Thermodynamic and Growth Kinetic Modeling of Solidification From a Metastable Mushy-Zone

submitted by

Justin E. Rodriguez

In partial fulfillment of the requirements for the degree of

Doctor of Philosophy

in

Mechanical Engineering

School of Engineering

Tufts University

Medford, Massachusetts

August 2016

Certified By:_____

Associate Professor Douglas Matson

Tufts University

Committee:_____

Associate Professor Luisa Chiesa

Tufts University

Committee:_____

Professor Mary Shultz

Tufts University

Committee:_____

Professor Robert Hyers

University of Massachusetts Amherst

Abstract

Improving the fidelity of modern casting simulation programs requires a detailed understanding of how solidification proceeds during the initial phase where rapid heat extraction along exterior surfaces strongly influences local structure and properties. The overarching goal of this research is to develop a better understanding of stable-phase rapid solidification from a metastable mushy-zone and how it relates to stable phase microstructures and material properties. With that goal in mind, this research consists of 3 primary parts: thermophysical property measurements, thermodynamic modeling, and growth kinetics analyses.

Electrostatic levitation (ESL) experiments were conducted at NASA Marshall Space-Flight Center (MSFC) to define stable and metastable phase thermodynamic properties for the Fe–Co alloy system. These properties were used to optimize the equilibrium phase diagram by investigating the extension of the metastable liquidus and solidus to allow prediction of the BCC-FCC-liquid peritectic, define the driving potential for solidification in undercooling experiments, and identify the partitioning coefficient for each phase.

Growth kinetics were measured using electromagnetic levitation (EML) techniques. The velocity of the stable phase growing through the mushy zone was found to be greater than that of the stable phase growing through undercooled liquid, and the velocity was found to be constant, regardless of the initial undercooling. This is explained, in part, by an effective change in the heat capacity of the growth environment. This effective heat capacity, C_P^{Eff}, considers remelting of the of the metastable phase in which case the pre-existing BCC δ–phase acts as a heat sink for the stable FCC γ–phase to release energy during

solidification. The second matter is the possibility that heat is conducted back from the tip of the growing dendrite such that conditions at the tip become non-adiabatic. These two considerations, used in conjunction with existing dendrite growth models, lead to a new "Non-adiabatic Remelt" growth model. The results show that for a given heat flux, there will be a minimum undercooling for which dendritic growth can be supported. The predicted growth velocity, which corresponds to that minimum undercooling, matches the measured experimental growth velocity data. This suggests that the growth of the stable phase into the mushy zone occurs under the minimum conditions required to support dendritic growth.

Acknowledgements

First and foremost I'd like to thank my mother. She worked tirelessly to provide me with as many opportunities as possible, and has supported me in every way imaginable. I can never repay those decades of selflessness, but I hope that this work makes her proud.

I'd also like to thank my extended family, aunts, uncles, cousins, and grandparents. They have all played a significant role in my life, and helped me develop into the person that I am today.

I want to thank my previous advisor and mentor, Ann Anderson. She played a pivotal role in my decision to pursue a Ph.D., and I appreciate her continued guidance.

I thank my committee for devoting their time and effort to reviewing my work, and providing invaluable feedback. I want to express my appreciation to my advisor, Doug Matson. Our relationship is one which I could have only dreamed of. I was given an enormous amount of freedom in terms of my research goals and the approach that I took, and that allowed me to develop skills beyond analytical methods and data analysis.

I'd like to express my gratitude to my lab group and my officemates, for our scientific and not-so-scientific banter. I want extend a special thank-you to my lab-mate, officemate, and good friend, Gabrielle String. Throughout my time at Tufts, we've spent countless hours studying together and discussing research. She has always been there for me, both academically and personally, and I'm glad that I had the opportunity to make such a great friend.

I'd would like to thank Glenn Fountain and Trudy L. Allen for technical

For my grandmother, Marilyn Ann Dyson.

Contents

List of Tables

List of Figures

Chapter 1

Introduction

Advanced materials are a cornerstone in nearly every field of technology. From consumer electronics to unmanned space vehicles, breakthroughs in materials science play a pivotal role in facilitating innovation. In 2011 the Materials Genome Initiative was implemented in the United States, with the main goal of reducing the amount of time that it takes to discover, develop, manufacture, and deploy new materials [1]. One critical mechanism for creating advanced materials is the ability to effectively utilize simulation-based engineering during the development process. Computational models have a proven track record of reducing the time and cost of development. The Committee on Integrated Computational Materials, of the National Academy of Sciences, provided a thorough investigation of the use computational materials engineering with multiple case studies [2]: While modeling aluminum castings, Ford Motor Co. benefited from a 15-25% reduction in development time and a significant reduction in cost. General Electric, Pratt & Whitney, and Boeing saw a 50% reduction in development time, and the amount of testing was reduced by up to a factor of eight.

There are two key components that are required for successful computational materials modeling: Accurate material properties, and a model that successfully describes the phenomena of interest. Containerless processing methods, such as electrostatic levitation (ESL), or electromagnetic levitation (EML), provide the means to accurately measure various material properties, and observe solidification phenomena under conditions that would otherwise be unachievable. In this case, the phenomenon of interest is known as double recalescence. Levitation processing allows a molten sample to undercool below the stable γ–phase (FCC) liquidus temperature over a wide composition range for Iron-Cobalt and Iron-Chromium-Nickel alloys. If the undercooling is sufficient, i.e. the temperature is below the melting point of the metastable δ–phase (BCC), the sample can solidify in a two-step process known as double recalescence. Recalescence refers to the rapid and intense brightening that occurs when the heat of fusion is released during solidification.

A typical thermal profile of a Fe–40 at.% Co sample that solidified via double recalescence is given in Figure 1.1. Figure 1.2 shows a progression of double recalescence solidification of a Fe–40 at.% Co sample.

The goal of this research is to develop a better understanding of rapid solidification phenomena and how it relates to microstructures and material properties. With that goal in mind, this research consists of 3 primary parts: thermophysical property measurements, thermodynamic modeling, and growth kinetics analyses. In the remainder of this paper, I will focus on thermodynamic modeling, and growth kinetics analyses, as those are my primary contributions to the body of knowledge.
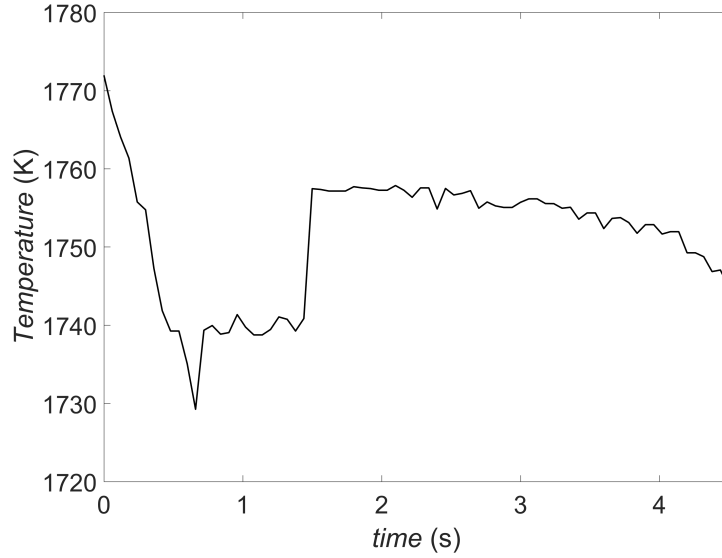
Figure 1.1: Thermal profile of a Fe–40 at.% Co sample processed ESL, which solidified via double recalescence.
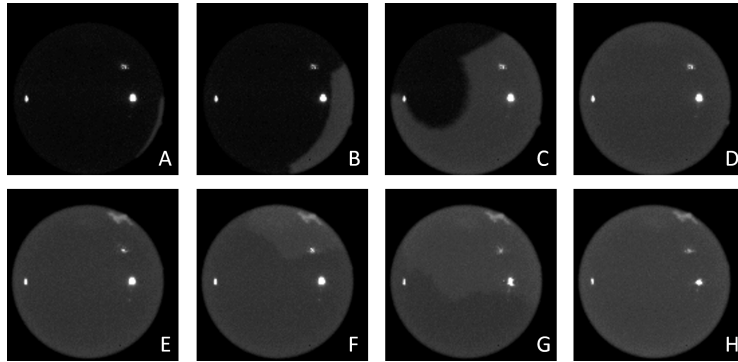
Figure 1.2: Images of the progression of solidification of a Fe–40 at.% Co sample processed ESL, which solidified via double recalescence. Images A-D show the growth of the metastable δ–phase growing through undercooled liquid. Images E-H show the stable γ–phase growing through the metastable mushy-zone.

Chapter 2

Literature Review

2.1 Rapid Solidification and Metastable Phase Formation

It is important to begin this discussion by explaining what a metastable phase is. A metastable phase is a phase that may exist for a period of time, but which does not correspond to the system's lowest energy state [3]. For materials, the equilibrium phase is described by the minimum Gibbs energy, which will be discussed in Section 2.2. Metastable phases represent a local minimum energy phase, but not the global minimum energy state. For example, natural diamonds are formed when carbon is subjected to high pressure and temperatures in the Earth's mantle. At the ambient temperatures and pressures at the Earth's surface, the diamond lattice is metastable, with graphite being the stable phase. Therefore, diamonds are, in fact, not "forever"; though for all intents and purposes, they are.

In terms of levitation experiments, the metastable phase is accessed by sup-

pressing heterogeneous nucleation, which alloys the molten sample to undercool below the stable liquidus temperature. As undercooling increases, the free energy difference between the undercooled liquid and the stable solid phase increases. This phenomenon is depicted graphically in Figure 2.1.
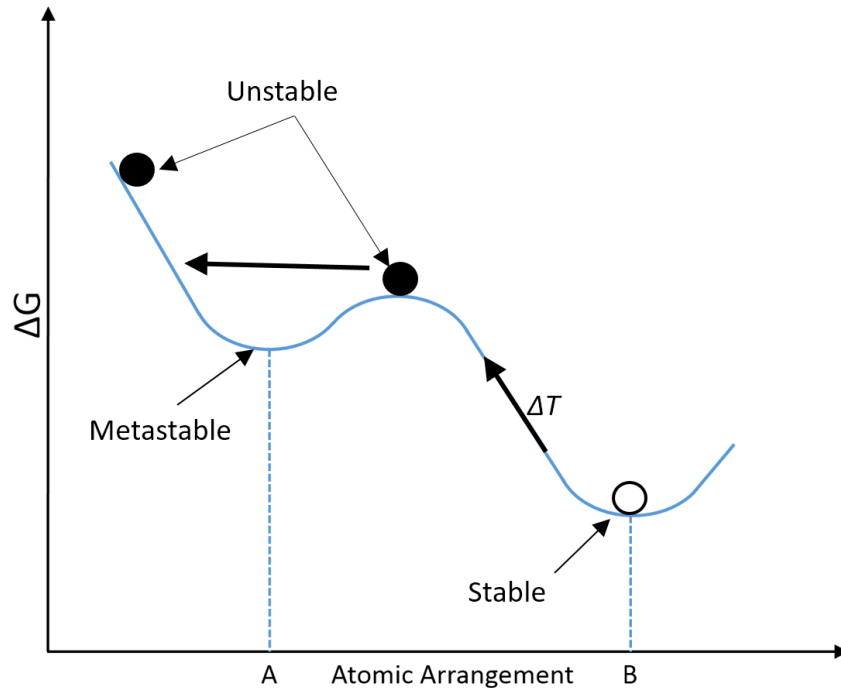
Figure 2.1: A schematic that describes the relationship between undercooling, ΔT, free energy, ΔG, and atomic arrangement.

Upon solidification, if the undercooling is sufficient, a metastable solid phase can form. Eventually, the metastable phase will transform into the stable phase. Figure 2.2 shows a schematic that describes the path of phase transformations upon solidification. The persistence of the metastable phase falls under the subject of kinetics, rather than thermodynamics, but it is related to the free energy hump between the metastable and stable phases.

Rapid solidification refers to a material's transition from a liquid to a solid, and is typically characterized by high growth rates, resulting in dendritic structures within solid solutions. In the event of double recalescence, the primary phase
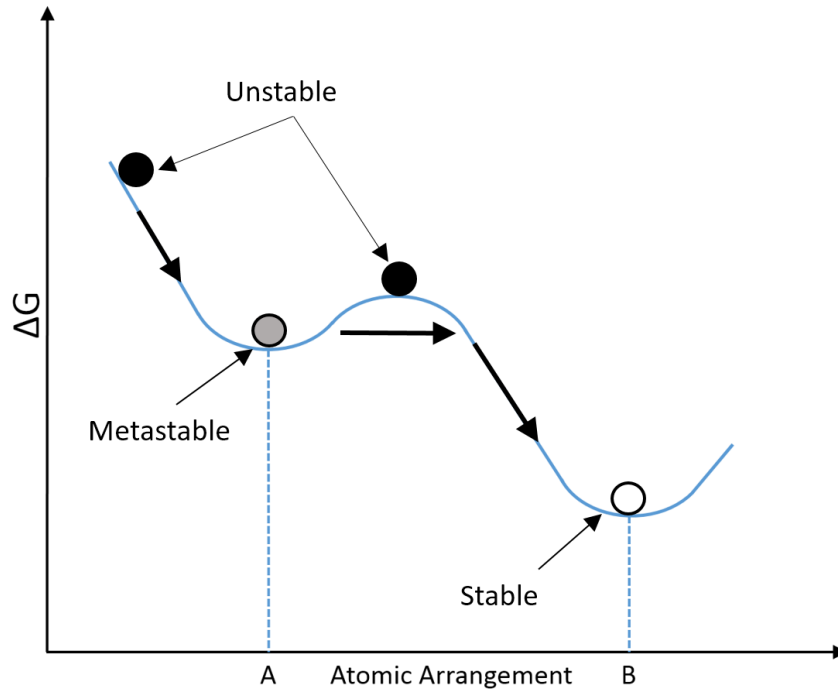
Figure 2.2: A schematic that describes the path of phase transformations upon solidification.

grows and releases heat of fusion which raises the temperature of the sample to a location between liquidus and solidus temperature of the metastable phase. The result is a combination of metastable solid and liquid, which is known as the mushy-zone. After a short delay time, nucleation and growth of the stable phase sets in and the temperature is further increased towards the equilibrium liquidus temperature by which the primary metastable phase is partially or wholly remelted and transformed into the stable phase [4–12]. Therefore, besides the delay time for nucleation, the growth velocity of the stable phase into the mushy-zone determines the dynamics of the metastable-stable phase transformation and is a decisive parameter controlling the formation of the microstructure.

Li *et al.* [13] discussed microstructure and phase selection in undercooled Fe–30 at.% Co melts in the context of glass flux experiments and subsequent

microscopical investigations on as-solidified samples but in-situ measurements during rapid solidification have not been carried out.

Koseki and Flemings performed a thorough investigation of solid phase formation and microstructure evolution [8–10, 14] on various $Fe_{70}CrNi$ alloys, using EML processing. They provided microstructural evidence showing that metastable δ–phase forms prior to the stable γ–phase, estimated the solidification velocities of the γ and δ phases growing into undercooled liquid from the measured recalescence time, and conducted a computer-aided microprobe analysis (CMA) to get concentration profiles of microstructures. The CMA results indicated that the metastable δ–phase primarily rejects nickel, while the stable γ–phase rejects chromium.

Matson *et al.* [11, 12] measured the solidification velocities of $FeCr_{15}Ni_{15}$ and $FeCr_{12}Ni_{16}$ wt.% alloys using a high-speed camera. The results of both solid phases, γ and δ, growing through undercooled liquid, as well as the γ–phase growing through the mushy-zone, were reported.

Based on the work of Löser *et al.* [15], and Moir and Herlach [16], Volkmann, *et al.* [17, 18], conducted a two-part study of nucleation and phase selection in undercooled Fe–Cr–Ni melts. In the first part of the study, they conducted a theoretical analysis of nucleation, regarding phase selection, in undercooled Fe–Cr–Ni melts. They concluded that the primary solid phase is determined by higher nucleation probability. If there is sufficient undercooling, the preferential nucleation of the metastable δ–phase can be explained by it having a lower solid liquid interface energy than the stable γ–phase. The purpose of the second part of study was to experimentally verify the conclusions from the initial theoretical investigation. Undercooling experiments were conducted on $Fe_{69}Cr_{31-x}Ni_x$ over a wide range of compositions. The results showed that for

low nickel concentration, where the δ–phase is stable, only δ–phase nucleated, regardless of undercooling; at higher nickel concentrations where the γ–phase is stable, if sufficient undercooling was achieved, the metastable δ–phase nucleated as the primary phase.

Within a NASA Science Requirements Document (SRD) regarding phase selection and containerless processing experiments, Flemings *et al.* [19] reported on microstructural observations in a sample that solidified via double recalescence as compared to one that solidified via single recalescence. The single recalescence sample showed long dendritic structures, while the double recalescence sample showed a fine equiaxed microstructure. This suggests that double recalescence can have a significant grain refinement effect.

2.1.1 Effects of Melt Convection

Growth kinetics and microstructural evolution are generally influenced by fluid flow because it affects the heat and mass transport at the solid-liquid interface. The effect is more apparent the lower the growth rate is compared to the fluid flow speed. [20]. The effects of melt convection are not completely understood, however experimental data suggests that under certain conditions, bulk fluid flow can affect solidification and the resulting microstructure of the material.

Glicksman *et al.* [21, 22] conducted isothermal dendrite growth experiments (IDGE) under terrestrial and microgravity conditions, and reported on the effects of natural convection on dendrite growth. The ground-based experiments were conducted using a U-shaped pyrex glass tube that had an expanded spherical chamber on one side to hold the bulk of the sample. Both sides of the tube were heated, and nucleation was initiated by turning off one heater

dropping a spherical steel ball into the liquid on one side of the tubing. The solid grew through the tubing and entered the spherical chamber through a capillary aperture. Microgravity experiments were conducted in a similar manner, except the test apparatus was made of steel and included viewing windows to make it more durable. The results indicated melt convection effects were significant up to undercoolings of 1.7 K. At low undercoolings, ~ 0.1 K, the growth velocity under microgravity conditions was greater than that under terrestrial conditions by approximately a factor of 3. The dendrite tip radius was correspondingly 50% smaller.

In a study on Ni–Al Reutzel *et al.* [23] compared the growth velocities of samples that were tested in an EML on ground, to those that were evaluated in microgravity. Ground-based EML results in a significant amount of convection because of the electromagnetic force that is required to overcome gravity, while EML in micro-gravity has no such limitation. They found that at low to moderate undercoolings, the growth velocity increased when subjected to melt convection.

Hermann *et al.* [5–7] reported Fe–Co growth velocity results for the γ–phase and metastable δ–phase growing through undercooled liquid, using EML processing in both terrestrial and microgravity conditions during parabolic flight; thus, different levels of forced electromagnetic stirring were achieved [24]. In those experiments double recalescence was detected by a fast responding silicon photo diode. Growth velocity of the primary growing phase was inferred from temperature-time characteristics while growth kinetics of the secondary stable phase could not be obtained by this method. However, an effect of melt convection on primary growth kinetics could not be detected because the solidification velocities of the γ and δ phases were in the range of several m/s

which is much larger than fluid flow velocities in EML processing on ground and under microgravity [24].

Matson *et al.* [25, 26] found that melt convection appears to influence the delay time between nucleation of the metastable phase and nucleation of the stable phase; the delay times of the samples that were tested in ESL are approximately an order of magnitude greater than the delay times of samples that were tested in EML. Hyers *et al.* [24] modeled flow conditions for gound-based ESL and EML and found that the fluid flow rate in ESL is ~4.4 cm/s, $Re \approx 110$ which is laminar [27], while the convection velocity in ground-based EML is ~32 cm/s, $Re \approx 2800$ which is turbulent [27]. Hanlon *et al.* [28] propose that the reduced delay time in EML samples is because convection in EML causes the dendrites to deflect, which results in impingement of the secondary arms of adjacent dendritic structures, thus creating preferred nucleation sites for the stable phase.

Matson [29] developed a model to evaluate the influence of both undercooling and convection on the incubation time for conversion of metastable to stable phase based on retained damage within the parent metastable matrix. This damage consists of two parts, non-equilibrium solidification effects and liquid shear induced defect development in the parent phase. The damage promotes stable phase nucleation by increasing the matrix volume free energy in a manner analogous to recrystallization and recovery during hot-working.

2.2   Thermodynamic Modeling

Thermodynamic modeling, in the context of material properties and phase change, dates back to an article written by Gibbs in 1879 [30]. In that article,

he reported on what became known as the Gibbs free energy relationships, given in Equations 2.1 and 2.2, which relate the free energy of a system to the enthalpy, and entropy.

$$G = H - TS \tag{2.1}$$

$$\frac{\partial G}{\partial T} = -S \tag{2.2}$$

By applying the first and second laws of thermodynamics, the constant pressure specific heat capacity can be related to the free energy, as shown in Equation (2.3) .

$$\frac{\partial^2 G}{\partial T^2} = -C_P/T \tag{2.3}$$

G is the Gibbs free energy, H refers to the enthalpy, S is the entropy, C_P is the constant pressure heat capacity, and T is the temperature.

By and large, "thermodynamic modeling" is synonymous with the "CALPHAD Method". Spencer [31] provides a brief history of CALPHAD. A detailed breakdown of the CALPHAD method can be found in a book written by Lukas, Fries, and Sundman [32].

The CALPHAD (CALculation of PHAse Diagrams) method is a process by which experimental and theoretical data on phase transitions and thermophysical properties is used to assess parameters mathematical models of the Gibbs energy [32]. The result is a set of equations that can be used to predict phase transition regions and thermophysical properties as a function of temperature, pressure, and composition.

2.2.1   The Fe–Co System

The Fe–Co phase diagram consists of BCC, FCC, HCP, and liquid phases and has a BCC-FCC-liquid peritectic point near 20 at.% cobalt, where the δ–liquid combination transforms to the γ–phase at the peritectic point. The initial modeling of the iron, cobalt, and iron-cobalt phase diagram was performed by Guillermet [33–35]. Updated pure element parameters for CALPHAD were later published in 1991 by Dinsdale [36] and again in 2001 [37], where the latter supersedes the former. More recently, Woodcock *et al.* [38] made an effort to develop a metastable phase diagram.

Figure 2.3 shown an image of the Fe–Co equilibrium phase diagram generated by Thermo-Calc, Version 8 (2015b), using the PBIN database.
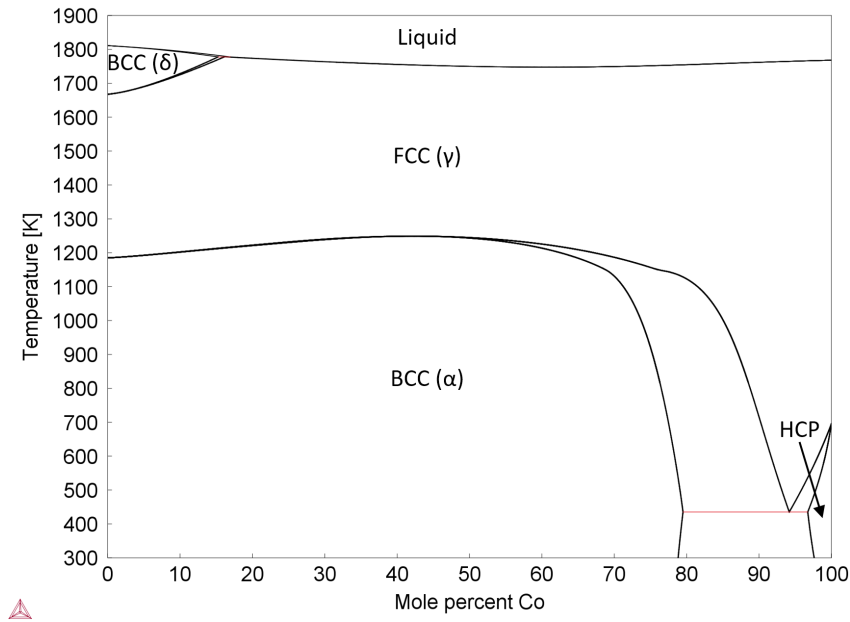
Figure 2.3: Fe–Co equilibrium phase diagram calculated with Thermo-Calc, Version 8 (2015b), with the PBIN database.

The thermodynamic model must consider each of these phase present for both iron and cobalt, as well as the excess free energy and the magnetic contribution. The molar free energy of the Fe–Co system is given as [35]:

$$G_m^\alpha = x_1 G_1^{o,\alpha} + x_2 G_2^{o,\alpha} + RT(x_1 ln(x_1) + x_2 ln(x_2)) + G_m^{E,\alpha} + \Delta G_m^{mg}. \tag{2.4}$$

The subscripts 1 and 2 correspond to the solvent (iron) and solute (cobalt). $G^{o,\alpha}$ represents the molar Gibbs energy of the element, or phase α, where the magnetic contribution is neglected. $G_m^{E,\alpha}$ is the excess free energy of the given phase, and ΔG_m^{mg} is the magnetic contribution.

The free energy for each phase of each component is a function of the enthalpy, entropy, the magnetic contribution, as well as the pressure contribution. The form of the equation used to calculate the free energy of each component, in a nonmagnetic state, where the temperature is less than the melting temperature, is given by [33–35]:

$$G_e^{o,\alpha} = a_e^\alpha + b_e^\alpha T + c_e^\alpha T ln(T) + d_e^\alpha T^2 + e_e^\alpha T^3 + f_e^\alpha T^{-1} + j_e^\alpha T^{i+1} + \int_0^P V_m(T,P) dP \tag{2.5}$$

The subscript e indicates which element is being analyzed, and it corresponds to the subscripts 1 and 2 from Equation (2.4). Parameters c_e^α, d_e^α, e_e^α, f_e^α, and j_e^α are directly related to the heat capacity of the material. In addition to the previously mentioned parameters, the enthalpy is directly influenced by a_e^α and b_e^α, and the entropy is a dependent on b_e^α. The integral term accounts for the pressure contribution to the free energy. Similarly, the equation for the individual components when the temperature is greater than the melting temperature, is of the form [33–35]:

$$G_e^{o,\alpha} = a_e^{\alpha,H} + b_e^{\alpha,H} T + c_e^{\alpha,H} T ln(T) + j_e^{\alpha,H} T^{i+1} + \int_0^P V_m(T,P) dP \tag{2.6}$$

The superscript H indicates that the parameters are associated with the high temperature form of the equation, where the temperature is greater than the melting temperature, T_m. The superscript i is equal to -10 for the solid phases and 6 for the liquid phase [33, 34]. From the fundamental free energy relationships, Equations (2.1)-(2.3), along with Equations (2.5)-(2.6), it becomes evident that coefficients a_e-j_e are related to the enthalpy, b_e-j_e are related to the entropy, and c_e-j_e are related to the heat capacity. The pressure term is given in Equation (2.7).

$$\int_0^P V_m(T,P)dP = \frac{V_o exp(a_0 T + \frac{1}{2}a_1 T^2 + a_2/T)}{(K_0 + K_1 T + K_2 T^2)(n-1)}[(1-nP(K_0+K_1 T+K_2 T^2))^{1-1/n}-1]$$

$$(2.7)$$

For continuity at $T > T_m$ the heat capacities of the solid phases are made to approach that of the liquid phase [33, 34]. Similarly, for $T > T_m$ the heat capacity of the liquid phase is made to approach the heat capacity of the solid phase at room temperature (C_P^{BCC} for iron, and C_P^{HCP} for cobalt) [33, 34]. The j_e terms, in Equations (2.5) and (2.6), account for the asymptotic approaches of the heat capacities under the previously mentioned conditions. Therefore, for $T > T_m$ the $j_e^{\alpha,H}$ term is assumed to be zero for the liquid phase, and for $T < Tm$ the j_e^α term is assumed to be zero for the solid phases [33, 34]. The excess free energy for the Fe–Co system is given by the following sub-regular solution model [35]:

$$G_m^{E,\alpha} = x_{Co}x_{Fe}[L_{Co,Fe}^{0,\alpha} + L_{Co,Fe}^{1,\alpha}(x_{Co} - x_{Fe})]. \qquad (2.8)$$

The equation for $L_{Co,Fe}^{0,\alpha}$ takes the following form:

$$L_{Co,Fe}^{0,\alpha} = a^{0,\alpha} + b^{0,\alpha}T + c^{0,\alpha}Tln(T), \tag{2.9}$$

where $b^{0,\alpha}$ and $c^{0,\alpha}$ are zero for all of the phases except for the BCC phase. Similarly, the equation for $L_{Co,Fe}^{1,\alpha}$ is given below in Equation 2.10.

$$L_{Co,Fe}^{1,\alpha} = a^{1,\alpha} + b^{1,\alpha}T \tag{2.10}$$

where $b^{0,\alpha}$ is a zero for all of the phases except for the FCC phase.

The magnetic contribution, ΔG_m^{mg}, is given by:

$$\Delta G_m^{mg} = RTln(\beta + 1)f(\tau), \tag{2.11}$$

where τ is defined as T/T_c, and β is the magnetic entropy parameter. T_c is the critical temperature associated with magnetic ordering, and is given by the Curie temperature (T_C) and Néel temperature (T_N) for ferromagnetic and antiferromagnetic ordering, respectively.

$$\beta^\alpha = x_{Fe}\beta_{Fe}^\alpha + x_{Co}\beta_{Co}^\alpha + x_{Co}x_{Fe}[\beta_{Co,Fe}^{0,\alpha} + \beta_{Co,Fe}^{1,\alpha}(x_{Co} - x_{Fe})] \tag{2.12}$$

For $\tau < 1$:

$$f(\tau) = 1 - \frac{1}{A}\left[\frac{79\tau^{-1}}{140p} + \frac{474}{497}\left(\frac{1}{p} - 1\right)\left(\frac{\tau^3}{6} + \frac{\tau^9}{135} + \frac{\tau^{15}}{600}\right)\right] \tag{2.13}$$

For $\tau > 1$:

$$f(\tau) = -\frac{1}{A}\left(\frac{\tau^{-5}}{10} + \frac{\tau^{-15}}{315} + \frac{\tau^{-25}}{1500}\right) \tag{2.14}$$

$$A = \frac{518}{1125} + \frac{11692}{15975}\left[\frac{1}{p} - 1\right] \tag{2.15}$$

p is a parameter that is based on the structure of the material, and was taken to be 0.28 for the FCC and HCP phases, and 0.4 for the BCC phase. The critical temperature, T_c, as a function of composition is given in Equation (2.16).

(2.11)-(2.16)

$$T_c^\alpha = x_{Fe}T_{c_{Fe}}^\alpha + x_{Co}T_{c_{Co}}^\alpha + x_{Fe}x_{Co}\left[T_{c_{Co,Fe}}^{0,\alpha} + T_{c_{Co,Fe}}^{1,\alpha}\left(x_{Co} - x_{Fe}\right)\right] \tag{2.16}$$

The superscript α refers to the phase of interest.

Phase Transformations

The low temperature region of the Fe–Co phase diagram, which will be defined as $T < 1400$ K for the purposes of this discussion, contains $\alpha \rightleftharpoons \gamma$ and $HCP \rightleftharpoons \gamma$ phase transformations. Ellis [39] reported on the $\alpha \rightleftharpoons \gamma$ transitions in the 0-90 at.% Co range. For cobalt compositions less than 70 at.%, the temperature of the sample was measured while a constant heat flow was applied. The temperatures that corresponded to phase transition regions were then identified by the altered rate of heating and cooling. At compositions greater than 70 at.% Co the samples were heated to a specific temperature and quenched to preserve the lattice structure, and then an X-ray diffraction analysis was conducted to determine which phases were present. Similarly Masumoto [40, 41] performed thermal analysis experiments on Fe–Co alloys ranging from 0-99.32 at.% Co, and discussed $\alpha \rightleftharpoons \gamma$ and $HCP \rightleftharpoons \gamma$ transformations. Fischer *et al.* [42] tested Fe–Co alloys in the 0-18 at.% Co range using a magnetic susceptibility method,

and reported on $\alpha \rightleftharpoons \gamma$ transformations. Normanton *et al.* [43] conducted calorimetry experiments on alloys ranging from 0-100 at.% Co, and discussed the $\alpha \rightleftharpoons \gamma$ transformations in the range of 0-70 at.% Co.

The high temperature region, $T < 1400$ K, contains $\gamma \rightleftharpoons \delta$, $\delta \rightleftharpoons Liquid$, and $\gamma \rightleftharpoons Liquid$ transformations. Harris and Hume-Rothery [44] conducted thermal analysis experiments on Fe–Co alloys in the range of 0-31 at.% Co, and provided information on the $\gamma \rightleftharpoons \delta$, $\delta \rightleftharpoons Liquid$, and $\gamma \rightleftharpoons Liquid$ transitions. Predel and Mohs [45] performed calorimetry experiments on alloys ranging from 0-100 at.% Co, and discussed on the $\delta \rightleftharpoons Liquid$, and $\gamma \rightleftharpoons Liquid$ transformations. Fischer *et al.* [42] tested Fe–Co alloys in the 0-18 at.% Co range using a magnetic susceptibility method, and reported on $\gamma \rightleftharpoons \delta$ transformations.

Thermophysical Properties

An article by Guillermet [35] provides an extensive list of experimental thermophysical property data that is available for the Fe–Co system. Müller and Hayes [46], Castanet [47], and Normanton *et al.* [43] have reported on the heat capacity of various Fe–Co Alloys. Müller and Hayes [46], and Castanet [47] tested equiatomic compositions, while Normanton *et al.* [43] provided data on compositions ranging from 0 to 100 at.% Co.

The enthalpy of formation of Fe–Co solid solutions has been reported by Satow *et al.* [48] at 1093 K, Steiner and Krisement [49] 1143 K, Müller and Hayes [46] at 1143 K and 1473 K, and Hajra [50] at 1173 K. The enthalpy of formation of Fe–Co liquid solutions has been discussed by Predel and Mohs [45] at 1873 K, Batalin *et al.* [51] at 1873 K, and Tozaki *et al.* [52] at 1823 K < T < 1863 K. Satow *et al.* [48] also reported on the excess entropy at 1093 K.

Activity measurements for iron and cobalt have been reported by Rammensee

and Fraser [53] at 1473 K and 1873 K, Vrestal *et al.* [54] at 1500 K, Tomiska and Neckel [55, 56] at 1650 K and 1873 K, and Belton and Fruehan [57] as well as Maruyama [58] at 1873 K. Satow *et al.* [48] also presented activity data at 1013 K, 1153 K, and 1293 K, though just for iron. Both Tomiska [56] and Belton and Fruehan [57] reported activities with high positive deviations from ideal solutions, however the rest of the available data shows negative deviations for both iron and cobalt.

2.3 Dendrite Growth Theory

A dendrite is a branched tree-like structure that develops during alloy solidification and is a direct result of thermal and solutal perturbations at the solid-liquid interface, which leads to preferential solidification. Dendritic growth is the most common form of solidification that occurs in alloys, and it is typically characterized by primary growth direction, tip radius, primary spacing, and higher-order arm spacing. In a review article, Trivedi and Kurz provide a detailed overview of dendrite growth theory [59]. The article is somewhat dated at this point, however the fundamentals remain largely unchanged.

Dendritic structures typically result from one of two growth conditions: 1) Growth from an undercooled melt, which results in an equiaxed grain structure. 2) Directional solidification, which results in dendrites that grow parallel to one another and to the direction of heat rejection. It should be noted that the underlying mechanisms of solidification are the same for both growth conditions; the solid is growing into an undercooled melt. However, in the case of directional solidification, the direction of thermal gradient is carefully controlled, and that has a significant impact on the macrostructure of the material and macroscopic

strength properties. Versnyder and Shank [60] provide a detailed description of directional solidification and the effects on macrostructures of metal.

The first consideration when solving a steady-state dendrite growth problem consists of solving the steady-state thermal and solute diffusion equations, given in Equations (2.17) and (2.18).

$$\nabla^2 T + \frac{V}{\alpha_L} \frac{\partial T}{\partial z} = 0 \tag{2.17}$$

$$\nabla^2 C + \frac{V}{D_o} \frac{\partial C}{\partial z} = 0 \tag{2.18}$$

T is the temperature, C is the concentration, V is the growth velocity, α_L is the thermal diffusivity, D_o is the solute diffusivity, and z is the growth direction. The second considerations that the interface energy is required to define the dendrite growth problem. The interface energy acts to stabilize the dendrite, and prevent tip splitting.

The solution is particularly complex due to the fact that the geometry of the dendrite is initially unknown, and must be resolved in a self-consistent manner. That is, the solutions to the thermal and solutal diffusion equations must be shape preserving [59].

2.3.1 The Ivantsov Solution

Papapetrou [61] was the first to suggest that an isothermal parabolic interface would satisfy the shape preserving condition. In 1947, Ivantsov [62] developed the first self-consistent solution to the diffusion equations for a parabolic dendrite. The solution proceeds as follows.

$$T_t - T_\infty = \frac{\Delta H_f}{C_P^L} Iv(P_T) \tag{2.19}$$

$$C_t - C_o = C_T(1 - k_e)Iv(P_C) \tag{2.20}$$

T_t is the temperature of the tip of the dendrite, T_∞ is the liquid bath temperature, ΔH_f is the heat of fusion, C_P^L is the constant pressure specific heat capacity, C_t is the solute concentration at the tip, C_o is the solute concentration of the bulk liquid, k_e is the partitioning coefficient. $Iv(P_T)$ and $Iv(P_C)$ are Ivantsov functions, where the function arguments are the the thermal and solutal Péclet numbers, respectively. Alternatively, Equation (2.20) can be written as:

$$\frac{C_t}{C_o} = \frac{1}{1 - (1 - k_e)Iv(P_C)}. \tag{2.21}$$

The definitions of the Péclet numbers are given in Equations (2.22) and (2.23).

$$P_T = \frac{VR}{2\alpha_L} \tag{2.22}$$

$$P_C = \frac{VR}{2D_o} \tag{2.23}$$

V is the dendrite tip velocity, and R is the dendrite tip radius. The definition of the Ivantsov function is given in Equation (2.24).

$$Iv(P_x) = P_x e^{P_x} E_1(P_x) \tag{2.24}$$

$E_1(P_x)$ is the exponential integral function, where the argument P_x refers to the thermal or solutal Péclet number. Assuming linear phase lines, and neglecting capillary and interface kinetic effects, the total undercooling is given by:

$$\Delta T = (T_T - T_\infty) - m_L(C_t - C_o), \tag{2.25}$$

where m_L is the slope of the liquidus line. Combining Equations (2.19) and (2.21) with Equation (2.25) yields the total undercooling Ivantsov solution:

$$\Delta T = \frac{\Delta H_f}{C_P^L} Iv(P_T) - m_L C_o \left[\frac{(1-k_e)Iv(P_C)}{1-(1-k_e)Iv(P_C)} \right] \tag{2.26}$$

From Equation 2.26, it should be clear that the solution only provides unique values of Péclet, or the product VR. Therefore, there are a multitude of growth velocity or tip radius values, where the tip velocity is inversely proportional to the growth velocity, that satisfy the solution.

If capillary effects are considered, the "modified Ivantsov solution", given in Equation (2.27), is obtained [63–65]:

$$\Delta T = \frac{\Delta H_f}{C_P^L} Iv(P_T) - m_L C_o \left[\frac{(1-k_e)Iv(P_C)}{1-(1-k_e)Iv(P_C)} \right] + \frac{2\Gamma}{R}. \tag{2.27}$$

Γ is the Gibbs-Thomson coefficient, given by:

$$\Gamma = \frac{\sigma}{\Delta S_f}, \tag{2.28}$$

where ΔS_f is the entropy of fusion, and σ is the solid-liquid interfacial energy. The total bath undercooling is often represented as the sum of the individual undercooling components, as shown below.

$$\Delta T = \Delta T_T + \Delta T_C + \Delta T_R \tag{2.29}$$

ΔT_T is the thermal undercooling, ΔT_C is the solutal undercooling, and ΔT_R is the capillary or curvature undercooling. With this presentation, the factors that contribute to the total bath undercooling become more apparent. The thermal undercooling accounts for the difference in temperature between the dendrite tip and the bulk liquid, the solutal undercooling represents the undercooling that results from solute buildup at the tip, and the capillary undercooling accounts for the local suppression of the liquidus temperature as a result of the curved interface. The undercooling components are given in Equations (2.30)-(2.32).

$$\Delta T_T = \frac{\Delta H_f}{C_P^L} Iv(P_T) \tag{2.30}$$

$$\Delta T_C = m_L C_o \left[1 - \frac{1}{1 - (1 - k_e)Iv(P_C)} \right] \tag{2.31}$$

$$\Delta T_R = \frac{2\Gamma}{R} \tag{2.32}$$

Figure 2.4 shows an example of the undercooling components on an equilibrium phase diagram.

There are several key points to take away from the undercooling solution thus far: 1) The solution predicts unique values of the Péclet numbers, however, unique values of V and R remain unknown. 2) The solution does not account for significant non-equilibrium effects such as solute trapping. 3) The inclusion of capillary effects renders the solution inherently approximate in nature. The
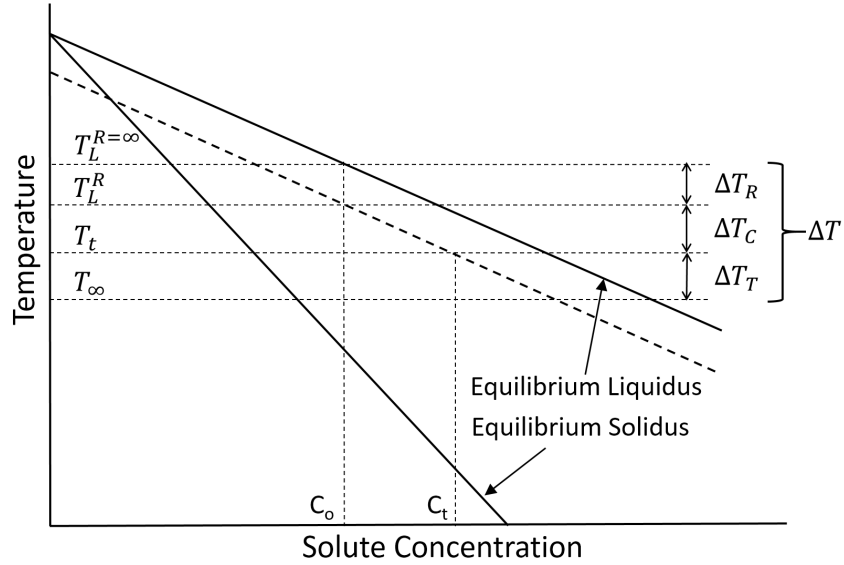
Figure 2.4: Phase diagram including the definitions of the undercooling components. The dashed line represents the suppression of the liquidus line as a result of the curved solid-liquid interface.

Ivantsov solution is rigorous under steady-state isothermal growth conditions, however, the capillary effect will vary along the curved surface of the dendrite tip, and that will make the interface non-isothermal.

In order to further constrain the problem, the Ivantsov solution needs to be combined with a stabilizing effect such as the interfacial energy.

2.3.2 Dendrite Tip Radius Selection Condition and its Application Within Dendrite Growth Theory

As previously stated at the end of Section 2.3.1, the modified Ivantsov solution only produces singular results for the Péclet numbers, or the product VR. However, the inclusion of the capillary term creates an extremum in the velocity-radius relationship; it was initially believed that solidification occurs at that maximum velocity point. Glicksman *et al.* [21] performed growth velocity experiments on succinonitrile, and found that although the then-current theory

23

predicted the Péclet numbers reasonably well, the measured growth velocity was significantly lower than the theoretical velocity; thus proving that solidification does not occur under maximum-velocity conditions, and suggesting that an absolute stability condition should exist.

The dendrite tip radius selection criterion can be considered to be a balance between the thermal and solute gradient destabilizing effects in the undercooled liquid, and the stabilizing influence of the interfacial energy [59].

Mullins and Sekerka [66] assessed the stability of a planar interface by employing a perturbation analysis, and the results provided the first rigorous solution for the stability of a planar interface. Within their analysis they assumed that the thermal diffusion length was much greater than the wavelength of perturbations, which is not valid under rapid solidification conditions.

In 1977, Langer and Müller-Krumbhaar [67] proposed that the dendrite tip radius R is approximately equal to the Mullins-Sekerka [66] minimimum wavelength for planar instabilities, λ_s. Then they applied that within a marginal stability criterion for the dendrite tip radius [68]. The marginal stability criterion states that the radius of the dendrite tip would be as large as possible while remaining stable, hence, "marginal stability criterion". Their analysis was limited to small thermal and solutal Péclet numbers and, under that assumption, they found that the product VR^2 is constant.

Using the marginal stability criterion, Lipton, Glicksman, and Kurz (LGK) [69], and Karma and Langer [70] developed dendrite growth theories that provided unique values for V and R. Both theories predict experimental results reasonably well, however, they are only valid at to low undercoolings, due to the limitations of the marginal stability criterion.

In 1986, Trivedi and Kurz [71] extended the marginal stability criterion to

include large Péclet numbers, and therefore large undercoolings. This has become a cornerstone for our understanding of dendrite stability. Soon after, Lipton, Kurz, and Trivedi (LKT) [72] extended LGK theory [69] to include large Péclet numbers using the new marginal stability criterion. LKT theory consists of the thermal, solutal, and capillary undercooling components from the modified Ivantsov solution, with the inclusion of the extended marginal stability criterion as the second equation such that unique values of V and R can be determined. The general expression for dendrite tip selection is given in Equation (2.33).

$$-\frac{\Gamma}{\sigma^* R^2} - \left[\bar{K}_S G_S \xi_S + \bar{K}_L G_L \xi_L\right] + m_L G_C \xi_C = 0 \qquad (2.33)$$

Γ is the Gibbs-Thomson coefficient, σ^* is the stability parameter, G_C is the solute gradient in the liquid, G_S and G_L are the temperature gradients in the solid and liquid, respectively. ξ_C, is the solute stability function, dependent on the solutal Péclet number, while ξ_S and ξ_L are the stability functions, dependent on the thermal Péclet numbers for the solid and liquid, respectively. $\bar{K}_S$ and $\bar{K}_L$ are the weighted conductivities of the solid and liquid, given as $\bar{K}_S = K_S/(K_S + K_L)$ and $\bar{K}_L = K_L/(K_S + K_L)$. The stability functions are shown in Equations (2.34)-(2.36).

$$\xi_L = \frac{(1 + \bar{\kappa})\left(-1 + \sqrt{1 + \frac{1}{\sigma^* P_t^2}}\right)}{\bar{\kappa}\left(1 + \sqrt{1 + \frac{1}{\sigma^* P_t^2}}\right) + \left(-\bar{\alpha} + \sqrt{\bar{\alpha}^2 + \frac{1}{\sigma^* P_t^2}}\right)} \qquad (2.34)$$

$$\xi_S = \frac{(1 + \bar{\kappa})\left(\bar{\alpha} + \sqrt{\bar{\alpha}^2 + \frac{1}{\sigma^* P_t^2}}\right)}{\bar{\kappa}\left(1 + \sqrt{1 + \frac{1}{\sigma^* P_t^2}}\right) + \left(-\bar{\alpha} + \sqrt{\bar{\alpha}^2 + \frac{1}{\sigma^* P_t^2}}\right)} \qquad (2.35)$$

$$\xi_C = 1 + \frac{2k_e}{1 - 2k_e - \sqrt{1 + \frac{1}{\sigma^* P_c^2}}} \tag{2.36}$$

$\bar{\kappa}$ is the ratio of the thermal conductivity of the liquid to that of the solid, $\bar{\alpha}$ is the ratio of the thermal diffusivity of the liquid to that of the solid. For an isothermal dendrite $G_S = 0$. G_L and G_C are given in Equations (2.37)-(2.38).

$$G_L = -\frac{2P_t \Delta H_f}{C_P^L R} \tag{2.37}$$

$$G_C = \frac{-2C_o P_c (1 - k_e)}{R(1 - (1 - k_e)Iv(P_c))} \tag{2.38}$$

Within the marginal stability criterion, Langer and Müller-Krumbhaar [68] set σ^* to be equal to $1/4\pi^2$. There no justification for that other than the fact that it gives good agreement with experimental results. Several authors have solved the self-consistent dendrite growth problem, which includes capillary effects at the boundary conditions [73–78]. The solution that allows for a stable dendrite tip, without tip splitting, is known as the microsolvability condition. The solutions show that no steady-state dendrite shape exists under isotropic capillary conditions. Solvability theory considers solid-liquid interface energy anisotropy, where the value of the stability parameter takes the form $\sigma^* = \sigma_o \varepsilon_C^{7/4}$. σ_o is a constant, and ε_C corresponds to the interface energy anisotropy [73, 74]. When external flow is considered, the stability parameter becomes a function of the flow velocity, U, where $\sigma^* = \sigma_o \varepsilon_C^{7/4} f(U)$ [79–81].

More recently, Alexandrov *et al.* [82–85] developed a stability criterion, via the mocrosolvability approach, for a non-isothermal dendrite growing under

forced convection within the thermo-solutal and kinetic growth regimes. The general form of the solution is the same as that given by the marginal stability criterion. Although the solution is analytically rigorous, it gives rise to a number of parameters that are adjustable, or must be determined using phase-field modeling.

2.3.3 Non-Equilibrium Effects During Dendritic Growth

Thus far, the discussion on dendrite growth has not included major non-equilibrium effects. There are two non-equilibrium effects that will be discussed in this section: 1) Solute trapping. 2) Undercooling due to attachment kinetics.

During rapid solidification, the solid-liquid interface is not necessarily heat-flow or diffusion limited. In that case, solute can be trapped by the growing solid phase before it has a chance to diffuse to reach equilibrium concentrations [86]. There have been a number of articles that discuss or demonstrate this phenomenon [10, 87, 88]

Solute trapping can be characterized by velocity dependent deviations from the equilibrium partition coefficient, k_e, and the equilibrium liquidus slope, m_L. As solidification velocity increases, the partition coefficient deviates from equilibrium and approaches unity, where there is complete solute trapping. Aziz and Kaplan [86] utilized chemical rate theory, which provides an expression for the rate of diffusion of impurities across an interface, to find a velocity dependent partition coefficient, k_v, shown in Equation (2.39).

$$k_v = \frac{k_e + V/V_d}{1 - (1 - k_e)X_o + V/V_d} \tag{2.39}$$

X_o is the initial solute atomic fraction, and V_d is the atomic diffusive speed at the solid-liquid interface, shown in Equation (2.40).

$$V_d = D_o/a_o \qquad (2.40)$$

D_o is the solute diffusivity, and a_o is the atomic spacing in the liquid. The velocity dependent liquidus slope, from Boettinger, Coriell, and Trivedi, (BCT) [89] is given in Equation (2.41).

$$m_v = m_L \left[\frac{1 + \left[k_e - k_v(1 - ln(k_v/k_e)) \right]}{1 - k_e} \right] \qquad (2.41)$$

Utilizing the non-equilibrium partition coefficient and liquid slope, BCT theory [89] gives the following equation for the solutal undercooling:

$$\Delta T_C = m_L C_o \left[1 - \frac{m_v/m_L}{1 - (1 - k_v)Iv(P_C)} \right] \qquad (2.42)$$

The non-equilibrium partition coefficient is also applied within the the solutal stability function, ξ_C, and the solute gradient in the liquid, G_C, given Equations (2.36) and (2.38), in place of the equilibrium partition coefficient k_e.

The second aspect of non-equilibrium growth that needs to be considered is the interface kinetics. At high undercoolings, solidification is not diffusion limited, but it is limited by the impingement rate of atoms at the interface [90]. This is often referred to as thermally driven, or kinetically limited growth. BCT theory gives the following equation for the kinetic undercooling:

$$\Delta T_K = V/\mu. \qquad (2.43)$$

μ is the kinetic growth coefficient, shown in Equation (2.44).

$$\mu = \frac{\Delta H_f V_o}{\bar{R} T_m^2} \tag{2.44}$$

T_m is the melting temperature, $\bar{R}$ is the universal gas constant, and V_o is the kinetic rate parameter, where $V_d < V_o < V_S$. V_S is the speed of sound through the liquid, and V_d is the diffusive speed defined above. With the inclusion of the kinetic undercooling, the total undercooling becomes:

$$\Delta T = \Delta T_T + \Delta T_C + \Delta T_R + \Delta T_K \tag{2.45}$$

2.3.4   Dendrite Growth During Chill Casting

In an effort to capture the quenching effects observed in chill casting, Koseki [8] developed a dendrite growth model which includes heat extraction through the growing solid dendrite. The model, which is based off of LKT and BCT theory, assumes that there is some heat sink at the base of the dendrite, which causes heat to conduct from the tip of the base of the structure.

The conduction is evaluated mathematically as a velocity dependent reduction of the heat of fusion. With that consideration, the thermal undercooling (see Equation (2.30)) and thermal gradient in the liquid (see Equation (2.37)) become:

$$\Delta T_T = \frac{1}{C_P^L}(\Delta H_f - J_S/V)Iv(P_T), \tag{2.46}$$

$$G_L = -\frac{2P_t}{C_P^L R}(\Delta H_f - J_S/V). \tag{2.47}$$
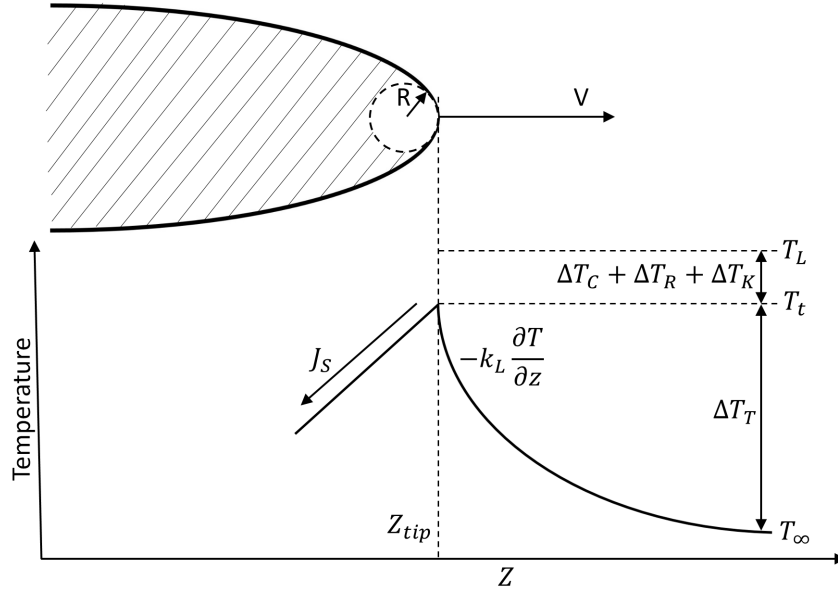
Figure 2.5: Schematic of the thermal field around a growing dendrite tip during chill casting [8].

J_S is the heat flux conducted from the dendrite tip back down its length, V is the solidification velocity. In this case, the thermal gradient in the solid is non-zero, and is given in Equation (2.48).

$$G_S = \frac{J_S}{k_S} \tag{2.48}$$

The remainder of the marginal stability criterion, given in Equations (2.33)-(2.38), remains unchanged. The stability criterion can be arranged into a quadratic equation which can be solved for the growth velocity, V, as shown in Equations (2.49)-(2.52).

$$AV^2 - BV + C = 0 \tag{2.49}$$

$$A = \frac{\Gamma}{4\sigma^* \alpha_L^2 P_t^2} \tag{2.50}$$

$$B = \frac{\bar{\kappa}\Delta H_f}{k_L(1+\bar{\kappa})}\zeta_L + \frac{m_L C_o(k_v - 1)}{D_o(1 - (1 - k_v)Iv(P_c))}\zeta_C \qquad (2.51)$$

$$C = \frac{\bar{\kappa}J_S}{k_L(1+\bar{\kappa})}(\zeta_L + \zeta_S) \qquad (2.52)$$

Chapter 3

Experimental Methods

For the electrostatic levitation experiments, Fe–Co and Fe–Cr–Ni samples , from 99.995% pure iron, chromium, and nickel, and from 99.95% pure cobalt. The Fe–Co samples were prepared at 30, 40, and 50 at.% cobalt, and the Fe–Cr–Ni samples were prepared at 16 wt.% chromium and 12 wt.% nickel. The components were arc-melted under an argon atmosphere, such that the samples had a mass of approximately 40-60 mg (~2 mm diameter). They were processed via ESL, where the negatively charged sample was contained within a vacuum chamber (evacuated to 10^{-9} mbar), between a negatively charged lower plate, and a positively charged upper plate.

The sample was then melted, allowed to cool radiatively, and then solidify. An article by Rogers and SanSoucie [91] gives a full description of the experimental setup. The location of the sample was determined by positioning lasers, and the electrostatic field was adjusted accordingly. The temperature of the samples was monitored with a Mikron Mi-GA140 single color pyrometer, which has a 1.45 μm to 1.8 μm wavelength range, and was operating at 16 Hz. The pyrometer accuracy, as stated by the manufacturer, is ± 0.3% of reading in °F

+ 1.8 °F for T < 2732 °F (1773 K), and ± 0.5% of reading in °F for T > 2732 °F (1773 K). The pyrometer was calibrated with a Mikron M390 blackbody generator [92]. The complete pyrometer specifications can be found in Appendix A.

The solidification was monitored with a high-speed camera, which was operating at 14,800-50,000 frames per second at 128x128-512x512 image resolution. The variations in frame rate and image resolution depended on which camera was being used, and which alloys were being evaluated. There were three cameras that were used during testing: Phantom V7.1, IDT MotionPro Y4, and IDT MotionPro Y7. The phantom V7.1 and the IDT MotionPro Y7 were the primary cameras that were used since they are capable of achieving higher frame rates. Both the IDT MotionPro Y4 and Y7 have significantly more memory than the Phantom V7.1, and they are capable of partitioning memory segments, which is useful when taking data in rapid succession, so they were used when long videos (>3 s) were taken or when videos were taken in rapid succession. The complete camera specifications can be found in Appendix A.

Several samples were also quenched in Indalloy 46L. The purpose of quenching samples is to preserve the microstructure at various points during the solidification process, such that the evolution of the solidification interactions can be evaluated. An article by SanSoucie *et al.* [93] details the quenching procedure.

EML growth velocity and delay time experiments were carried out in a collaboration with Thomas Volkmann and Carolina Kreischer at the German Aerospace Center (DLR)[1]. Fe–Co alloys were arc melted from 99.995 at.% pure Fe and Co under high purity (6N) 1 bar Ar atmosphere. The sample

mass is about 1g corresponding to a sphere of typically 6.5 mm in diameter. The vacuum chamber of the levitation facility is evacuated to 10^{-6} mbar and then filled with high purity (6N) He to 400 mbar. The sample is levitated and inductively heated in a coil consisting of water-cooled Cu-windings carrying an alternating current of frequency in the range of 350 kHz. Samples were melted and then cooled by a He gas stream in several cycles. The temperature-time profile was measured by an IMPAC ISR 12-CO single color pyrometer at 100 Hz with an operating range of 0.8 - 1.05 um. Rapid solidification during recalescence of the undercooled melt was recorded with a Photron Fastcam SA5 high-speed video camera at a rate of 75,000 fps and a resolution of 320 x 264 pixels. A comprehensive description of the levitation facility is given elsewhere [94].

3.1   Pyrometry

A radiation pyrometer is a non-contact temperature measurement device which takes in incident thermal radiation, converts it to a signal intensity, and outputs a calculated temperature [95]. The general form of signal intensity is given in Equation (3.1) [96].

$$S = \int \int \int R(\lambda)\tau(\lambda)I_\lambda(\lambda, T)\partial A_t cos\Theta \partial\omega_t \partial\lambda \qquad (3.1)$$

S is the signal intensity, λ is the wavelength, T is the temperature of the target, R is the responsivity of the detector, τ is the transmissivity of the optical path, A_t is the target area, Θ is the angle between the target surface normal

---

[1]Institut für Materialphysik im Weltraum,
Deutsches Zentrum für Luft- und Raumfahrt (DLR),
Linder Höhe, 51147 Cologne, Germany

and the optical vector, ω_t is the angle subtended by the detector, and I_λ is the spectral intensity. Assuming a well defined optical path, and a narrow bandpass pyrometer, Equation (3.1) reduces to Equation (3.2).

$$S = K \int I_\lambda(\lambda, T) \partial \lambda \tag{3.2}$$

K is the instrument constant, which includes the transmissivity of the optical path and responsivity of the detector. Narrow bandpass pyrometers operate under a narrow range of wavelengths. Therefore, the spectral intensity, $I_\lambda(\lambda, T)$, only needs to be considered at the effective wavelength of the pyrometer, λ_{eff}. Thus, the spectral intensity is not a function of a broad wavelength range, and the integral in Equation (3.2) can be approximated by the integrand.

Planck's radiation equation, as shown in Equation (3.3) gives the spectral intensity of a black body.

$$I_{\lambda,b}(T) = \frac{2hc^2}{\lambda_{eff}^5 [exp(\frac{hc}{\lambda k_b T_b}) - 1]} = \frac{C_1}{\lambda_{eff}^5} \frac{1}{exp(\frac{C_2}{\lambda_{eff} T_b}) - 1} \tag{3.3}$$

h and k_b are the Plank and Boltzmann universal constants, respectively, c is the speed of light. In the low wavelength infrared range, Wein's approximation can be applied to Planck's blackbody equation, which results in Equation (3.4).

$$I_{\lambda,b}(T) = \frac{C_1}{\lambda_{eff}^5} exp(\frac{-C_2}{\lambda_{eff} T_b}) \tag{3.4}$$

Therefore, the signal intensity corresponding to a black is given as:

$$S_b = K \frac{C_1}{\lambda_{eff}^5} exp(\frac{-C_2}{\lambda_{eff} T_b}) \tag{3.5}$$

From Equation (3.5), it should be clear that it is possible to determine a relationship between the temperature of a blackbody and the corresponding signal intensity. That relationship is given in Equation (3.6).

$$ln(S_{b,0}) - ln(S_{b,1}) = ln\left[\frac{I_{\lambda,b_0}}{I_{\lambda,b_1}}\right] = \frac{-C_2}{\lambda_{eff}}\left[\frac{1}{T_{b,0}} - \frac{1}{T_{b,1}}\right] \qquad (3.6)$$

$T_{b,0}$ and $T_{b,1}$ are arbitrary temperatures of a blackbody, and $S_{b,0}$ and $S_{b,1}$ are the corresponding signal intensity values.

When the temperature of a real surface is evaluated, the pyrometer will interpret the signal intensity as if the surface is a blackbody, and will report the corresponding blackbody temperature which is below the true temperature. This is depicted graphically in Figure 3.1. The initial reported temperature will be referred to as T_{b0}, and the true temperature will be referred to as T_T.
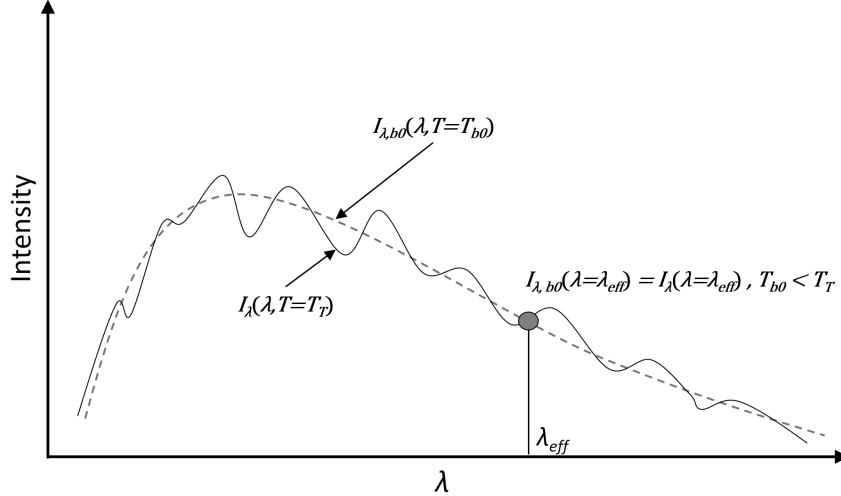
Figure 3.1: Graphical depiction of the spectral intensity of a real surface at it's true temperature, $I_\lambda(\lambda, T = T_T)$, and that of a blackbody which corresponds to the same spectral intensity at $\lambda = \lambda_{eff}$, $I_{\lambda,b0}(\lambda, T = T_{b0})$.

It is necessary to correlate the initial reported temperature of a blackbody, T_{b0}, to the true temperature of the real surface, T_T. That is accomplished by leveraging the definition of emissivity. Figure 3.2 shows the blackbody

curve which corresponds to the measured spectral intensity at $\lambda = \lambda_e ff$, $I_{\lambda,b0}(\lambda, T = T_{b0})$, and the blackbody spectral intensity curve which corresponds to the true temperature of the real surface, $I_{\lambda,b1}(\lambda, T = T_{b1} = T_T)$.
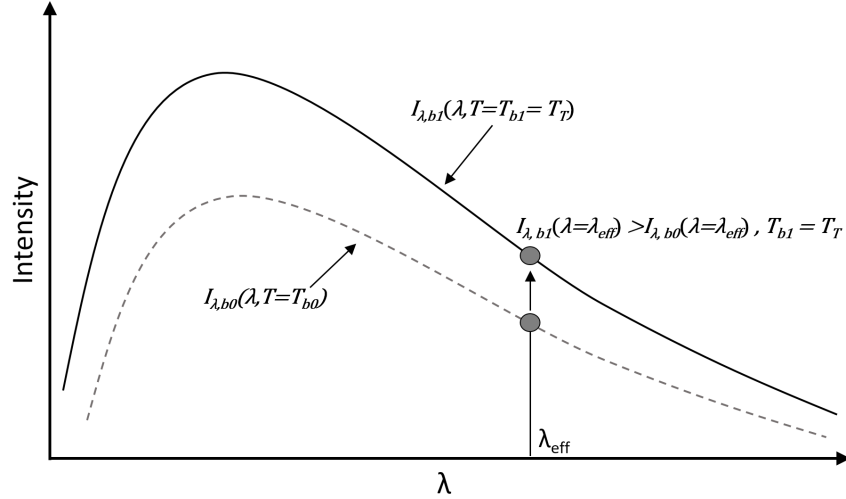
Figure 3.2: Graphical depiction of the blackbody spectral intensity curve which corresponds to the spectral intensity of the real surface, $I_{\lambda,b0}(\lambda, T = T_{b0})$, and the blackbody spectral intensity curve which corresponds to the true temperature of the real surface, $I_{\lambda,b1}(\lambda, T = T_{b1} = T_T)$.

Equation 3.7 gives the relationship between the initial reported blackbody temperature, T_{b0}, and the true temperature, T_T. From Equation 3.7, it becomes clear that the true temperature (reference temperature) must be known in order to determine the correct emissivity value, $\epsilon_{\lambda_{eff}}$. Once the emissivity value is known, the equation can be used to solve for other temperatures.

$$ln\left[\frac{I_{\lambda,b0}}{I_{\lambda,b1}}\right] = ln\left[\frac{I_\lambda}{I_{\lambda,b1}}\right] = ln(\epsilon_{\lambda_{eff}}) = \frac{-C_2}{\lambda_{eff}}\left[\frac{1}{T_{b0}} - \frac{1}{T_T}\right] \tag{3.7}$$

By extension, is it possible to correlate two different surface temperatures, with different emissivity values, so long as the all of the parameters associated with the reference temperature, and the emissivity of the current state of the material, are known. Equation 3.8 gives the relationship between the intensities

37

at two different temperatures.

$$ln\left[\frac{I_\lambda}{I_{\lambda,o}}\right] = \frac{-C_2}{\lambda_{eff}}\left[\frac{1}{T_T} - \frac{1}{T_{T,o}}\right] + ln\left[\frac{\epsilon_{\lambda_{eff}}}{\epsilon_{\lambda_{eff},o}}\right] \tag{3.8}$$

$T_{T,o}$ is the temperature of the reference temperature, where $\epsilon_{\lambda_{eff},o}$ and $I_{\lambda,o}$ are the corresponding emissivity and intensity values.

Within the current work, the emissivity was assumed to be approximately constant with respect to temperature and phase. Typically, any significant shift in emissivity, as a result of a phase change, will be observable in the temperature-time profile; the shift will manifest as an abrupt change in apparent temperature. No such observation was made during heating, or cooling, through the $\alpha \rightleftharpoons \gamma$ and $\gamma \rightleftharpoons Liquid$ phase transitions. The δ–phase is expected to behave similarly, since both α and δ are BCC crystal structures. Previous experimental results, which will be discussed below, support this assumption.

Watanabe *et al.* [97] investigated the spectral emissivities of the solid and liquid phases of iron and cobalt at their melting temperatures for wavelengths between 1 μm and 1.9 μm. The maximum observed emissivity shifts for iron and cobalt, between 1.45 μm and 1.8 μm, were 6.9% and 8.5%, respectively.

Wahlin and Knop [98] reported on the emissivity of iron between 1100 K and 1730 K, and cobalt between 1200 K and 1450 K. Their results correspond to a wavelength of 0.667 μm. They found that the emissivities for a given phase were nearly independent of temperature. The emissivity of iron decreased by 5.9% across the $\alpha \rightleftharpoons \gamma$ transition, and increased by 4.2% across the $\gamma \rightleftharpoons \delta$ transition. The emissivity of cobalt decreased by 4.2% between 1200 K and 1240 K, and then remained constant until the curie temperature was reached, where it increased by 4.8%.

Knop [99] evaluated the emissivity of Fe–60 wt.% Co. for 975 K $< T <$ 1540 K, at a wavelength of 0.667 μm. There are some abrupt changes in emissivity near the curie temperature, between 1000 K and 1100 K. The emissivity levels off thereafter, and then decreases by 8.1% across the $\alpha \rightleftharpoons \gamma$ transition. Between 1290 K and 1540 K, the emissivity was approximately constant.

Chapter 4

Thermodynamic Modeling

As previously stated, containerless processing facilitates observation of the metastable phase. The minimum undercooling required to achieve double recalescence is equal to the temperature difference between the BCC and FCC liquidus temperatures, $\Delta T_{\gamma\delta}$ [100]. The observed temperatures of the metastable δ–phase correspond to the liquidus temperatures of the BCC-Liquid relationship when it is extended beyond the peritectic into the area where the FCC phase is stable. Therefore, these data points expand the cobalt composition range over which BCC-Liquid equilibrium can be observed, thus providing insight into improving thermophysical property evaluations which characterize these transformations.

The metastable phase diagram can be calculated by suppressing (not calculating) the stable (FCC) phase, and evaluating the BCC-Liquid relationship below the peritectic temperature [8, 101]. Given the phase diagram, the temperature of the metastable phase can then be superimposed onto the equilibrium phase diagram, as seen in Figure 4.1. The phase diagram was calculated using Thermo-Calc, Version 8 (2015b), with the PBIN database.
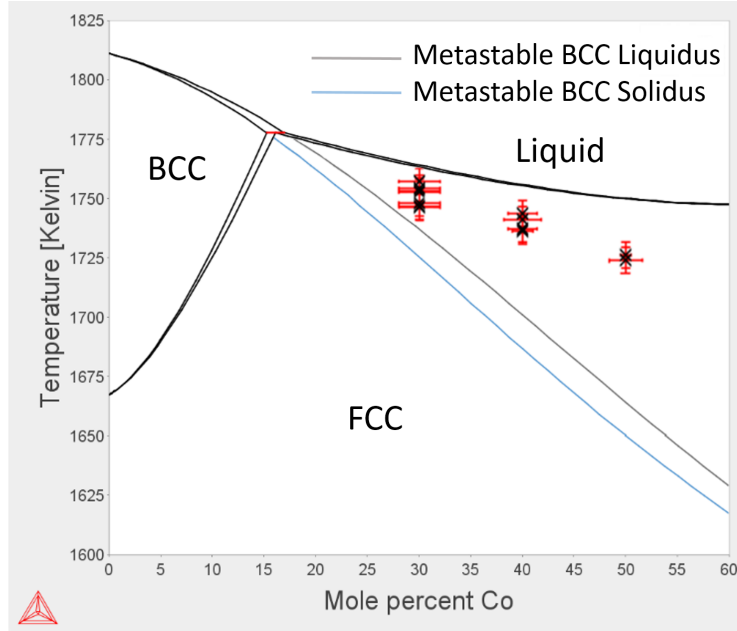
Figure 4.1: Fe–Co equilibrium phase diagram with metastable phase lines calculated in Thermo-Calc. Data points correspond to observations of the actual metastable transformation temperature from electrostatic levitation tests. Cobalt composition error bars correspond to the evaporation that occurred during the experiment, under the worst case scenario that all of the evaporation was from one component of the system. Temperature error bars correspond to the accuracy of the pyrometer at the given temperature, ± 0.3% of reading in °F + 1.8 °F.

The importance of the accuracy of the metastable phase diagram becomes more evident when considering dendrite growth analysis. The growth rate of the metastable phase is a function of its relative undercooling, as well as its partitioning coefficient and liquidus slope [72]. If the thermal driving potential ($\Delta T_{\gamma\delta}$) for transformation between the BCC and FCC phases is known (as well as several other parameters), then it is possible to calculate the heat flux from the stable phase dendrite as it grows through the metastable phase. That value can then be applied to a given dendrite growth model such that growth velocity can be calculated [100].

Previously accepted thermodynamic models for Fe-Co fall short in one of two ways. The first is that the model does not accurately represent the metastable

phase, which is a result of errors propagated from the analysis of the stable phase. The second consists of a misrepresented stable phase diagram, which is a result of optimizing the fitting parameters for either high-temperature Liquid-Solid equilibrium or low-temperature Solid-Solid transformations.

The goal of this work is to demonstrate the applicability of metastable temperature data within equilibrium phase diagram modeling. In doing this, the location of the FCC-BCC-liquid peritectic will be better resolved, there will be a better ability to predict driving potential for solidification in undercooling experiments, and the metastable partitioning coefficient will be obtained. Additionally, the thermophysical properties that are associated with the metastable phase will be more accurately represented, and the solution activity may be determined as a function of the constituents such that evaporation during thermal processing may be predicted.

4.1   Analysis

In this section, the methodology for modifying the free energy parameters in Equations (2.4)-(2.10) will be described. See Section 2.2.1 for a complete description of the thermodynamic model for the Fe–Co system. Based on the analysis of previous work, it was decided that the magnetic and pressure contributions would not be modified for any phase. Table 4.1 gives the parameters that are used to calculate the magnetic component of the free energy for the Fe–Co system. The parameters that are used to calculate the pressure contribution for iron and cobalt are given in Tables 4.2 and 4.3.

The primary relationships that determine the high temperature free energy parameters for the solid phases, where $T > T_m$, are: the enthalpy and entropy

Table 4.1: Parameters used in Equations (2.11)-(2.16) to calculated the magnetic contribution to the free energy [35].

Parameters	BCC	FCC*	HCP
$T_{c_{Co}}^{\alpha}$	1450	1396	1396
$T_{c_{Fe}}^{\alpha}$	1043	-201	0
$T_{c_{Co,Fe}}^{0,\alpha}$	590	283	-253
$T_{c_{Co,Fe}}^{1,\alpha}$	0	879	1494
B_{Co}^{α}	1.35	1.35	1.35
B_{Fe}^{α}	2.22	-2.1	0
$B_{Co,Fe}^{0,\alpha}$	2.4127	9.74	5.41
$B_{Co,Fe}^{1,\alpha}$	0.2418	-3.516	-0.24
p	0.4	0.28	0.28

* For $x_{Co} < 0.152$, the values of β and T_c, calculated with Equations (2.12) and (2.16), are divided by -3.

Table 4.2: Parameters used in Equation (2.7) to calculated the pressure contribution to the free energy for pure Fe [33].

Parameters	BCC	FCC	HCP	Liquid
V_o (J/mol)	7.042095E-06	6.688726E-06	6.59121E-06	6.62574E-06
a_0 (K^{-1})	2.3987E-05	7.3097E-05	7.3646E-05	1.07895E-04
a_1 (K^{-2})	2.569E-08	0	0	0
a_2 (K)	0	0	0	-25.79493
K_0 (Pa^{-1})	5.965E-12	6.2951E-12	6.2951E-12	7.5475E-13
K_1 (Pa^{-1} K^{-1})	6.5152E-17	6.5152E-17	6.5152E-17	4.8509E-15
K_2(Pa^{-1} K^{-2})	0	0	0	0
n	4.7041	5.1665	5.1665	6.59834

Table 4.3: Parameters used in Equation (2.7) to calculated the pressure contribution to the free energy for pure Co [34, 35].

Parameters	BCC	FCC	HCP	Liquid
V_o (J/mol)	6.8148E-06	6.7529274E-06	6.719875E-06	6.4650793E-06
a_0 (K^{-1})	3.207E-05	3.20701588E-05	3.45819359E-05	1.012169928E-04
a_1 (K^{-2})	2.93427E-09	5.86834503E-09	5.58753394E-09	-8.3E-09
a_2 (K)	0	0	0	0
K_0 (Pa^{-1})	4.66592E-12	4.66591978E-12	4.51215767E-12	5.06841984E-12
K_1 (Pa^{-1} K^{-1})	1.4593E-17	1.45932992E-15	1.60731053E-15	4.32537907E-15
K_2(Pa^{-1} K^{-2})	5.174E-20	5.1736842E-20	4.66728911E-20	0
n	4.007	4.007	4.007	4.5925

calculations from low and high temperature free energy equations must be equal at $T = T_m$, and the heat capacity of the solid phases must approach that of the liquid phase. The high temperature enthalpy and entropy relationships are directly linked to $a_e^{\alpha,H}$ and $b_e^{\alpha,H}$ respectively, and the approach of the solid phase heat capacity to that of the liquid phase is related to $j_e^{\alpha,H}$. The same

relationships apply to the liquid phase, except that for $T < T_m$ the liquid phase heat capacity approaches that of the stable solid phase at room temperature, governed by j_e^{Liq} and the low temperature liquid parameters a_e^{Liq} and b_e^{Liq} are linked to the low temperature enthalpy and entropy calculations.

The phases of iron are well documented, therefore, in this work few modifications were applied to the free energy parameters of iron. b_{Fe}^{BCC} was reduced slightly in order to maintain a good representation of the high temperature BCC-FCC relationship. The heat capacities were reevaluated assuming a hypothetical nonmagnetic state, and $j_{Fe}^{\alpha,H}$ and j_{Fe}^{Liq} were adjusted for the solid and liquid phases respectively, based on the specifications from Guillermet [33, 34]. The high temperature solid parameters, $a_{Fe}^{\alpha,H}$ and $b_{Fe}^{\alpha,H}$, were then determined based on the previously mentioned conditions. Similarly, a_{Fe}^{Liq} and b_{Fe}^{Liq} were found, while $a_{Fe}^{Liq,H}$ was modified simultaneously such that the BCC-Liquid relationship was better represented.

The parameters concerning cobalt were modified more extensively. Calorimetry experiments on liquid cobalt [102, 103] show similar values for heat capacity and enthalpy. The heat capacity of 45.98 J/mol-K, and enthalpy values, were taken from Hess [102], while the entropy values reported by Treverton [103] were applied. Using the new liquid heat capacity values for $-c_{Co}^{Liq,H}$, and $-c_{Co}^{\alpha,H}$ for the solid phases, the terms $j_{Co}^{\alpha,H}$ and j_{Co}^{Liq} were calculated in the same manner that they were for iron. The parameters a_{Co}^{BCC} and $_bCo^{BCC}$ were also considered to be adjustable since BCC cobalt is a hypothetical phase, and there can't be an evaluation of the enthalpy or entropy of the phase [35]. The solid phase parameters $a_{Co}^{\alpha,H}$, and $b_{Co}^{\alpha,H}$, were obtained in the same way that they were for iron. $a_{Co}^{Liq,H}$ and $b_{Co}^{Liq,H}$ were then established based on the new enthalpy and entropy values for liquid cobalt. Lastly, a_{Co}^{Liq}, and b_{Co}^{Liq} were calculated such that

the low and high temperature enthalpy and entropy calculations were equal at $T = T_m$.

The equation for calculating the excess free energy, Equation 2.8, shows that for pure iron or cobalt, the excess free energy goes to zero. This is critical, as it highlights the fact that the excess free energy applies only to the Fe–Co system, and does not affect the pure element properties. Any modifications made to the excess free energy parameters will directly influence the Fe-Co phase diagram, as well as the thermophysical properties, while those of the pure elements will remain unchanged.

The optimization process was a combination of automated evaluation with a final manual check. The thermophysical property relationships, as well as the desired free energy relationships, were used to calculate an initial set of excess free energy parameters, as well as a_{Co}^{BCC} and b_{Co}^{BCC}, via a weighted least-square-error process. The weights were selected by personal judgment based on which section of the phase diagram was to be optimized. After optimization, the parameters were re-adjusted manually such that the available experimental data remained accurately represented. It should be noted that no modifications were made to the pressure contribution for iron or cobalt.

Once all of the parameters had been determined, the free energy curves for each phase were calculated, as a function of compositions, at temperatures ranging from 300 K to 1811 K. At a given temperature, the tangent line that corresponded to the lowest free energy curves was drawn, and those points where the line touched the curves were taken to be points on the phase diagram. As previously stated, the metastable phase lines were found by suppressing the FCC phase (not calculating it) and repeating the procedure using only the BCC and liquid free energy curves. This concept is demonstrated in Figures 4.2

and 4.3. Figure 4.2 shows the free energy curves of the BCC, FCC, and liquid phases at T = 1650 K, and indicates that the FCC phase is the stable phase across the entire composition range. If the FCC phase is suppressed, as shown in Figure 4.3, the metastable BCC-Liquid relationship can be evaluated.
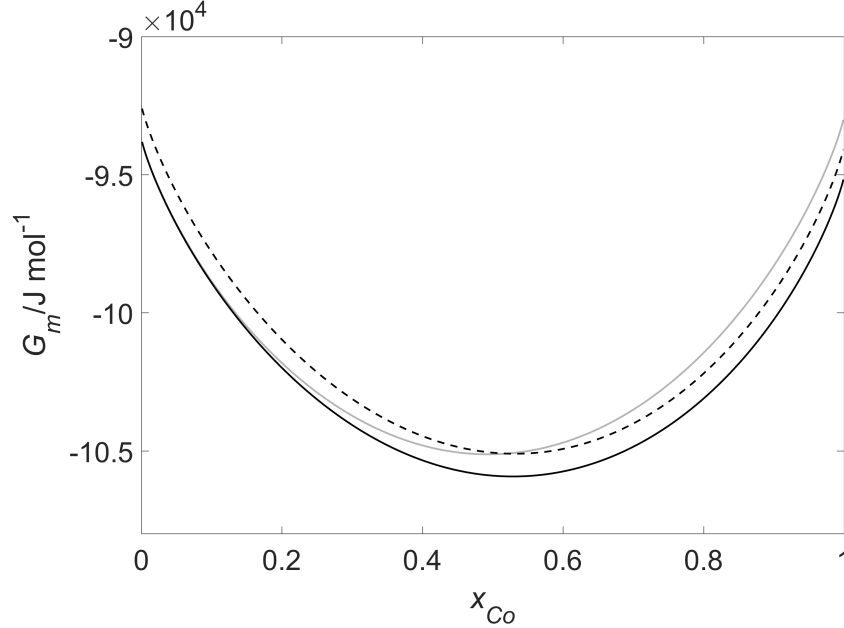
Figure 4.2: Free energy curves of the BCC, FCC, and Liquid phases of Fe–Co, at T = 1650 K, calculated using parameters from Dinsdale [37] and Guillermet [33–35]. —— BCC; —— FCC; - - - - Liquid. The curves indicate that the FCC phase is stable across the entire composition range.

In the following sections, comparisons of thermophysical properties and phase diagram results will be provided. In each of these cases, where a comparison of results from an empirical equation is provided, all of the figures were generated using the fundamental thermodynamic relationships related to the free energy. This method allows for comparison of results that were not explicitly depicted graphically in previous literature.
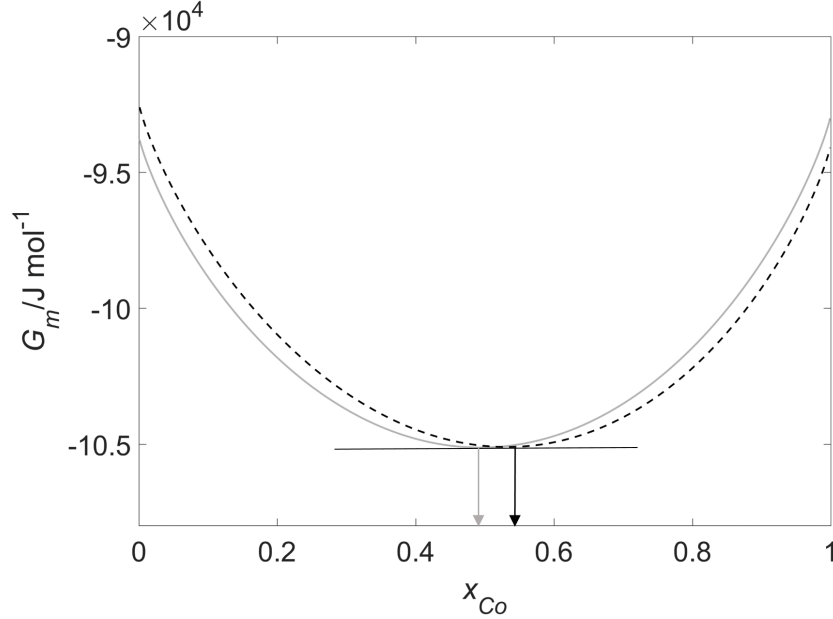
Figure 4.3: Free energy curves of the BCC, and Liquid phases of Fe–Co, at T = 1650 K, calculated using parameters from Dinsdale [37] and Guillermet [33–35]. —— BCC; - - - - Liquid. With the FCC phase suppressed, the metastable BCC-Liquid relationship is demonstrated. The arrows identify the metastable BCC solidus and liquidus compositions at the given temperature.

4.2 Results and Discussion

4.2.1 Experimental Results

Figures 4.4 and 4.5 show the delay times for samples that solidified via double recalescence. The delay times of the 40 and 50 at.% Co EML samples are approximately an order of magnitude smaller than those of the ESL samples. This supports the results of Matson *et al.* [25, 26].

One thing to note is that if the delay time of the metastable phase is less than the pyrometer's time step, the metastable phase will not be observed in the temperature-time profile. In the event that the delay time is slightly greater than the pyrometer's time step, the metastable phase may or may not be seen in the temperature-time profile since at least 2 data points are required to

indicate a plateau. The best practice for verifying the type of solidification is to implement a high-speed camera, however, a high-speed pyrometer could also be an effective option.
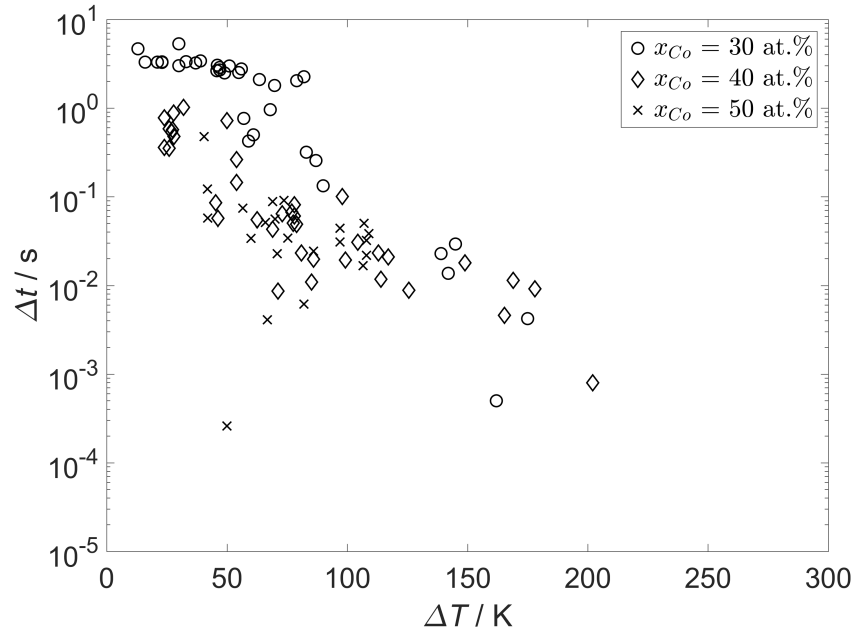
Figure 4.4: Delay time of ESL samples as a function of undercooling.

Table 4.4 shows the results of the solidification experiments for samples where double recalescence was observed in the pyrometer data.
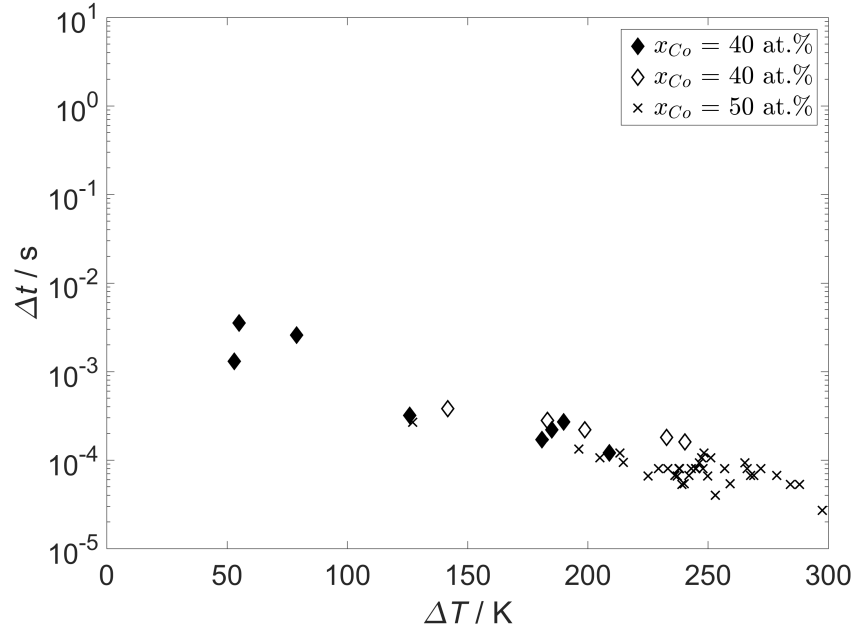
Figure 4.5: Delay time of EML samples as a function of Undercooling. ◆ [104]; ◇ and ✕ from collaboration with Thomas Volkmann and Carolina Kreischer at Deutsches Zentrum für Luft- und Raumfahrt (DLR), Linder Höhe, 51147 Cologne, Germany [105].

Table 4.4: Temperature data for samples that exhibited double recalescence in pyrometer plots. x_{Co} is the initial cobalt composition, Melt Cycle refers to the number of times that the sample was melted and solidified, ΔT is the total undercooling, ΔT_δ is the undercooling relative to the observed temperature of the metastable phase, and T_δ is the observed temperature of the metastable phase.

Sample	x_{Co}	Melt Cycle	$\Delta T/K$	$\Delta T_\delta/K$	T_δ/K
1	0.3006	1	16	10	1758
		2	55	44	1753
		3	64	47	1747
		4	46	31	1748
		5	21	11	1754
2	0.2998	2	70	53	1747
		3	96	87	1755
		4	90	74	1747
3	0.3999	1	28	10	1738
		3	21	9	1744
4	0.4003	4	32	18	1741
5	0.3995	2	27	8	1737
6	0.4991	1	74	50	1727
7	0.4993	2	41	15	1724

4.2.2 Parameter Modification

Table 4.5: Paramaters that were modified in $G_{Fe}^{o,\alpha}$ (non-magnetic state). The bolded text shows where parameter changes were made.

	[37] BCC	Current BCC	[37] FCC	Current FCC	[37] HCP	Current HCP	[37] Liquid	Current Liquid
a_{Fe}^{α}	1225.7	1225.7	-236.7	-236.7	-2480.08	-2480.08	**13265.87**	**13228.6588**
b_{Fe}^{α}	**124.134**	**124.131**	132.416	132.416	136.725	136.725	**117.57557**	**117.586673**
c_{Fe}^{α}	-23.5143	-23.5143	-24.6643	-24.6643	-24.6643	-24.6643	-23.5143	-23.5143
d_{Fe}^{α}	-4.39752 E-03	-4.39752 E-03	-3.75752 E-03	-3.75752 E-03	-3.75752 E-03	-3.75752 E-03	-4.39752 E-03	-4.39752 E-03
e_{Fe}^{α}	-5.8927 E-08	-5.8927 E-08	-5.8927 E-08	-5.8927 E-08	-5.8927 E-08	-5.8927 E-08	-5.8927 E-08	-5.8927 E-08
f_{Fe}^{α}	77359	77359	77359	77359	77359	77359	77359	77359
j_{Fe}^{α}	0	0	0	0	0	0	**-3.67516 E-21**	**-3.72027306 E-21**
$a_{Fe}^{\alpha,H}$	**-25383.581**	**-25375.52878**	**-27097.396**	**-27086.23614**	**-29340.776**	**-29329.61614**	**-10838.83**	**-10858.83**
$b_{Fe}^{\alpha,H}$	**299.31255**	**299.305549**	**300.252559**	**300.247012**	**304.561559**	**304.556012**	291.302	291.302
$c_{Fe}^{\alpha,H}$	-46	-46	-46	-46	-46	-46	-46	-46
$j_{Fe}^{\alpha,H}$	**2.29603 E+31**	**2.27924512 E+31**	**2.78854 E+31**	**2.76527491 E+31**	**2.78854 E+31**	**2.76527491 E+31**	0	0

Table 4.6: Paramaters that were modified in $G_{Co}^{o,\alpha}$ (non-magnetic state). The bold text shows where parameter changes were made.

	[37] BCC	Current BCC	[37] FCC	Current FCC	[37] HCP	Current HCP	[37] Liquid	Current Liquid
a_{Co}^{α}	**3248.241**	**3220.37184**	737.832	737.832	310.241	310.241	**15395.278**	**12746.715508**
b_{Co}^{α}	**132.65221**	**131.98244**	132.750762	132.750762	133.36601	133.36601	**124.434078**	**126.057218**
c_{Co}^{α}	-25.0861	-25.0861	-25.0861	-25.0861	-25.0861	-25.0861	-25.0861	-25.0861
d_{Co}^{α}	-2.654739E-03	-2.654739E-03	-2.654739E-03	-2.654739E-03	-2.654739E-03	-2.654739E-03	-2.654739E-03	-2.654739E-03
e_{Co}^{α}	-1.7348E-07	-1.7348E-07	-1.7348E-07	-1.7348E-07	-1.7348E-07	-1.7348E-07	-1.7348E-07	-1.7348E-07
f_{Co}^{α}	72527	72527	72527	72527	72527	72527	72527	72527
j_{Co}^{α}	0	0	0	0	0	0	**-2.19801E-21**	**-6.4701028E-21**
$a_{Co}^{\alpha,H}$	**-14259.666**	**-25044.494656**	**-16770.075**	**-27527.034499**	**-17197.666**	**-27954.625499**	**-846.61**	**-11799.7**
$b_{Co}^{\alpha,H}$	**252.56994**	**298.901272**	**252.668492**	**299.669594**	**253.28374**	**300.284842**	**243.599944**	**290.767**
$c_{Co}^{\alpha,H}$	**-40.5**	**-45.98**	**-40.5**	**-45.98**	**-40.5**	**-45.98**	**-40.5**	**-45.98**
$j_{Co}^{\alpha,H}$	**9.3488E+30**	**2.73811289E+31**	**9.3488E+30**	**2.73811289E+31**	**9.3488E+30**	**2.73811289E+31**	0	0

Table 4.7: Excess Gibbs energy parameters that were modified in $L_{Co,Fe}^{0,\alpha}$ and $L_{Co,Fe}^{1,\alpha}$. The bold text shows where parameter changes were made.

	[35]	Current	[35]	Current	[35]	Current	[35]	Current
	BCC	BCC	FCC	FCC	HCP	HCP	Liquid	Liquid
$a^{0,\alpha}$	**-23669**	**-29437.347**	**-8471**	**-7776.797199**	**-400**	**1281.801529**	**-9312**	**-8385.97986**
$b^{0,\alpha}$	**103.963**	**164.217752**	0	0	0	0	0	0
$c^{0,\alpha}$	**-12.7886**	**-20.32034**	0	0	0	0	0	0
$a^{1,\alpha}$	**0**	**-1158.60079**	**1181**	**-4177.993893**	**0**	**-4914.888372**	**-1752**	**-1381.69775**
$b^{1,\alpha}$	**0**	**0**	**-1.6544**	**1.326825**	**0**	**0**	**0**	**0**

Tables 4.5, 4.6, and 4.7 show the results of the parameter optimization. The parameters for iron and cobalt (Tables 4.5 and 4.6) are transferrable to other analyses involving those elements, where the magnetic contribution is calculated independently as part of the free energy of the system.

Figure 4.6 shows the Fe-Co phase diagram that was generated using the parameters provided in the current work, as well as the accepted phase diagram, and the phase diagram that is generated using parameters from Woodcock [38]. The accepted phase diagram uses pure element parameters from Dinsdale [37], and excess, magnetic, and pressure free energy values from Guillermet [35]. The analysis yielded results that fit the experimental data across the entire range of compositions and temperatures.

The phase diagram shows the melting temperature of iron and cobalt to be 1809 K and 1766.9 K, respectively. Harris [44] reported the melting temperature of iron to be 1534 °C ± 2 °C, and Roeser [106] reported a melting temperature of 1539 °C ± 1. When corrected to the latest International Temperature Scale, ITS – 90 [107], and converted to Kelvin, those temperatures become 1809 K ± 2 K and 1811.4 K ± 2 K. Stimson [108] listed the melting temperature of cobalt to be 1492 °C, while VanDusen [109] provided a value of 1495 °C ± 1 °C. Correcting those values to ITS – 90, and converting to Kelvin, yields results of 1766.9 K and 1767.6 K ± 1 K. The melting temperature of iron that is given in this work agrees with that provided by Harris [44]. The melting temperature of

cobalt agrees with that specified by Stimson [108], and falls within the bounds of the value given by VanDusen [109].
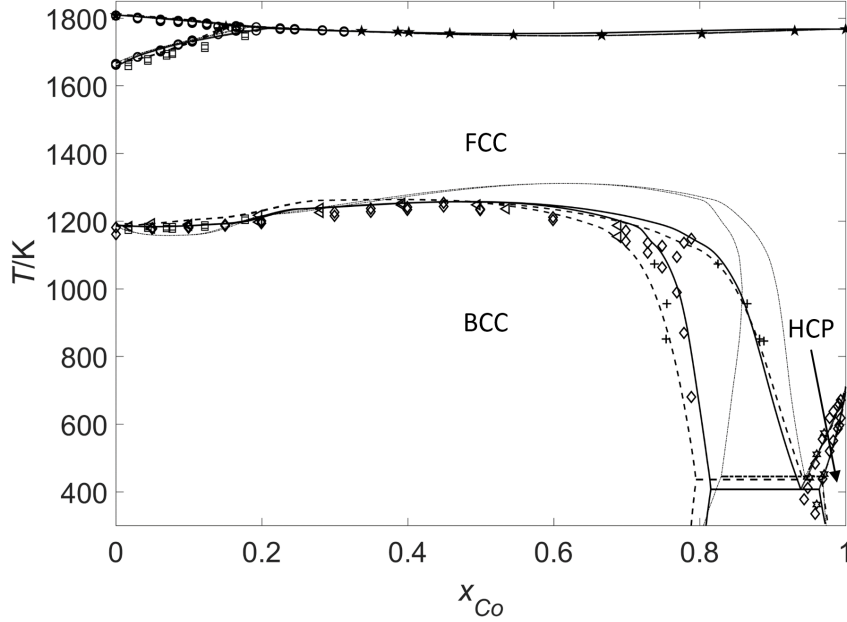
Figure 4.6: Equilibrium phase diagram according to the current work and previous models as well as previous experimental data: —— Current; - - - - [35, 37]; ······ [38]; + [39]; □ [42]; ○ [44]; ◇ [40]; ◁ [43]; ☆ [45].

The high temperature peritectic occurs at T = 1769.7 K, where $x_{Co,BCC}$ = 0.204, $x_{Co,FCC}$ = 0.209, and $x_{Co,LIQ}$ = 0.217. The low temperature eutectoid occurs at T = 406.9 K, where $x_{Co,BCC}$ = 0.815, $x_{Co,FCC}$ = 0.939, and $x_{Co,HCP}$ = 0.964. The low temperature parameters were used for all analyses of a given component below its melting point, while high temperature parameters were used for all evaluations above the component melting point.

A closer view of the high temperature region of the phase diagram is shown in Figure 4.7. The BCC-Liquid and BCC-FCC relationships show good agreement with experimental data points. There is limited data available for the FCC-Liquid relationship, however the phase diagram agrees well in low to mid cobalt composition range. For cobalt compositions between 0.55 and 0.9, the liquidus temperature is within ~ 7 K of the experimental results from Predel [45].
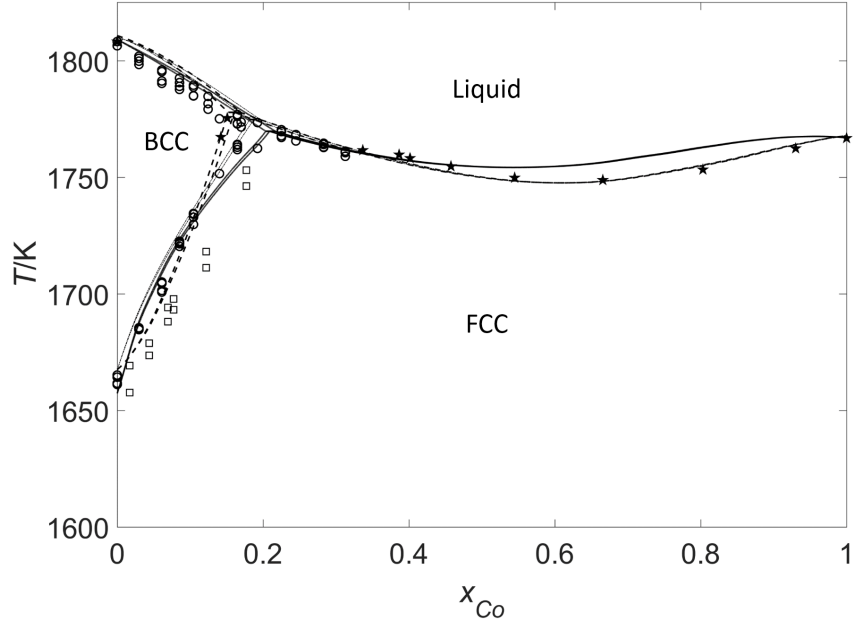
Figure 4.7: High temperature portion of the equilibrium phase diagram according to the current work and previous models as well as previous experimental data: —— Current; - - - - [35, 37]; ------- [38]; ☐ [42]; ○ [44]; ☆ [45].

4.2.3   Parameter Validation

In addition to ensuring that the phase diagram matched the experimental results, it was necessary to validate the parameter modifications by comparing thermophysical property calculations to experimental results.

The enthalpy and entropy calculations for liquid cobalt can be found in Figures 4.8 and 4.9 respectively; there is good agreement between the calculated and experimental values. In short, the results show that the liquid parameters that were modified for pure cobalt are supported by previous experimental results.

The enthalpy and entropy values for liquid cobalt can be calculated using Equations 4.1 and 4.2 respectively.

$$H_{Co}^{Liq}(J \cdot mol^{-1}) = 45.98T - 11800 \tag{4.1}$$

$$S_{Co}^{Liq}(J \cdot mol^{-1}K^{-1}) = -4.4191E - 6T^2 + 0.040546T + 41.2518 \tag{4.2}$$
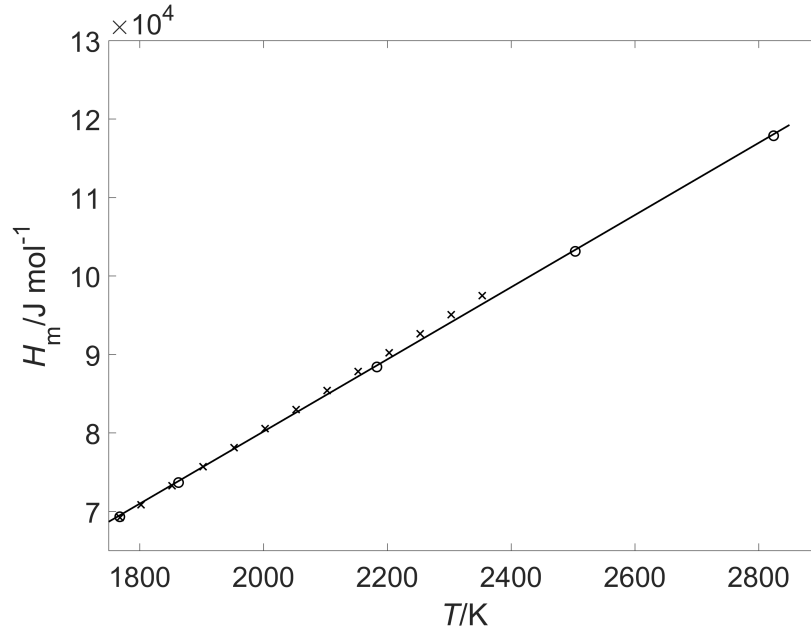
Figure 4.8: Enthalpy calculation for liquid cobalt, with experimental data points: ——— Enthalpy calculated using Equation (4.1); ○ [102]; ✕ [103]

The heat capacity, enthalpy, and entropy of each of the Fe-Co phases can also be determined since the free energy equation is known. The heat capacity was calculated as a function of temperature at various cobalt compositions and is given in Figure 4.10. The discontinuity that is observed is a result of the BCC-FCC transition.

Similarly, the enthalpy of formation was calculated and plotted at various temperatures, and these can be found in Figures 4.11, 4.12, and 4.13. In Figure 4.11 the BCC-FCC transition can be observed in the ~0.72-0.77 cobalt atomic fraction range, where the BCC phase is to the left, and the FCC phase is to the right. The abrupt change in the enthalpy of formation near $x_{Co} = 0.1$
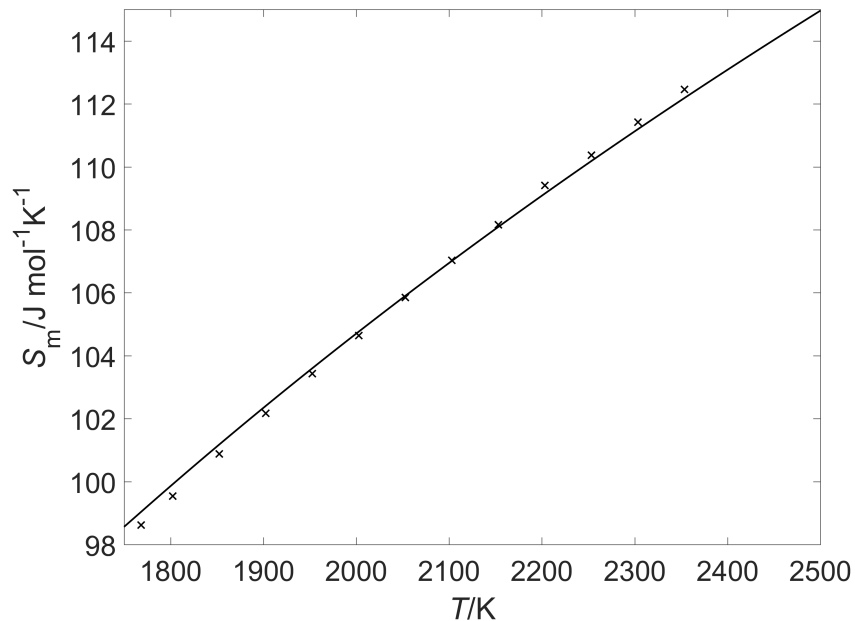
Figure 4.9: Entropy calculation for liquid cobalt, with experimental data points: ——— Entropy calculated using Equation (4.2); $\times$ [103].
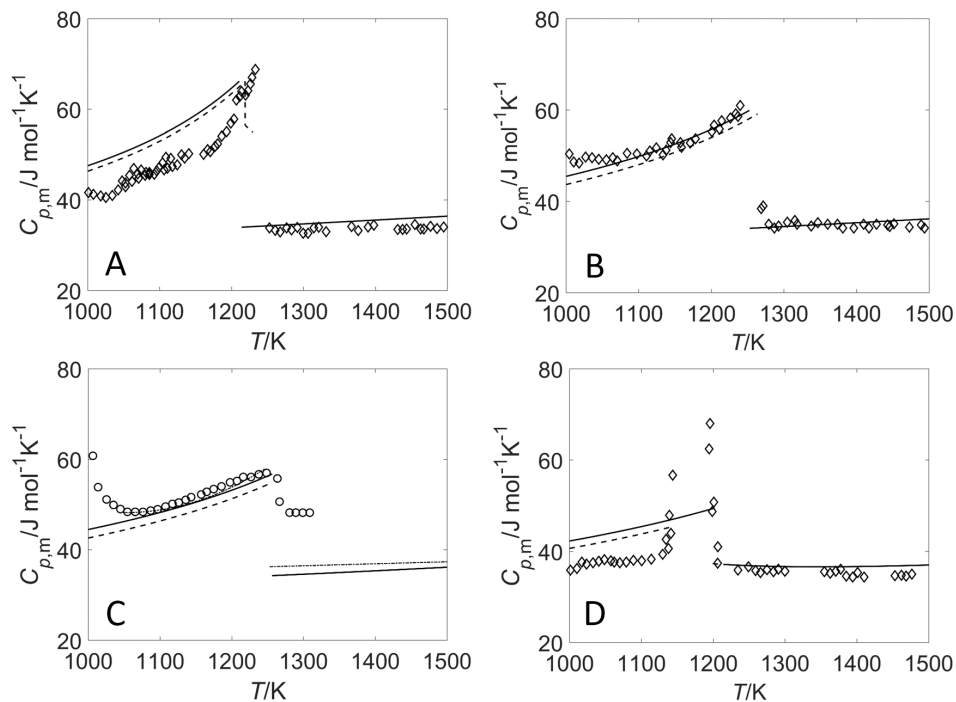
Figure 4.10: Heat capacities at A) $x_{Co} = 0.2001$, B) $x_{Co} = 0.3916$, C) $x_{Co} = 0.5$ and D) $x_{Co} = 0.6882$ from $T = 1000$ K to $T = 1500$ K: ——— Current; - - - - [35,37]; ·--·--· [46]; $\diamond$ [43]; $\bigcirc$ [47].

is a result of crossing the Curie point of the BCC phase. The enthalpy of formation given in Figure 4.12 shows a minimum at $x_{Co} \approx 0.75$, while that which is calculated using the parameters from previous works [35, 37] shows a minimum at $x_{Co} \approx 0.37$.
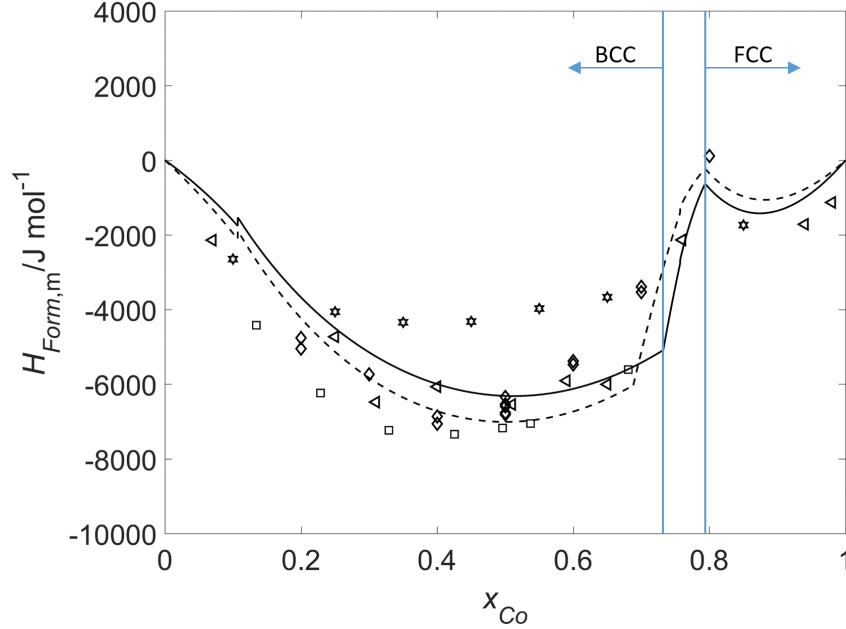
Figure 4.11: Enthalpy of formation as a function of cobalt composition at $T = 1143$ K: —— Current; - - - - [35, 37]; $\Diamond$ $T = 1143$ K [46]; $\triangleleft$ $T = 1143$ K [49]; $\star$ $T = 1173$ K [50]; $\Box$ $T = 1093$ K [48].

The previously mentioned Figures serve to validate the selection of the free energy parameters. The heat capacities and enthalpies of formation reasonably agree with the experimental data that exists.

Based on the free energy analysis, the activities of iron and cobalt were found as a function of composition at various temperatures. In Figures 4.14 and 4.15, the activities, a, of iron and cobalt are compared to experimental data at $T = 1473$ K and $T = 1873$ K.

In order to simplify the process of calculating the activity, a system of equations was found such that the activity of iron and cobalt can be calculated as a
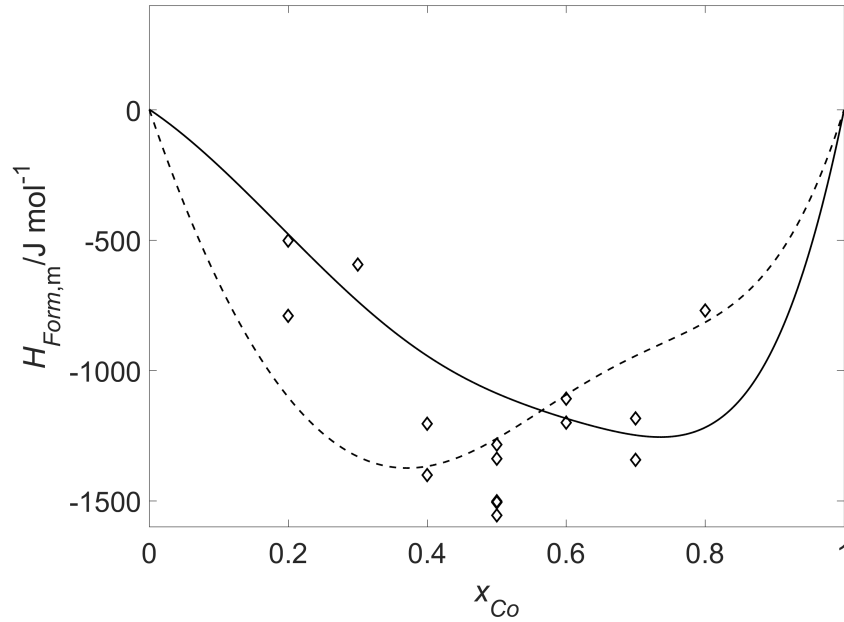
Figure 4.12: Enthalpy of formation as a function of cobalt composition at $T = 1473$ K: —— Current; ---- [35, 37]; $\diamondsuit$ $T = 1473$ K [46].
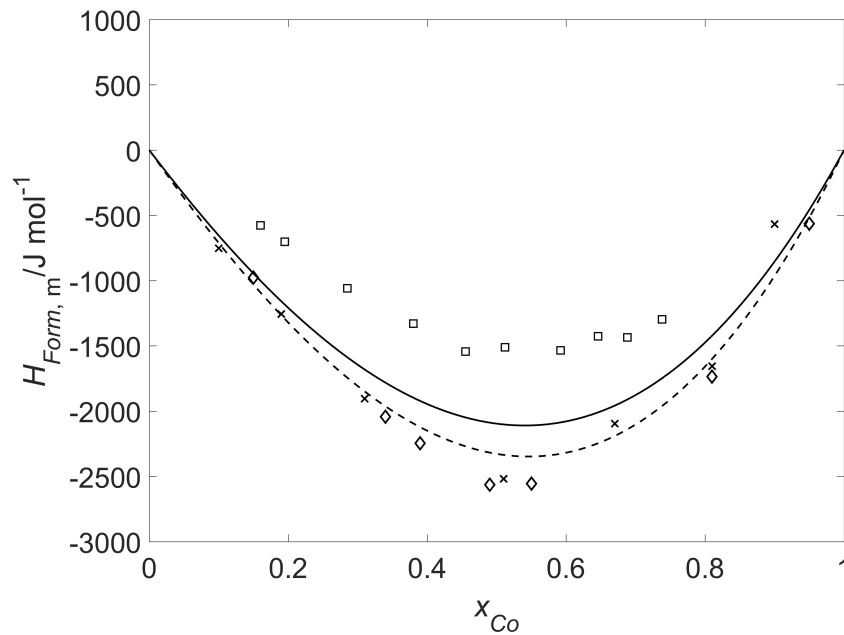
Figure 4.13: Enthalpy of formation as a function of cobalt composition at $T = 1873$ K: —— Current; ---- [35, 37]; $\diamondsuit$ $T = 1873$ K [45]; $\square$ $T = 1873$ K [51]; $\times$ $1823 < T < 1863$ K [52].

function of temperature and composition. First, the coefficients for a 2nd order equation that relates activity to temperature were found at various cobalt
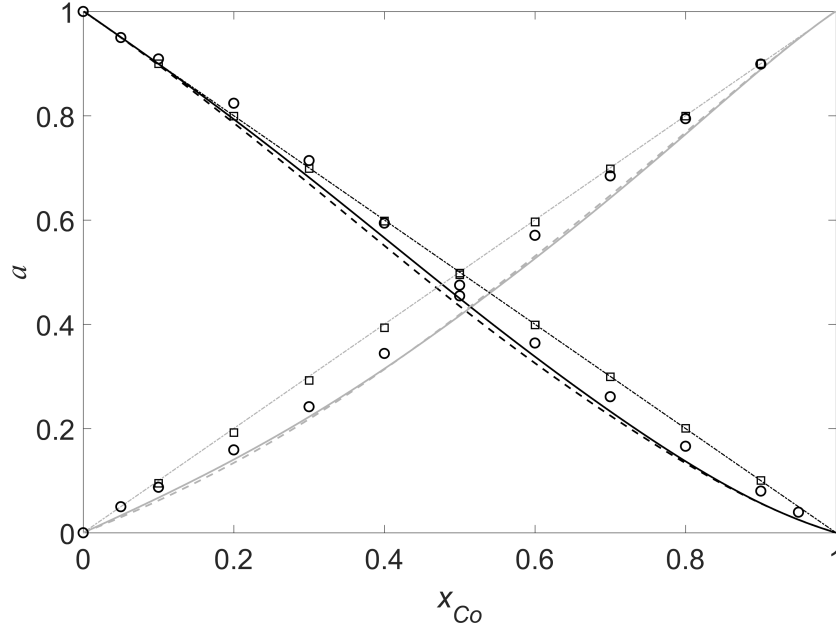
Figure 4.14: Activity calculations for iron and cobalt at T = 1473 K, as compared with the previous analysis and other experimental data of similar temperature: ——— Current a_{Fe}; ——— Current a_{Co}; - - - - a_{Fe} [35, 37]; - - - - - a_{Co} [35, 37]; ------- Ideal a_{Fe}; -------- Ideal a_{Co}; ◯ T = 1473 K [53]; ▢ T = 1500 K [54].

compositions ranging from x_{Co} = 0 to x_{Co} = 1, in increments of 0.05. Next, the coefficients for a 6th order equation which relates the activity equation coefficients to cobalt composition were found. Thus, the activity equation coefficients could be found as a function of composition, and those coefficients could then be plugged into the activity calculation to determine the activity as a function of temperature. The equation to calculate the activity of iron or cobalt, between the temperatures 1300 K and 2300 K, can be found in the following equation:

$$a_e = a_{e(x_{Co})}T^2 + b_{e(x_{Co})}T + c_{e(x_{Co})}. \tag{4.3}$$

The subscript e corresponds to either iron or cobalt, depending on which element is being analyzed. Each of the coefficients in Equation 4.3 can be
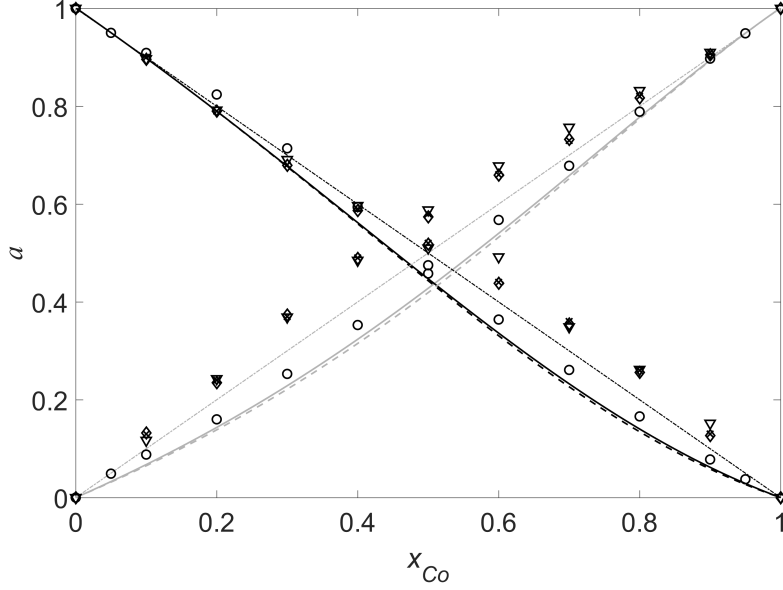
Figure 4.15: Activity calculations for iron and cobalt at T = 1473 K, as compared with the previous analysis and other experimental data of similar temperature: —— Current a_{Fe}; —— Current a_{Co}; - - - - a_{Fe} [35,37]; - - - - - a_{Co} [35,37]; ------- Ideal a_{Fe}; ------- Ideal a_{Co}; ○ T = 1873 K [53]; ◇ T = 1863 K [57]; ✕ T = 1873 K [58]; ▽ T = 1873 K [56].

calculated as a function of composition using a 6th order equation, in the form the following equation:

$$X_{e,(x_{Co})} = A_e x_{Co}^6 + B_e x_{Co}^5 + C_e x_{Co}^4 + D_e x_{Co}^3 + E_e x_{Co}^2 + F_e x_{Co} + G_e \qquad (4.4)$$

The coefficients used in Equation 4.4 are given in Tables 4.8 and 4.9. The reason that the coefficients in Tables 4.8 and 4.9 have different temperature boundary conditions is because the temperature dependent coefficients in the activity equation show slightly different trends. The activity of iron becomes more linear at $T \approx 1800$ K and the activity of cobalt becomes more linear at $T \approx 1700$ K. This could be due to the slight difference in the melting temperatures of iron and cobalt; iron melts at T = 1809 K, and cobalt melts at T = 1766.9 K, so it seems reasonable that different temperature boundary conditions could apply.

Table 4.8: Coefficients used in Equation (4.4) to calculate the coefficients used in Equation (4.3) for the activity of iron.

$T < 1800$ K

	A_{Fe}	B_{Fe}	C_{Fe}	D_{Fe}	E_{Fe}	F_{Fe}	G_{Fe}
$a_{Fe,(x_{Co})}$	1.110936799E-05	-3.230480060E-05	3.591729215E-05	-1.961802124E-05	5.477855205E-06	-5.874994882E-07	5.659824358E-09
$b_{Fe,(x_{Co})}$	-4.055993621E-02	1.172858891E-01	-1.294622020E-01	6.980738026E-02	-1.898916742E-02	1.936461583E-03	-1.845708168E-05
$c_{Fe,(x_{Co})}$	36.837112635	-106.196649816	116.796542266	-61.918585830	16.035147973	-2.567739966	1.014726126

$T > 1800$ K

	A_{Fe}	B_{Fe}	C_{Fe}	D_{Fe}	E_{Fe}	F_{Fe}	G_{Fe}
$a_{Fe,(x_{Co})}$	3.511293749E-09	-1.401828192E-07	2.755858409E-07	-9.149909081E-08	-4.651595535E-08	-9.148245356E-10	7.259404977E-12
$b_{Fe,(x_{Co})}$	2.334542822E-05	6.717102306E-04	-1.483199637E-03	4.835851272E-04	2.999620906E-04	4.677225709E-06	-3.731282505E-08
$c_{Fe,(x_{Co})}$	-0.154499141	-0.760068554	2.293382413	-0.709589347	-0.663381147	-1.005955679	1.000051614

Table 4.9: Coefficients used in Equation (4.4) to calculate the coefficients used in Equation (4.3) for the activity of cobalt.

$T < 1700$ K

	A_{Co}	B_{Co}	C_{Co}	D_{Co}	E_{Co}	F_{Co}	G_{Co}
$a_{Co,(x_{Co})}$	1.177271997E-05	-3.346830772E-05	3.575905444E-05	-1.870701209E-05	5.256140311E-06	-6.230701630E-07	3.598434338E-09
$b_{Co,(x_{Co})}$	-2.906479502E-02	8.367474117E-02	-9.188779973E-02	5.050775661E-02	-1.508929504E-02	1.891699106E-03	-1.129841307E-05
$c_{Co,(x_{Co})}$	15.305683341	-44.926763566	51.059784137	-29.964657401	10.226207885	-0.724520636	0.008404535

$T > 1700$ K

	A_{Co}	B_{Co}	C_{Co}	D_{Co}	E_{Co}	F_{Co}	G_{Co}
$a_{Co,(x_{Co})}$	-2.139958968E-06	8.093122244E-06	-1.207445056E-05	8.780021537E-06	-3.007373826E-06	3.507376834E-07	-1.892890016E-09
$b_{Co,(x_{Co})}$	8.870237370E-03	-3.352690482E-02	5.024571058E-02	-3.672567768E-02	1.246328443E-02	-1.335405404E-03	7.905219123E-06
$c_{Co,(x_{Co})}$	-9.055330980	34.194411183	-51.901841895	38.354756195	-12.499631836	1.916709415	-0.008201868

The activity calculations using Equations (4.3) and (4.3) predict the activity of cobalt within 3% of that calculated from the free energy analysis across the prescribed temperature range. The equations predict the activity of iron within 2.4% of that calculated from the free energy equations for temperatures between 1500 K and 2300 K, and within 3.5% for temperatures between 1300 K and 1500 K.

With the activity and the temperature-time profiles available, sample evaporation calculations were performed using the Langmuir Equation [110], which Lee and Matson [111] used in order to perform evaporation calculations on $Fe_{50}Co_{50}$ samples:

$$\dot{m}_e = \alpha_e a_e A_s p_{v,e} \sqrt{M_e/2\pi RT} \qquad (4.5)$$

$\dot{m}$ is the mass evaporation rate, α is the evaporation correction factor, which was assumed to be one for both iron and cobalt, a is the activity of the component, A_s is the surface area of the sample, M is the molar mass of the component, R is the universal gas constant, T is the temperature of the sample, and p_v is the vapor pressure of the component. The vapor pressure data was take from Honig [112], and is given by Equation (4.6).

$$log_{10}(p_{v,e}) = 133.322(A_e/T + B_e log_{10}(T) + C_e T + D_e T^2 + E_e) \qquad (4.6)$$

The coefficients that are required to calculate the vapor pressure for iron and cobalt can be found in Table 4.10.

In this case, the surface area is a function of the density of the sample. Lee *et al.* [113] showed that the density of liquid Fe–Co alloys with cobalt concentrations between 30 and 50 at.% deviated less than 0.5% from that of an ideal solution.

Table 4.10: Coefficients used in Equation (4.6) to calculate the vapor pressure for iron and cobalt [112].

Element	A_e	B_e	C_e	D_e	E_e
Fe	-2.4610 E4	-8.32083	6.686 E-4	-3.04822 E-8	38.0026
Co	7.0044 E3	54.1831	-12.0134 E-3	9.31868 E-7	-155.981

Since there is limited information on the density of Fe-Co as a function of temperature and composition, it was assumed that the density varied linearly with composition at a given temperature. For the solid phases, the density of iron and cobalt were taken from Mills [114], and the density of the liquid phases were taken from Iida and Guthrie [115]. During the initial evaporation calculations, it was observed that the fraction of mass evaporation that occurs below 1300 K is less than 50 PPM for the typical temperature-time profiles that are generated during testing, which is why the simplified activity calculations are only provided for temperatures between 1300 K and 2300 K. The activity at any temperature (outside of the specified range) and composition can be calculated from the free energy equation. A summary of the results of the evaporation calculations can be found in Table 4.11. The average chamber pressure for those samples was on the order of 10^{-9} mbar, thus ensuring that the Langmuir equation was applicable at the high temperatures at which the experiments were conducted.

With the exception of 2 samples, all of the calculations predict the total mass evaporation within 15% of measured evaporation. This is reasonable considering the uncertainties associated with estimation of density and vapor pressure.

Table 4.11: Results of the Fe–Co mass evaporation calculations, including the initial composition, x_{Co}, initial sample mass , m_i, final sample mass, m_f, measured mass evaporation, Δm, calculated mass evaporation, Δm_{calc}, and mass evaporation error $10^2(\Delta m_{calc} - \Delta m)/\Delta m$. During testing, the chamber pressure was on the order of 10^{-9} mbar.

Sample	x_{Co}	m_i (mg)	m_f (mg)	Δm (mg)	Δm_{calc} (mg)	$10^2(\Delta m_{calc} - \Delta m)/\Delta m$
1	0.3	43.051	40.457	2.58	3.1085	20.67
2	0.3003	44.999	42.464	2.54	2.5813	1.83
3	0.2993	43.265	41.208	2.06	2.0103	-2.27
4	0.4	39.035	37.862	1.173	1.2417	5.86
5	0.4	41.15	39.981	1.169	1.215	3.97
6	0.5035	50.016	48.138	1.878	1.9927	6.11
7	0.5037	42.185	39.66	2.525	2.7815	10.16
8	0.5027	43.173	42.636	0.537	0.6578	22.5
9	0.5035	39.334	37.01	2.324	2.5161	8.27
10	0.5089	40.839	37.076	3.763	4.296	14.16
11	0.5063	38.774	37.049	1.725	1.9695	14.17
12	0.4983	41.488	39.678	1.81	1.9264	6.43

4.2.4 Metastable Phase Diagram, Thermophysical Properties, and Growth Parameter Prediction

The metastable phase diagram, given in Figure 4.16, shows good agreement with the experimental metastable data from the current work, as well as experimental data from Woodcock [38]. Although the presentation of metastable phase diagram provided by Woodcock [38] does not include compositions where $x_{Co} > 0.6$, it is relatively simple to calculate that portion of the phase diagram using the free energy parameters that were provided in the work.

Reevaluating the delay times in ESL, given in Figure 4.17, including the undercooling that corresponds to the liquidus temperature of the metastable phase, it is clear that there is a correlation between the minimum delay time and the thermal driving potential, $\Delta T_{\gamma\delta}$.

In general, dendritic rapid solidification is a highly non-equilibrium process. As undercooling increases, solidification growth velocity increases, and diffusion decreases. That ultimately leads to complete solute trapping and partitionless
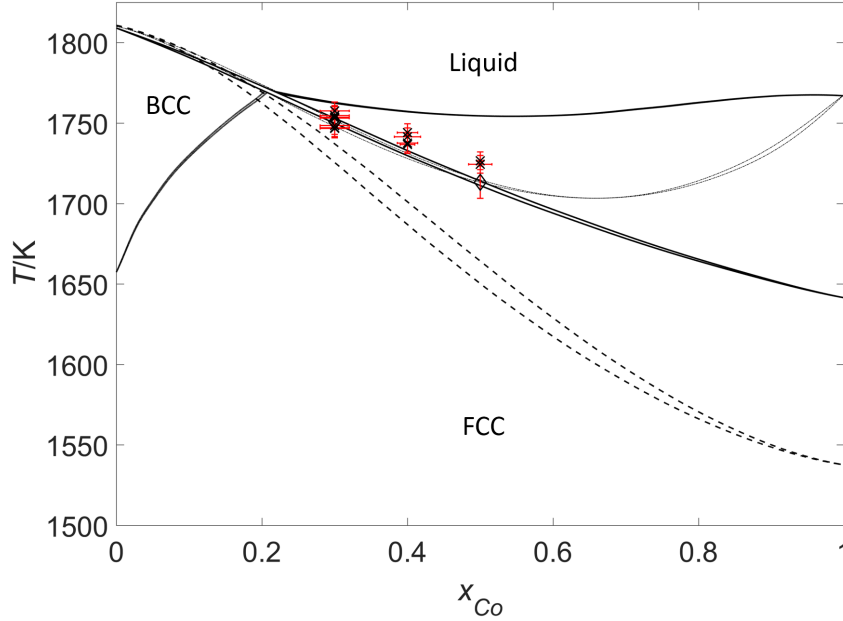
Figure 4.16: Metastable phase diagram comparing the current work and experimental data to the previous analytical results and experimental data: ──── Current; - - - - [35, 37]; ·--·--·- [38]; ✕ observed temperature of the metastable phase from the current work; ◇ observed metastable temperature (EML) [38]. Cobalt composition error bars correspond to the measured evaporation that occurred during the experiments, under the worst-case scenario that all of the mass loss was from one component of the system. Temperature error bars correspond to the accuracy of the pyrometer at the given temperature, ± 0.3% of reading in °F + 1.8 °F.

solidification [116]. However, that only applies only at the dendrite tip, and the spot size of the pyrometer is on the order of the sample radius; the temperature of the dendrite tip is somewhere between the liquidus and solidus temperature. However, the bulk temperature measurement can correspond very nearly to the equilibrium liquidus temperature. Obviously, this depends on the amount of partitioning that the sample exhibits. This effect can be evaluated by plotting the measured temperature of the metastable phase as a function of the initial undercooling. If the temperature of the metastable phase shows significant trend, then the liquidus temperature is accurately represented, within the error of temperature measurement. If there is a noticeable reduction
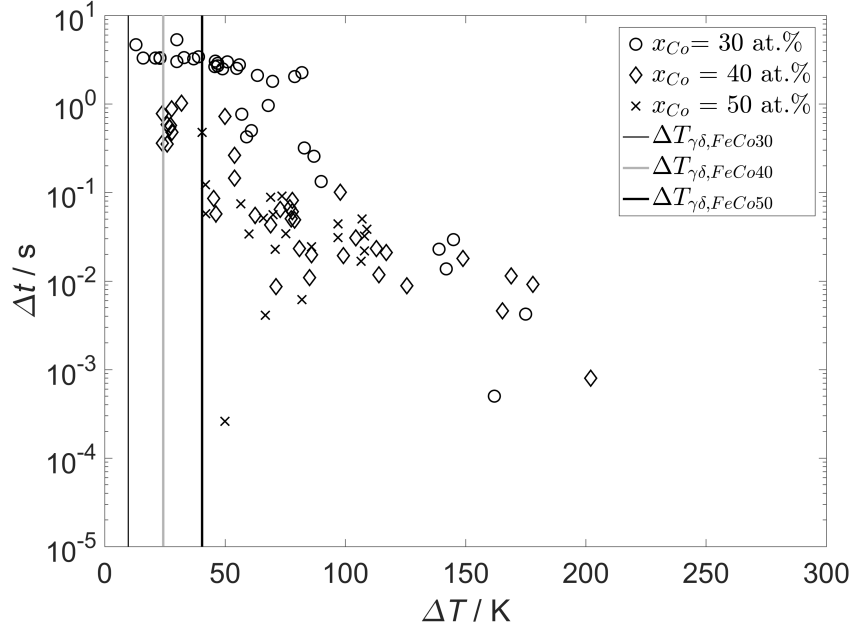
Figure 4.17: Delay time of ESL samples as a function of undercooling.

of the temperature of the metastable phase, then the alloy exhibits significant partitioning.

Figure 4.18 shows the metastable temperature data points for Fe 30 at.% Co. Note that due to the limited partitioning in this system, the temperature of the metastable phase shows no significant dependence on the initial undercooling.

The enthalpy and entropy corresponding to the BCC-Liquid and FCC-Liquid relationships is given as a function of composition in Figures 4.19 and 4.19. The BCC liquidus and solidus lines at compositions greater than 0.217 and 0.204 respectively correspond to the metastable phase. From the metastable phase diagram, it was also possible to determine the partition coefficient for the BCC-Liquid and FCC-Liquid relationships as seen in Figure 4.21, as well as the thermal driving potential for solidification from the metastable phase to the stable phase, given in Figure 4.22, and the FCC and BCC liquidus slopes, m_L, as depicted in Figure 4.23. Those parameters can be applied to a given

66
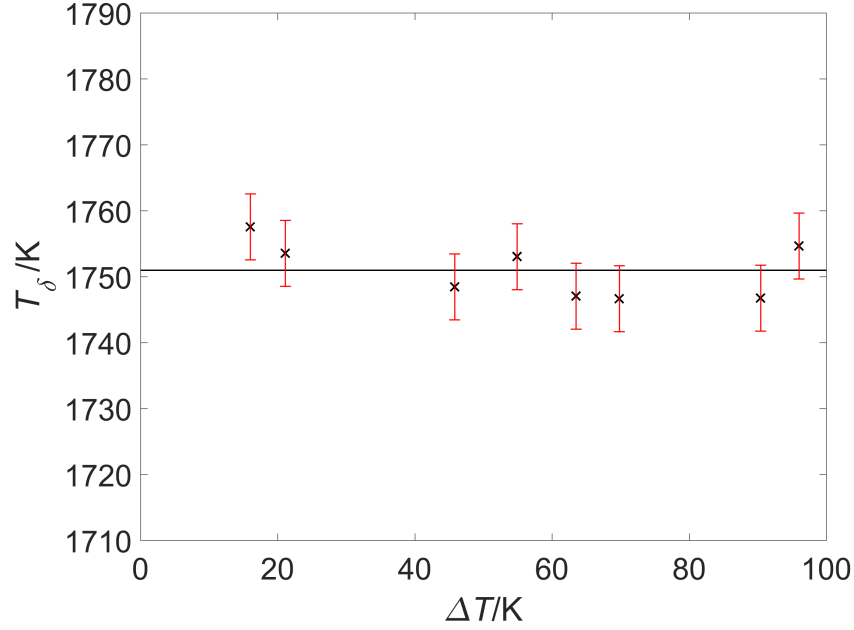
Figure 4.18: Observed Temperature os the metastable phase of Fe 30 at.% Co as a function of total undercooling. ——— Average measured temperature of the metastable phase, $\bar{T}_\delta$ = 1751 K. Temperature error bars correspond to the accuracy of the pyrometer at the given temperature, ± 0.3% of reading in °F + 1.8 °F.

dendrite growth model to predict dendrite growth velocity.

The partition coefficient can be calculated using a 6th order equation, as seen in Equation (4.7). Table 4.12 contains the coefficients that are used in Equation (4.7), to calculate the FCC-Liquid and BCC-Liquid partition coefficients.

$$k_{e,i} = A_i x_{Co}^6 + B_i x_{Co}^5 + C_i x_{Co}^4 + D_i x_{Co}^3 + E_i x_{Co}^2 + F_i x_{Co} + G_i \qquad (4.7)$$

The subscript i refers to the phase of interest.

Table 4.12: Coefficients used to calculate the partition coefficient of the FCC-Liquid and BCC-Liquid phases.

Phase	A_i	B_i	C_i	D_i	E_i	F_i	G_i
BCC-Liquid	-0.2322	0.5534	-0.2527	-0.2805	0.2407	0.0504	0.9209
FCC-Liquid	1.2435	-3.4215	3.3726	-1.2753	-0.1608	0.3358	0.9057
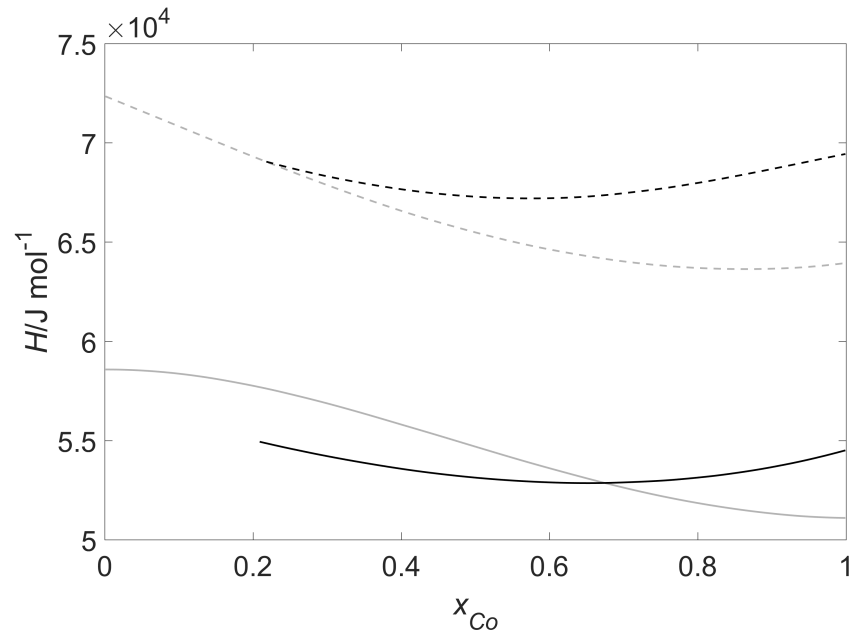
Figure 4.19: Enthalpy of Fe–Co as a function of composition at the BCC and FCC liquidus and solidus temperatures: —— FCC Solidus; —— BCC Solidus; - - - - FCC Liquidus; - - - - BCC Liquidus;
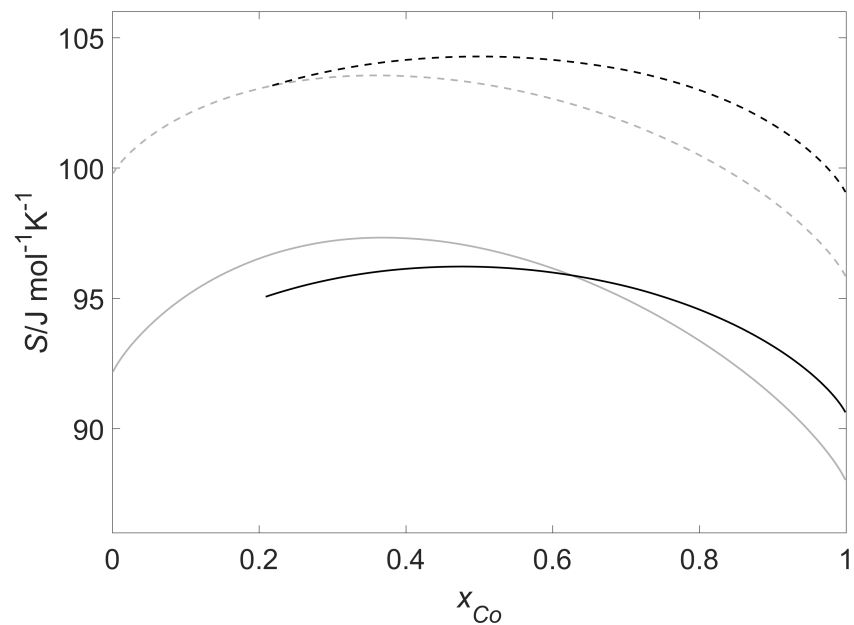
Figure 4.20: Entropy of Fe–Co as a function of composition at the BCC and FCC liquidus and solidus temperatures: —— FCC Solidus; —— BCC Solidus; - - - - FCC Liquidus; - - - - BCC Liquidus;
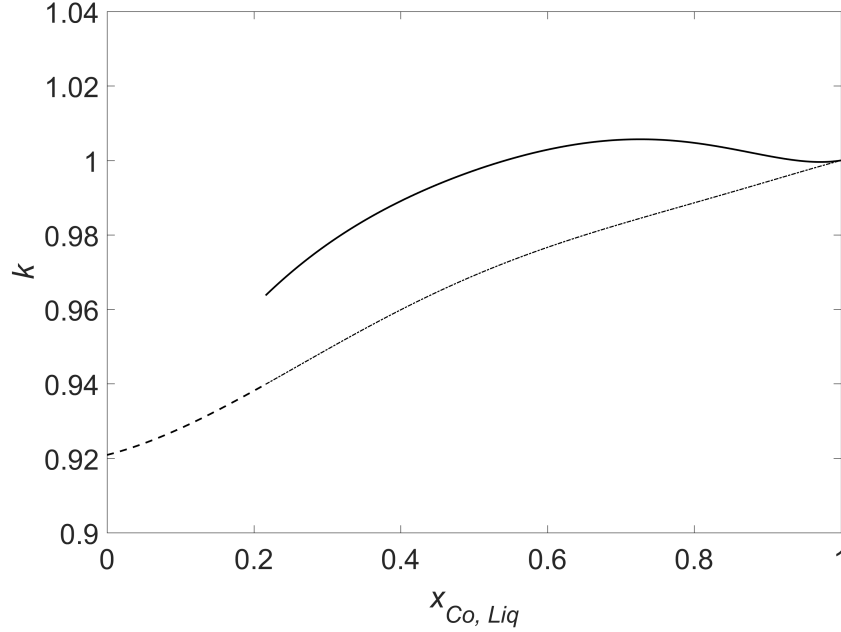
Figure 4.21: Partitioning coefficient for the metastable and stable BCC-Liquid relationship, and the FCC-Liquid relationship, as a function of the liquidus cobalt composition; ——— Stable FCC-Liquid; ‒ ‒ ‒ ‒ Stable BCC-Liquid; ·····- Metastable BCC-Liquid;

For $x_{Co} > 0.217$, the calculated peritectic liquidus composition, the thermal driving potential for the second recalescence can be calculated as a function of liquidus composition $x_{Co,Liq}$ using Equation (4.8):

$$\Delta T_{\gamma\delta} = -374.4x_{Co}^5 + 816.1258x_{Co}^4 - 729.4136x_{Co}^3 + 427.973x_{Co}^2 - 0.4163x_{Co} - 14.4529 \tag{4.8}$$

The liquidus slopes for BCC and FCC phases, as a function of liquidus composition, can be found using Equation (4.9).

$$m_{L,i} = A_i x_{Co}^6 + B_i x_{Co}^5 + C_i x_{Co}^4 + D_i x_{Co}^3 + E_i x_{Co}^2 + F_i x_{Co} + G_i \tag{4.9}$$

The subscript i refers to the phase of interest. The coefficients used to calculate the BCC and FCC liquidus slopes are given in Table 4.13.
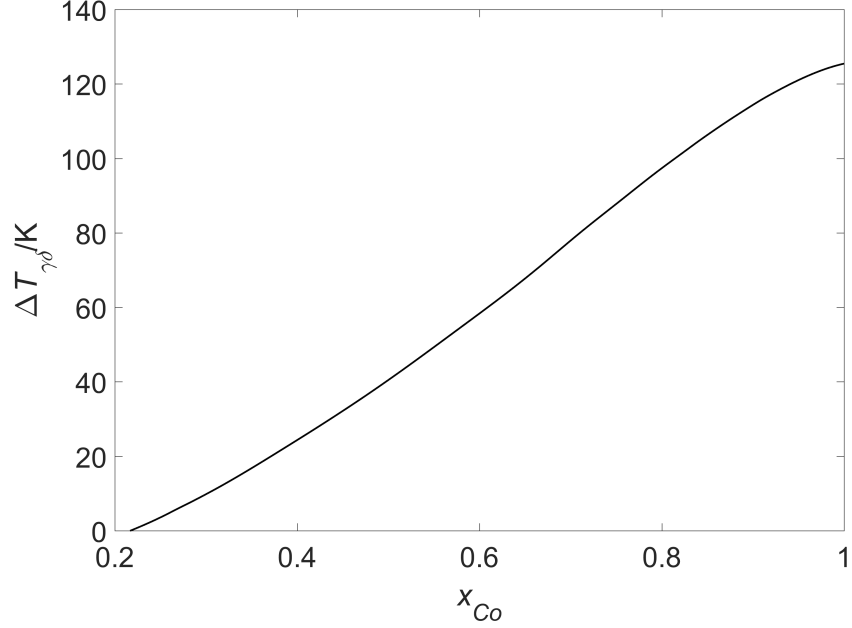
Figure 4.22: Thermal driving potential of the second recalescence as a function of composition; the metastable phase to the stable phase.

Table 4.13: Coefficients used to calculate the BCC and FCC Liquidus slopes using Equation (4.9).

Phase	A_i	B_i	C_i	D_i	E_i	F_i	G_i
BCC Liquidus	12444.0079	-43811.748	62746.4491	-46923.563	19481.556	-4177.3122	152.8582
FCC Liquidus	-466.0077	6719.4738	-18878.121	21060.4831	-11067.4006	3013.6794	-408.8296

4.3 Conclusions

Fe–Co samples, which were processed via ESL, exhibited double recalescence solidification when sufficient undercooling was achieved. By adjusting various parameters in the Gibbs energy analysis, a new and consistent phase diagram was generated. The equilibrium phase diagram, given in figures 4.6 and 4.7, shows excellent agreement with new and previous experimental data. Various thermophysical property calculations, including heat capacity, enthalpy, enthalpy of formation, and activity, show good agreement with experimental data, thus supporting the validity of the modified parameters. The evaporation analysis also agrees well with the experimental results considering the uncertainties
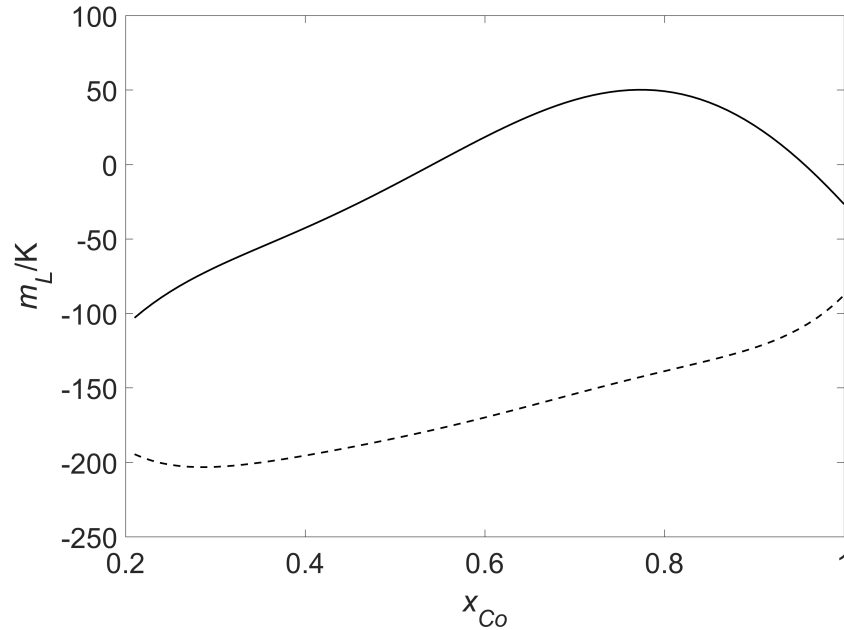
Figure 4.23: 6th order polynomial representation of the BCC and FCC liquidus slopes: ———— FCC Liquidus; - - - - BCC Liquidus

associated with the vapor pressure and densities of both iron and cobalt.

The metastable phase diagram, given in Figure 4.16, reasonably represents the location of the metastable phase, and the equilibrium solidification model was found to accurately predict the observed temperatures of the metastable phase.

From the metastable phase diagram, equations for the BCC-Liquid and FCC–Liquid partitioning coefficients, as well as the transformation driving potential for the second recalescence and the BCC and FCC liquidus slopes were found. Used in conjunction with the thermophysical property estimates, these functions can be used to predict dendrite growth velocities and transformation kinetics for this commercially important binary system.

This is the first successful demonstration of the applicability of metastable temperature data for improving an equilibrium phase diagram, and generating an accurate metastable phase diagram.

Chapter 5

Growth Kinetics: Solid-Liquid Interactions

In this chapter, new experimental results of growth velocity in both electrostatically and electromagnetically levitated samples will be presented. While electromagnetic levitation processing leads to stirring in the melt, the electrostatic levitation technique provides containerless solidification experiments without significant induced convection [25]. In the current work, rapid solidification was monitored by high-speed video camera. Imaging of double recalescence enabled measurement of the velocity of the stable phase through the mushy zone of the primarily solidified metastable phase, as well as growth of the solid phases through undercooled liquid.

The measured velocities as a function of undercooling for both of the stable γ–phase and metastable δ–phase growing through undercooled are assessed using Lipton-Kurz-Trivedi (LKT) theory [72], including the kinetic undercooling component from Boettinger-Coriell-Trivedi (BCT) theory [89].

The purpose of the growth velocity analysis is two-fold: 1) Assess the validity

of the theory as it applies to the Fe–Co system. 2) Evaluate the kinetic growth coefficient, μ, assuming a constant kinetic rate parameter, V_o. This work sets the foundation for the work in Chapter 6.

5.1 Analysis

The experimental solidification velocity determined by using a high-speed camera technique developed by Matson [117]. The growth of the solid phases through undercooled liquid was assessed using LKT theory [72], incorporating the marginal stability criterion from Trivedi and Kurz [71], and including kinetic effects from BCT theory [89], and non-equilibrium effects discussed in Section 2.3.3. The complete analysis is described in Sections 2.3.1-2.3.3.

There were no observed effects of melt convection on primary growth kinetics, therefore, external flow considerations were neglected within the stability parameter σ^*. In general, the application of the marginal stability criterion within the perturbation analysis predicts experimental results well, and reduces the number of unknowns and adjustable parameters within the analysis. For these reasons, σ^* was chosen to be equal to $1/4\pi^2$ within the current work. Tables 5.1 and 5.2 show the thermophysical property values that were used in the analysis. Images of the $Fe_{70}Cr_xNi_{30-x}$ wt.% and $Fe_{72}Cr_xNi_{28-x}$ wt.% pseudobinary phase diagrams are given in Appendix B.

Table 5.1: Thermophysical property values used in the Fe–Co solidification analysis.

Properties	$Fe_{70}Co_{30}$	$Fe_{60}Co_{40}$	$Fe_{50}Co_{50}$
$^{\star}a_o$ (m)	2.358E-10 [115]	2.354E-10 [115]	2.35E-10 [115]
$^{\star}\alpha$ (m^2/s)	5.46E-06 [118]	5.36E-06 [118]	5.29E-06 [118]
C_o (at.%)	30	40	50
$C_P^{L,\gamma} \mid C_P^{L,\delta}$ (J/m^3-K)	5749190 | 5712909 [4]	5796451 | 5704510 [4]	5822432 | 5666976 [4]
D_o (m^2/s)	4.7E-9 [119]	4.7E-9 [119]	4.7E-9 [119]
$\Delta H_\gamma \mid \Delta H_\delta$ (J/mol)	14098 | 10999 [4]	14083 | 10767 [4]	14154 | 10795 [4]
$k_e^\gamma \mid k_e^\delta$	0.977 | 0.949 [4]	0.989 | 0.96 [4]	0.997 | 0.969 [4]
$m_L^\gamma \mid m_L^\delta$ (K/at.%)	-0.69 | -1.99 [4]	-0.45 | -1.98 [4]	-0.13 | -1.85 [4]
$T_\gamma \mid T_\delta$ (K)	1763 | 1753 [4]	1757 | 1733 [4]	1754 | 1714 [4]
$\Delta T_{\gamma\delta}$ (K)	10 [4]	24 [4]	40 [4]
$^{\star\star}\sigma_\gamma \mid \sigma_\delta$ (J/m^2)	0.319 | 0.206 [120]	0.319 | 0.206 [120]	0.319 | 0.206 [120]
$^{\star}\rho_S \mid \rho_L$ (kg/m^3)	7612 [114, 121] | 7242 [113]	7718 [114, 121] | 7352.53 [113]	7824 [114, 121] | 7423.47 [113]
$\Delta S_\gamma \mid \Delta S_\delta$ (J/m^3-K)	1020485 | 801219 [4]	1032396 | 801030 [4]	1043547 | 815419 [4]
$V_o^\gamma \mid V_o^\delta$ (m/s)	550 | 350	550 | 350	550 | 350
$^{\star}V_S \mid V_d$ (m/s)	4307 [115] | 19.9	4276 [115] | 20	4245 [115] | 20
$^{\star}\Omega_S \mid \Omega_L$ (m^3/mol)	7.4577 E-6 | 7.8384 E-6	7.3953 E-6 | 7.76335 E-6	7.3346 E-6 | 7.73076 E-6
X_o (at. Fraction)	0.3	0.4	0.5

* Indicates that ideal mixing was assumed and that the values were obtained based on the atomic composition of the alloy.
** Values for pure iron were used.

Table 5.2: Thermophysical property values used in the Fe–Cr–Ni solidification analysis.

Properties	$Fe_{70}Cr_{15}Ni_{15}$	$Fe_{72}Cr_{12}Ni_{16}$
$^{\star\star}a_o$ (m)	2.37E-10 [115]	2.37E-10 [115]
$^{\star}\alpha$ (m^2/s)	6.01E-06 [118]	5.98E-06 [118]
C_o (at.%)	16.05	12.87
C_P^L (J/m^3-K)	5541049	5564890
D_o (m^2/s)	2.58E-9 [8]	2.64E-9 [8]
$\Delta H_\gamma \mid \Delta H_\delta$ (J/mol)	11723 | 10549 [122]^a	12153 | 11009 [122]^a
$k_e^\gamma \mid k_e^\delta$	0.889 | 0.751 [122]^a	0.902 | 0.746 [122]^a
$m_L^\gamma \mid m_L^\delta$ (K/at.%)	-2.11 | -6.59	-1.33 | -6.03
$T_\gamma \mid T_\delta$ (K)	1735 [122]^a | 1718 [8, 122]	1743 | 1704 [122]^a
$\Delta T_{\gamma\delta}$ (K)	17 [8]	39 [122]^a
$^{\star\star}\sigma_\gamma \mid \sigma_\delta$ (J/m^2)	0.319 | 0.206 [120]	0.319 | 0.206 [120]
$\Delta S_\gamma \mid \Delta S_\delta$ (J/m^3-K)	854244 | 789735 [122]^a	881788 | 829086 [122]^a
$V_o^\gamma \mid V_o^\delta$ (m/s)	750 | 325	750 | 325
$^{\star\star}V_S \mid V_d$ (m/s)	4400 [115] | 10.9	4400 [115] | 11.1
$^{\star}\Omega_S \mid \Omega_L$ (m^3/mol)	7.5071E-6 | 7.725E-6 [122]^a	7.4989E-6 | 7.9172E-6 [122]^a
X_o (at. Fraction)	0.1605	0.1287

* Indicates that ideal mixing was assumed and that the values were obtained based on the atomic composition of the alloy.
** Values for pure iron were used.
^{a} Values were obtained from Thermo-Calc Software, Version 8 (2015b), FEDEMO database (a subset of the TCFE8 database).

5.2 Results and Discussion

Table 5.3: Values of $\bar{V}_{\gamma\delta}$ and μ for each Fe–Co alloy. The ± error margins were calculated at a 95% confidence level.

Properties	$Fe_{70}Co_{30}$	$Fe_{60}Co_{40}$	$Fe_{50}Co_{50}$
$\mu_{\gamma L}\mid\mu_{\delta L}$ (m/s-K)	0.300 $\mid$ 0.151	0.302 $\mid$ 0.151	0.304 $\mid$ 0.155
$\bar{V}_{\gamma\delta}$ (m/s)	1.6 ± 0.45 *	2.4 ± 0.23	4.9 ± 0.27
Standard Deviation (m/s)	0.76	0.64	1.42
Num. $V_{\gamma\delta}$ Data Points	11	29	104

* Indicates that the values are based on few data points.

Table 5.4: Values of $\bar{V}_{\gamma\delta}$ and μ for each Fe–Cr–Ni alloy. The ± error margins were calculated at a 95% confidence level.

Properties	$Fe_{70}Cr_{15}Ni_{15}$	$Fe_{72}Cr_{12}Ni_{16}$
$\mu_{\gamma L}\mid\mu_{\delta L}$ (m/s-K)	0.351 $\mid$ 0.14	0.361 $\mid$ 0.148
$\bar{V}_{\gamma\delta}$ (m/s)	1.6 ± 0.39 * [11]	3.9 ± 0.31 [12]
Standard Deviation (m/s)	0.40	0.81
Num. $V_{\gamma\delta}$ Data Points	4	26

* Indicates that the values are based on few data points.

Tables 5.3 and 5.4 show the average growth velocity of the stable phase through the mushy zone, $\bar{V}_{\gamma\delta}$, as well as the kinetic coefficient, μ, which was used in the dendrite growth analyses. The error margins given for $\bar{V}_{\gamma\delta}$ were calculated at a 95% confidence level.

From Equation (2.44), μ is seen to vary with $\Delta H_f/T_m^2$. Therefore, as the alloy composition shifts μ should shift in accordance with the change in $\Delta H_f/T_m^2$ for a given solid phase. In this case, that value changes very little, which is why μ is similar for the three Fe–Co alloys, and the two Fe–Cr–Ni alloy compositions.

The experimental results and the results of the theoretical analyses are given in Figures 5.1-5.5. Figures 5.1-5.3 show the experimental growth velocity results from the current work, as well as those from Dolan [123] and Hermann *et al.* [7]. Figures 5.4 and 5.5 show $FeCr_{15}Ni_{15}$ wt.% and $FeCr_{12}Ni_{16}$ wt.% experimental growth velocity results from Matson *et al.* [11, 12], compared to the theoretical

results from this work.

In some cases, after the metastable phase nucleated, the stable phase would nucleate within the mushy zone formed during primary solidification and grow fast enough to outgrow the metastable phase and escape into the undercooled liquid. In those cases, it was possible to estimate the solid-liquid growth velocity for both solid phases as well as the velocity of the stable phase growing into the mushy zone. The results are displayed as a function of the undercooling relative to the melting point of the stable phase. For example, for the Fe–40 at.% Co alloy, the thermal driving force is calculated from the difference between the melting points:

$$\Delta T_{\gamma\delta} = T_\gamma - T_\delta = 1757 - 1733 = 24K. \tag{5.1}$$

For an undercooling of 100 K relative to the stable phase, the undercooling relative to the metastable phase is 76 K. There are no growth velocity measurements of either the metastable phase into liquid, or the stable phase into the mushy zone if the underooling is less than 24 K, as there can be no double recalescence. In Figure 5.4, there is one $V_{\delta L}$ data point to the left of the $\Delta T_{\gamma\delta}$ line; this is likely due to uncertainty of the magnitude of the thermal driving potential, $\Delta T_{\gamma\delta}$, or some small pyrometer temperature measurement error.

The δ and γ phase kinetic rate parameters were taken to be $V_{o,\delta} = 350$ m/s-K and $V_{o,\gamma} = 550$ m/s-K for the Fe–Co alloys, and $V_{o,\delta} = 325$ m/s-K and $V_{o,\gamma} = 750$ m/s-K for the Fe–Cr–Ni alloys. For a constant value of V_o for each phase of each alloy, the results of the dendrite growth analyses match sufficiently well with the experimental data. This indicates that it is reasonable to assume that V_o is constant for a given phase within an alloy system if $\Delta H_f/T_m^2$ does

Figure 5.1: Growth velocity of Fe–30 at.% Co as a function of undercooling, including experimental results from ESL testing as well as the results of the LKT/BCT [72, 89] analysis. ■ $V_{\delta L}$ (ESL); ♦ $V_{\delta L}$ (EML) [7]; □ $V_{\gamma L}$ (ESL); ◇ $V_{\gamma L}$ (EML) [7]; ■ $V_{\gamma \delta}$ (ESL); ——— $V_{\delta L}$, μ = 0.151; - - - - $V_{\gamma L}$, μ = 0.300; ---------- $\bar{V}_{\gamma \delta}$ = 1.6 m/s; -·-·-·- $\Delta T_{\gamma \delta}$ = 10 K. $\bar{V}_{\gamma \delta}$ is the averaged value of the available experimental data points of $V_{\gamma \delta}$.

not vary significantly within the system, or within the composition range of interest.

The velocity of the solid phases growing into undercooled liquid, as well as the stable phase growing into the mushy zone, were found to be independent of melt convection. This is because the growth velocity is much greater than the melt convection velocity, particularly at higher undercoolings [24]. In the case of the γ–phase growing through the mushy zone, it is unlikely that there will be significant stirring due to the presence of the dendritic structure of the metastable solid.

The mushy zone velocity is greater than that of the stable phase growing through undercooled liquid at the critical undercooling, $\Delta T_{\gamma \delta}$, and it is independent of the initial undercooling, but varies with cobalt concentration. The γ–phase

Figure 5.2: Growth velocity of Fe–40 at.% Co as a function of undercooling, including experimental results from ESL and EML testing as well as the results of the LKT/BCT [72,89] analysis. ■ $V_{\delta L}$ (ESL); ● $V_{\delta L}$ (ESL) [123]; ▼ $V_{\delta L}$ (EML); ◆ $V_{\delta L}$ (EML) [7]; ★ $V_{\delta L}$ (Parabolic Flight) [7]; □ $V_{\gamma L}$ (ESL); ▽ $V_{\gamma L}$ (EML); ◇ $V_{\gamma L}$ (EML) [7]; ✩ $V_{\gamma L}$ (Parabolic Flight) [7]; ▦ $V_{\gamma \delta}$ (ESL); ⬤ $V_{\gamma \delta}$ (ESL) [123]; ▼ $V_{\gamma \delta}$ (EML); ——— $V_{\delta L}$, $\mu = 0.151$; - - - - $V_{\gamma L}$, $\mu = 0.302$; ---------- $\bar{V}_{\gamma \delta} = 2.4$ m/s; -·-·-·-·- $\Delta T_{\gamma \delta} = 24$ K. $\bar{V}_{\gamma \delta}$ is the averaged value of the available experimental data points of $V_{\gamma \delta}$. EML growth velocity results in the current work are from collaboration with Thomas Volkmann and Carolina Kreischer at the German Aerospace Center (DLR)[1].

mushy-zone growth velocity becomes larger as the cobalt concentration is increases because the difference between melting temperatures of the δ–phase and γ–phase increases. Matson and Hyers [100] previously addressed this observation within an adiabatic remelt model. In the remelt model, some portion of the pre-existing metastable phase is remelted, absorbing the heat of fusion. This remelting is accounted for with an effective heat capacity of the growth environment which is greater than the heat capacity of the liquid by itself. Given that the effective heat capacity is greater than the liquid heat capacity, and that the thermal driving potential is constant for a given alloy composition, it is logical that the growth velocity of the stable phase through
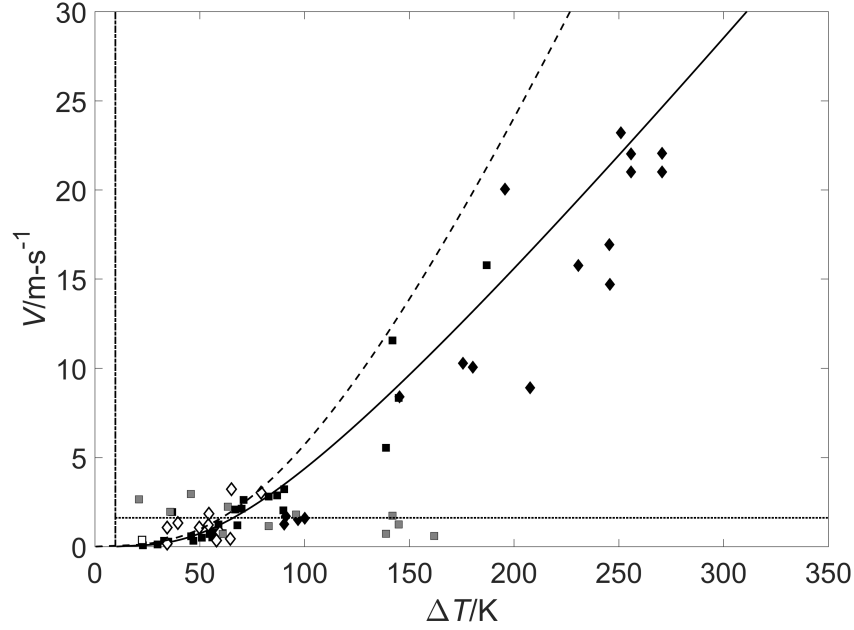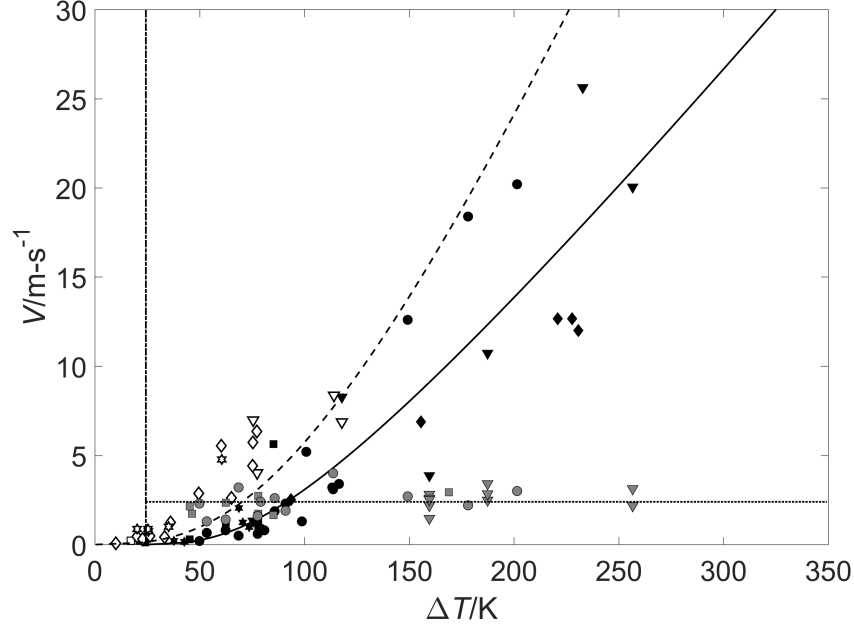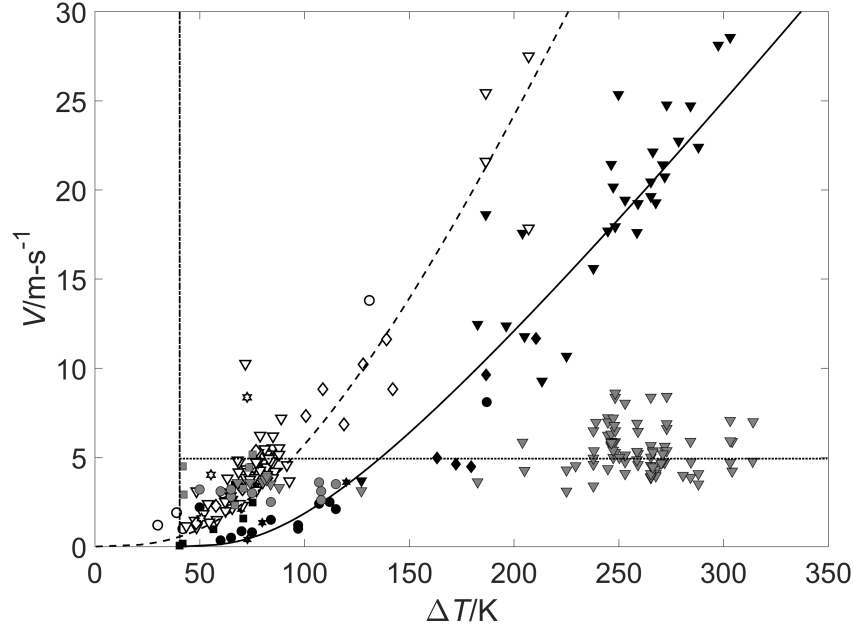
Figure 5.3: Growth velocity of Fe–50 at.% Co as a function of undercooling, including experimental results from ESL and EML testing as well as the results of the LKT/BCT [72, 89] analysis. ■ $V_{\delta L}$ (ESL); ● $V_{\delta L}$ (ESL) [123]; ▼ $V_{\delta L}$ (EML); ◆ $V_{\delta L}$ (EML) [7]; ★ $V_{\delta L}$ (Parabolic Flight) [7]; □ $V_{\gamma L}$ (ESL); ▽ $V_{\gamma L}$ (EML); ◇ $V_{\gamma L}$ (EML) [7]; ✩ $V_{\gamma L}$ (Parabolic Flight) [7]; ▨ $V_{\gamma \delta}$ (ESL); ● $V_{\gamma \delta}$ (ESL) [123]; ▼ $V_{\gamma \delta}$ (EML); —— $V_{\delta L}$, $\mu = 0.155$; - - - - $V_{\gamma L}$, $\mu = 0.304$; ---------- $\bar{V}_{\gamma \delta} = 4.9$ m/s; -·-·-·-·- $\Delta T_{\gamma \delta} = 40$ K. $\bar{V}_{\gamma \delta}$ is the averaged value of the available experimental data points of $V_{\gamma \delta}$. EML growth velocity results in the current work are from collaboration with Thomas Volkmann and Carolina Kreischer at the German Aerospace Center (DLR)[1] [105].

the mushy zone will be constant, and greater than that of the solid phase growing through liquid at the same undercooling, $\Delta T_{\gamma \delta}$.

The Fe–Co results show no significant effects of a transition from diffusion-limited growth to the kinetically limited regime, which have previously been observed in other systems [124–126]. This behavior is expected because both the δ–phase and γ–phase exhibit very little partitioning and both have relatively shallow liquidus slopes. The Fe–Cr–Ni results show minor effects of the thermo-

---

[1]Institut für Materialphysik im Weltraum,
Deutsches Zentrum für Luft- und Raumfahrt (DLR),
Linder Höhe, 51147 Cologne, Germany
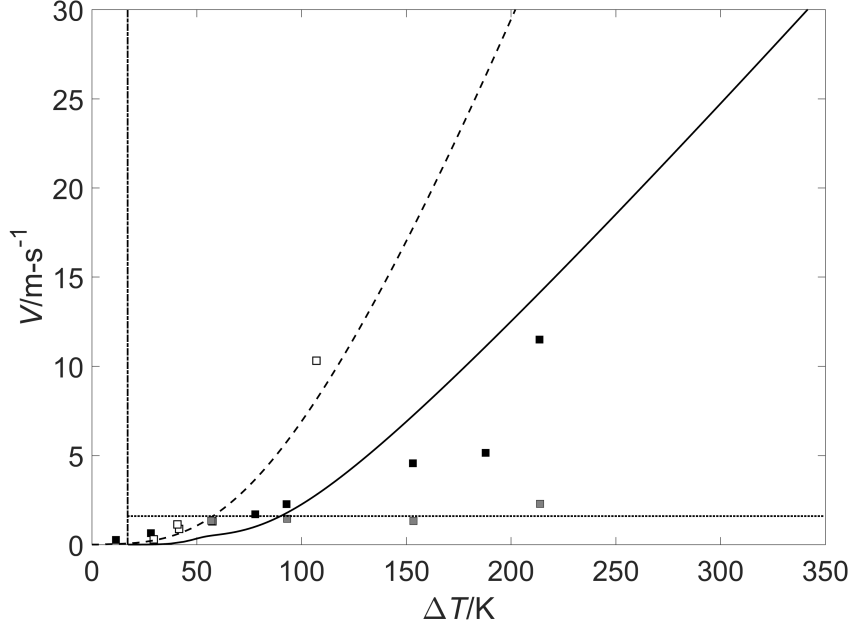
Figure 5.4: Results of the LKT/BCT [72, 89] growth velocity analysis on FeCr$_{15}$Ni$_{15}$ wt.%, compared to experimental results from Matson *et al.* [11]. ■ $V_{\delta L}$ (EML) [11]; □ $V_{\gamma L}$ (EML) [11]; ▥ $V_{\gamma\delta}$ (EML) [11]; —— $V_{\delta L}$, $\mu = 0.141$; - - - - $V_{\gamma L}$, $\mu = 0.351$; ---------- $\bar{V}_{\gamma\delta} = 1.6$ m/s; -·-·-·- $\Delta T_{\gamma\delta} = 17$ K [8]. $\bar{V}_{\gamma\delta}$ is the averaged value of the available experimental data points of $V_{\gamma\delta}$.

solutal[2] transition, particularly in the case of the metastable δ–phase, due to the lower partition coefficient and high liquidus slope.

From the measured Fe–Co velocities, it is clear that the growth of stable γ—phase into the undercooled liquid is faster than that of the metastable δ–phase at a given undercooling. This is, in part, due to the fact that the undercooling relative to the metastable phase represents only a fraction of the total undercooling. The undercooled melt solidifies primarily into the metastable phase although its growth rate is smaller than that of the stable counterpart. Thus, growth of competing phases can be excluded as the mechanism for phase selection. Primary solidification of the metastable δ-–phase phase must therefore be determined by preferred nucleation.

---

[2]The thermo-solutal growth region is defined as the transition region between diffusion limited and kinetically limited growth.
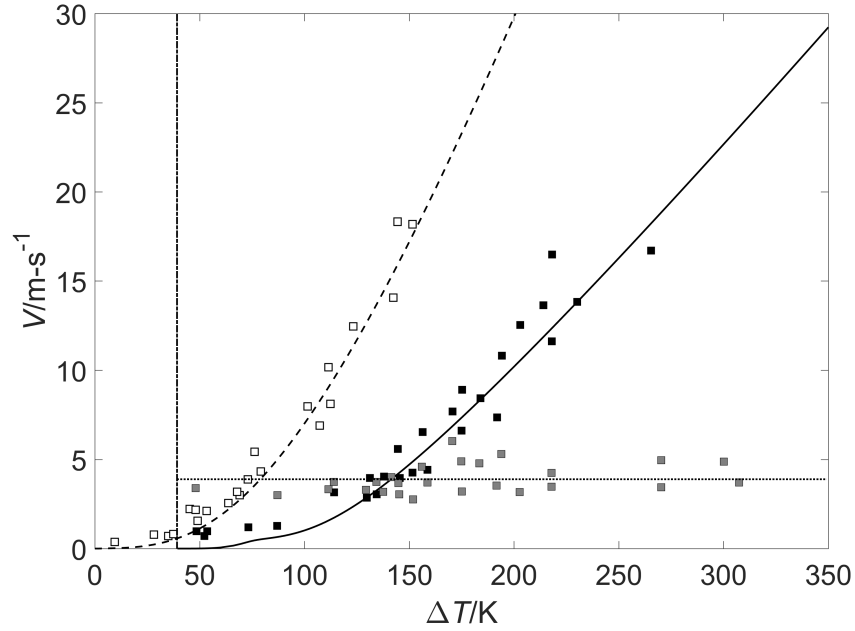
Figure 5.5: Results of the LKT/BCT [72, 89] growth velocity analysis on FeCr$_{12}$Ni$_{16}$ wt.%, compared to experimental results from Matson [12]. ■ $V_{\delta L}$ (EML) [12]; □ $V_{\gamma L}$ (EML) [12]; ■ $V_{\gamma\delta}$ (EML) [12]; —— $V_{\delta L}$, μ = 0.148; ---- $V_{\gamma L}$, μ = 0.361; ---------- $\bar{V}_{\gamma\delta}$ = 3.9 m/s; -·-·-·-· $\Delta T_{\gamma\delta}$ = 39 K [122]. $\bar{V}_{\gamma\delta}$ is the averaged value of the available experimental data points of $V_{\gamma\delta}$. The value of $\Delta T_{\gamma\delta}$ was obtained from Thermo-Calc Software, Version 8 (2015b), FEDEMO database (a subset of the TCFE8 database).

5.3 Conclusions

New experimental results of the growth velocity of the stable phase into the mushy zone have been presented for various Fe–Co alloys. Based on the experimental results, there are several key takeaways: 1) The velocity of the stable phase growing into the mushy zone is greater than that of the stable phase growing into undercooled liquid at the critical undercooling. 2) The growth velocities of the solid phases growing through undercooled liquid are unaffected by liquid flow velocity. 3) There are no significant observable effects of the transition from solutal growth to kinetically limited growth.

The results of the dendrite growth analysis indicate that it is reasonable to assume that V_o is constant for a given phase within an alloy system if $\Delta H_f/T_m^2$ does not vary significantly within the system, or within the composition range of interest. It is unclear whether this assumption will hold up in the event that $\Delta H_f/T_m^2$ varies significantly with changes in alloy composition, however, that is only likely to be the case when the alloy contains very dissimilar components in moderate quantities. This is a particularly useful finding which will allow researchers to estimate growth conditions in new alloys by extrapolating from previously known data.

Chapter 6

Growth Kinetics: Growth Through the Mushy Zone

This chapter includes a discussion of a new method of evaluating solidification interactions when a solid phase grows into a pre-existing solid phase in a non-symbiotic manner. The goal was to develop a model that sufficiently described growth of the stable phase into the mushy zone, without requiring in-depth knowledge of the geometry of the growing dendrite or the growth environment.

Matson and Hyers [100] previously addressed the growth of the stable phase into the mushy zone within an adiabatic remelt (AR) model. The model considers that there is some heat flux into the preexisting metastable phase, and that the heat extraction by remelting the metastable solid enhances dendrite growth rates, however, the model is dependent on knowing the thickness of secondary stable phase.

From the results given in Chapter 5, the velocity of the stable phase growing through the mushy zone was found to be greater than that of the stable

phase growing through undercooled liquid, and the velocity was found to be constant, regardless of the initial undercooling. This is explained, in part, by an effective change in the heat capacity of the growth environment. This effective heat capacity, C_P^{Eff}, considers remelting of the of the metastable phase, in which case the pre-existing δ–phase acts as a heat sink for the stable phase to release energy during solidification. The second consideration is the possibility that heat is conducted from the tip, away from the primary growth direction. These two considerations were applied within the framework an existing dendrite growth model, Lipton-Kurz-Trivedi (LKT) theory [72], including the kinetic undercooling component from Boettinger-Coriell-Trivedi (BCT) theory [89].

6.1   Analysis

The measured mushy-zone velocity was assessed using a modified Lipton-Kurz-Trivedi (LKT) theory [72], incorporating the marginal stability criterion from Trivedi and Kurz [71], and including kinetic effects from BCT theory [89], and non-equilibrium effects discussed in Section 2.3.3.

When dendrites of the stable phase grow through the mushy zone, the they grow at a faster rate than they would through liquid. This could be explained, in part, by an effective change in the heat capacity of the growth environment. Figure 6.1 shows a graphical representation of a stable phase dendrite growing into the mushy zone. Region 1 represents the pre-existing liquid, and region 2 is the pre-existing solid, which is partially melted.
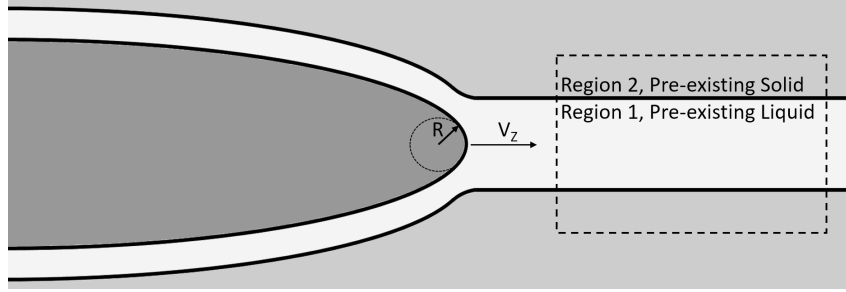
Figure 6.1: Graphical representation of a stable phase dendrite growing into the mushy zone.

6.1.1   The Effective Heat Capacity

In the following energy balance, exothermic reactions will be taken as negative, and endothermic reactions will be taken as positive. If there is no heat flux back down the length of the dendrite, then in region 1, the growing dendrite will release energy equivalent to the heat of fusion, and the pre-existing liquid will absorb as much energy as can be allowed by the liquid's heat capacity and the temperature difference between the existing liquid and the growing dendrite.

$$Q_1 = \left(-\Delta H_{f,S} + C_P^L \Delta T_{SM}\right) V_1 \tag{6.1}$$

$\Delta H_{f,S}$ is the heat of fusion of the stable phase, C_P^L is the liquid heat capacity, ΔT_{SM}[1]is the difference in the liquidus temperatures of the stable and metastable phases, and V_1 is the corresponding volume in region 1 where the reaction occurs. Figure 6.1 shows that the stable phase dendrite grows alongside the existing metastable phase. If the metastable phase acts as a sort of quench medium, then the heat released from the dendrite tip in the primary growth direction will be reduced by the quantity J_S/V. A graphical representation of a dendrite growing through the mushy zone, with a heat flux from the tip

present, is given in Figure 6.2.
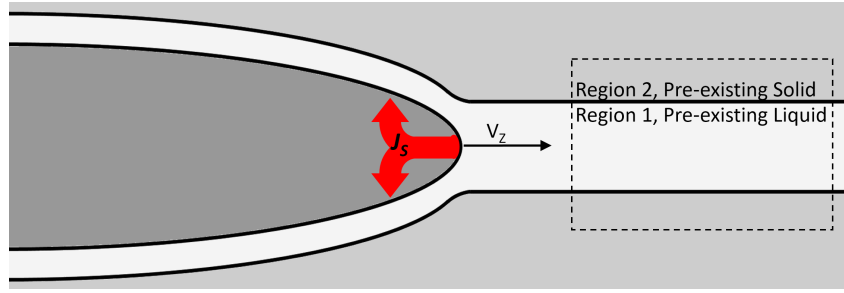
Figure 6.2: Graphical representation of a stable phase dendrite growing into the mushy zone, where there is some heat flux, J_S, away from the primary growth direction.

J_S is the heat flux conducted from the dendrite tip back down its length, and V is the growth velocity. The effective heat flux is mathematically comparable to what Koseki [8] used while evaluating dendrite growth during chill casting. The net energy into region 1 for this case is given in Equation (6.2).

$$Q_1 = \left(-\left(\Delta H_{f,S} - J_S/V\right) + C_P^L \Delta T_{SM}\right) V_1 \tag{6.2}$$

Region 2 will absorb the remaining heat. The solid will melt and then the liquid will be heated. The net energy into region 2 is shown in Equation (6.3).

$$Q_2 = \left(\Delta H_{f,M} + C_P^L \Delta T_{SM}\right) V_2 \tag{6.3}$$

$\Delta H_{f,M}$ is the heat of fusion of the metastable phase, and V_2 is the corresponding volume in region 2 where the reaction occurs.

Absent other long-range heat transfer, conservation of energy requires that the sum of Equations (6.2) and (6.3) is equal to zero, as shown in Equation (6.4).

---

[1]For the alloys that were tested, the γ–phase is the stable phase, and the δ–phase is the metastable phase. Therefore, the subscript SM corresponds to $\gamma\delta$.

$$Q_1 + Q_2 = (-(\Delta H_{f,S} - J_S/V) + C_P^L \Delta T_{SM}) V_1 + (\Delta H_{f,M} + C_P^L \Delta T_{SM}) V_2 = 0 \quad (6.4)$$

Solving for the ratio of V_2 to V_1 results in Equations (6.5) and (6.6).

$$\frac{V_2}{V_1} = V_R = \frac{\Delta H_{f,S} - J_S/V - C_P^L \Delta T_{SM}}{\Delta H_{f,M} + C_P^L \Delta T_{SM}} \quad (6.5)$$

or

$$\frac{V_2}{V_1 + V_2} = \frac{1}{1/V_R + 1} \quad (6.6)$$

Next, consider only the energy absorbed in regions 1 and 2

$$Q_{abs} = C_P^L \Delta T_{SM}(V_1 + V_2) + \Delta H_{f,M} V_2. \quad (6.7)$$

The energy absorbed per unit volume is therefore:

$$q_{abs} = \frac{Q_{abs}}{V_1 + V_2} = C_P^L \Delta T_{SM} + \Delta H_{f,M} \frac{V_2}{V_1 + V_2}. \quad (6.8)$$

Combining Equations (6.6) and (6.8) yields:

$$q_{abs} = C_P^L \Delta T_{SM} + \Delta H_{f,M} \frac{1}{1/V_R + 1}. \quad (6.9)$$

Considering that the entire energy transfer occurs between the temperature of the metastable phase, T_M, and the temperature of the stable phase, T_S, then the effective heat capacity is given as follows:

$$C_P^{Eff} = \frac{q_{abs}}{\Delta T_{SM}} = C_P^L + \frac{\Delta H_{f,M}}{\Delta T_{SM}} \frac{1}{1/V_R + 1}. \quad (6.10)$$

6.1.2   Application Within the Dendrite Growth Model

With the effective heat capacity evaluated, it is possible to apply it within a dendrite growth model. The growth of the stable phase into the mushy zone was assessed using Lipton-Kurz-Trivedi (LKT) theory [72], including the kinetic undercooling component from Boettinger-Coriell-Trivedi (BCT) theory [89], and non-equilibrium effects discussed in Section 2.3.3..

The undercooling is given by:

$$\Delta T = \Delta T_T + \Delta T_R + \Delta T_C + \Delta T_K \tag{6.11}$$

where ΔT_T is the thermal undercooling, ΔT_R is the curvature undercooling, ΔT_C is the solutal undercooling, and ΔT_K is the kinetic undercooling. All values of undercooling are with respect to the phase of interest. The curvature undercooling, ΔT_R, is given in Equation (6.12).

$$\Delta T_R = 2\frac{\Gamma}{R} \tag{6.12}$$

R is the radius of the dendrite tip, and Γ is the Gibbs-Thomson coefficient, given by:

$$\Gamma = \frac{\sigma}{\Delta S_f}, \tag{6.13}$$

where ΔS_f is the entropy of fusion, and σ is the solid-liquid interfacial energy. The solutal undercooling, including non-equilibrium effects, is given in Equation (6.14).

$$\Delta T_C = m_L C_o \left[1 - \frac{m_v}{m_L[1 - (1 - k_v)Iv(P_c)]} \right] \tag{6.14}$$

m_L is the slope of the liquidus line from the equilibrium phase diagram, m_v is the non-equilibrium liquidus slope [89], C_o is the solute concentration, k_v is the velocity-dependent partitioning coefficient according to the model by Aziz and Kaplan [86], and P_c is the solutal Peclet number.

$$m_v = m_L \left[\frac{1 + [k_e - k_v(1 - ln(k_v/k_e))]}{1 - k_e} \right] \tag{6.15}$$

k_e is the equilibrium partition coefficient.

$$k_v = \frac{k_e + V/V_d}{1 - (1 - k_e)X_o + V/V_d} \tag{6.16}$$

X_o is the initial solute atomic fraction, V is the solidification velocity, and V_d is the atomic diffusive speed, shown in Equation (6.17).

$$V_d = D_o/a_o \tag{6.17}$$

$$P_c = \frac{VR}{2D_o} \tag{6.18}$$

D_o is the solute diffusivity, and a_o is the atomic spacing in the liquid. The kinetic undercooling, ΔT_K, for growth of a solid into a liquid is given in Equation (6.19).

$$\Delta T_K = V/\mu \tag{6.19}$$

μ is the kinetic growth coefficient, shown in Equation (6.20).

$$\mu = \frac{\Delta H_f V_o}{\bar{R} T_m^2} \tag{6.20}$$

T_m is the melting temperature, $\bar{R}$ is the universal gas constant, and V_o is the kinetic rate parameter, where $V_d < V_o < V_S$. V_S is the speed of sound through the liquid, and V_d is the diffusive speed defined above.

If there is some heat flux back down the length of the dendrite due to the presence of an adjacent metastable solid phase, the heat of fusion that is observed by the surrounding liquid will be reduced by some amount related to the heat flux. Therefore, a heat flux dependent kinetic growth coefficient, μ_{J_S}, should be applied within to kinetic undercooling, as represented in Equation (6.21).

$$\Delta T_K = V/\mu_{J_S} \tag{6.21}$$

The heat flux dependent kinetic growth coefficient, μ_{J_S}, is given in Equation (6.22).

$$\mu_{J_S} = \mu \frac{\Delta H_{f,S} - J_S/V}{\Delta H_f} = \frac{(\Delta H_{f,S} - J_S/V)V_o}{\bar{R} T_m^2} \tag{6.22}$$

The thermal undercooling, ΔT_T, with dendrite heat flux considerations, is presented in Equation (6.23).

$$\Delta T_T = \frac{Iv(P_t)}{C_P^L}(\Delta H_{f,S} - J_S/V) \tag{6.23}$$

The thermal undercooling given in Equation (6.23) is mathematically compara-

ble to the equation that Koseki [8] presented within his analysis of dendrite growth during chill casting. C_P^L is the heat capacity of the undercooled liquid, ΔH_f is the heat of fusion, and $Iv(P_t)$ is the Ivantsov function of the thermal Peclet number, P_t. Applying the effective heat capacity, C_P^{Eff}, within the thermal undercooling results in Equation (6.24).

$$\Delta T_T = \frac{Iv(P_t)}{C_P^{Eff}}(\Delta H_{f,S} - J_S/V) \tag{6.24}$$

$$P_t = \frac{VR}{2\alpha_L} \tag{6.25}$$

α_L is the thermal diffusivity of the liquid. Lastly, it is necessary to evaluate the stability criterion to solve for the growth velocity. The undercooling equation provides a relationship for VR, however, another equation is necessary in order to solve for the values of velocity at a given undercooling. The second equation comes from the dendrite tip selection condition. The stability criterion from Trivedi and Kurz [71] was applied within the current work, where the general form is given in Equations (2.33)-(2.38).

The non-equilibrium partition coefficient, k_v, is applied within the the solutal stability function, ξ_C, and the solute gradient in the liquid, G_C, given Equations (2.36) and (2.38), in place of the equilibrium partition coefficient k_e.

Considering the proposed dendrite growth geometry and the localized nature of possible perturbations at the solid-liquid interface, the dendrite tip stability was assumed to behave in the manner of a solid growing into a liquid with included quenching effects. Koseki [8] previously assessed the stability criterion under those conditions. The description of the stability criterion with quenching considerations is given in Section 2.3.4.

Due to the presence of the dendritic structure of the metastable phase, there should be no melt convection in the mushy zone. Typically, external melt convection effects are negligible, even for a solid growing into undercooled liquid, if the convection velocity is significantly lower than solidification speed. Therefore, external flow considerations were neglected within the stability parameter. In general, the application of the marginal stability criterion within the perturbation analysis predicts experimental results well, and reduces the number of unknowns and adjustable parameters within the analysis. For these reasons, the stability parameter, σ^*, was chosen to be equal to $1/4\pi^2$ within the current work.

In the remainder of the article, this solution will be assessed using experimental results from the Fe–Co and Fe–Cr–Ni alloy systems. The δ–phase (BCC) is the metastable phase and the γ-phase (FCC) is the stable phase for both of the alloy systems. The Fe–Cr–Ni alloys must be treated as a pseudo-binary system within the solidification analysis. Images of the $Fe_{70}Cr_xNi_{30-x}$ wt.% and $Fe_{72}Cr_xNi_{28-x}$ wt.% pseudobinary phase diagrams are given in Appendix B. Koseki [10] previously showed that the δ–phase primarily rejects nickel, while the γ–phase rejects chromium. Therefore, nickel was treated as the solute for the δ–phase, and chromium was treated as the solute for the γ–phase. The focus of this analysis consists of analyzing growth of the γ–phase through the mushy zone, however, it was necessary to evaluate both solid phases growing through undercooled liquid in order to obtain the appropriate values of the kinetic coefficient, μ. Tables 5.1 and 5.2 show the thermophysical property values that were used in the analysis.

6.2 Results and Discussion

Figures 6.3 and 6.4 show the velocity curves that resulted from the mushy-zone growth velocity analyses, where the velocities at the minimum undercooling of each curve are marked as the calculated values. The results indicate that for a given heat flux along the metastable dendrites, J_S, there is a minimum undercooling for which dendritic growth can be supported [8]. That minimun undercooling shall be referred to as ΔT_{J_S}. For the unique value of J_S, such that $\Delta T_{J_S} = \Delta T_{\gamma\delta}$, there is a unique growth velocity solution. Similarly, there are singular values of C_P^{Eff}, P_T, and R. The particular values of P_T and R are referred to as P_{T,J_S} and R_{J_S}.

Figure 6.3: Fe–Co mushy-zone growth velocity results. Error bars on experimental data correspond to plus or minus one standard deviation from the mean. □ Measured $\bar{V}_{\gamma\delta}$ = 1.6 m/s for Fe$_{70}$Co$_{30}$ at.%; ○ Predicted $\bar{V}_{\gamma\delta}$ = 0.9 m/s for Fe$_{70}$Co$_{30}$ at.%; ▨ Measured $\bar{V}_{\gamma\delta}$ = 2.4 m/s for Fe$_{60}$Co$_{40}$ at.%; ● Predicted $\bar{V}_{\gamma\delta}$ = 2.2 m/s for Fe$_{60}$Co$_{40}$ at.%; ■ Measured $\bar{V}_{\gamma\delta}$ = 4.9 m/s for Fe$_{50}$Co$_{50}$ at.%; ● Predicted $\bar{V}_{\gamma\delta}$ = 3.5 m/s for Fe$_{50}$Co$_{50}$ at.%; ——— Growth velocity curve for Fe$_{70}$Co$_{30}$ at.%; ——— Growth velocity curve for Fe$_{60}$Co$_{40}$ at.%; ——— Growth velocity curve for Fe$_{50}$Co$_{50}$ at.%.
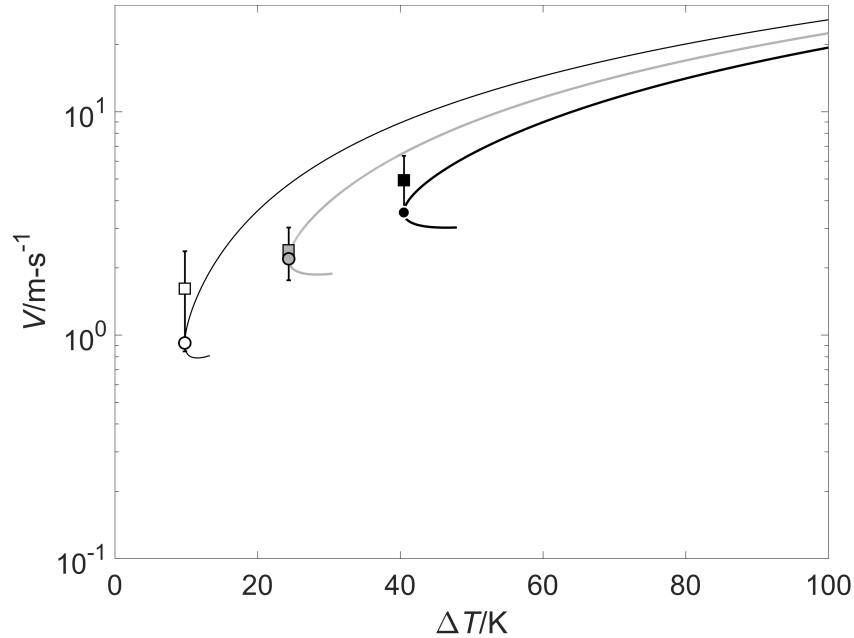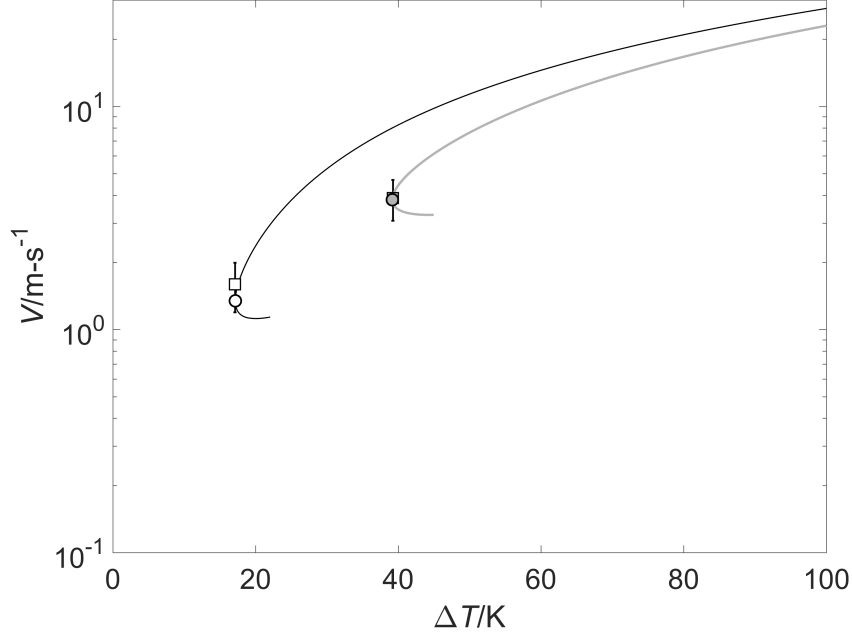
Figure 6.4: Fe–Cr–Ni mushy-zone growth velocity results. Error bars on experimental data correspond to plus or minus one standard deviation from the mean. □ Measured $\bar{V}_{\gamma\delta}$ = 1.6 m/s for $Fe_{70}Cr_{15}Ni_{15}$ wt.% [11]; ○ Predicted $\bar{V}_{\gamma\delta}$ = 1.3 m/s for $Fe_{70}Cr_{15}Ni_{15}$ wt.%; ■ Measured $\bar{V}_{\gamma\delta}$ = 3.9 m/s for $Fe_{72}Cr_{12}Ni_{16}$ wt.% [12]; ● Predicted $\bar{V}_{\gamma\delta}$ = 3.8 m/s for $Fe_{72}Cr_{12}Ni_{16}$ wt.%; ——— Calculated growth velocity curve for $Fe_{70}Cr_{15}Ni_{15}$ wt.%; ——— Calculated growth velocity curve for $Fe_{72}Cr_{12}Ni_{16}$ wt.%.

Tables 6.1 and 6.2 contain the summarized results of the Fe–Co and Fe–Cr–Ni growth velocity analyses. The validity of the model can be evaluated by comparing the predicted $\bar{V}_{\gamma\delta}$ with the measured $\bar{V}_{\gamma\delta}$. The calculated values of $\bar{V}_{\gamma\delta}$ are within one standard deviation of the measured values for each of the alloys that were tested. Given that the mushy-zone velocity corresponds to the velocity at the minimum undercooling for which dendritic growth can be supported, it is likely that the structure of the stable phase is not the same as that of a dendritic solid growing into pure liquid. The presence of the metastable phase likely creates preferential growth lanes, which results in the stable phase growing around the metastable solid, as Koseki [10] previously reported observing in micrographs which showed the stable γ–phase surrounding cores of the δ–phase dendrites.

With increasing thermal driving potential, $\Delta T_{\gamma\delta}$, C_P^{Eff} decreases while J_S increases. The effective heat capacity will eventually approach the heat capacity of the liquid, which means that $\bar{V}_{\gamma\delta}$ will approach $V_{\gamma L}$. However, the increasing heat flux suggests that there may be rapid coarsening effects due to the conduction from the dendrite tip. This makes sense intuitively because, by definition, as $\Delta T_{\gamma\delta}$ increases, the temperature difference between the stable and metastable phases increases.

Table 6.1: Results of mushy-zone growth velocity analysis for each Fe–Co alloy. The ± error margins were calculated at a 95 % confidence level.

Properties	$Fe_{70}Co_{30}$	$Fe_{60}Co_{40}$	$Fe_{50}Co_{50}$
$\mu_{\gamma L}$ | $\mu_{\delta L}$ (m/s-K)	0.300 | 0.151	0.302 | 0.151	0.304 | 0.155
μ_{J_S} (m/s-K)	0.181	0.186	0.19
J_S (W/m²)	6.56 E8	1.52 E9	2.438 E9
C_P^{Eff} (J/m³-K)	6.495 E7	2.805 E7	1.813 E7
P_{T,J_S}	0.133	0.197	0.248
R_{J_S} (m)	1.6 E-6	9.6 E-7	7.4E-7
$\bar{V}_R$	0.706	0.641	0.555
Predicted $\bar{V}_{\gamma\delta}$ (m/s)	0.9	2.2	3.5
Measured $\bar{V}_{\gamma\delta}$ (m/s)	1.6 ± 0.45 *	2.4 ± 0.23	4.9 ± 0.27
Standard Deviation (m/s)	0.76	0.64	1.42
Num. $V_{\gamma\delta}$ Data Points	11	29	104

* Indicates that the values are based on few data points.

Table 6.2: Results of mushy-zone growth velocity analysis for each Fe–Cr–Ni alloy. The ± error margins were calculated at a 95 % confidence level.

Properties	$Fe_{72}Cr_{15}Ni_{15}$	$Fe_{72}Cr_{12}Ni_{16}$
$\mu_{\gamma L}$ | $\mu_{\delta L}$ (m/s-K)	0.351 | 0.14	0.361 | 0.148
μ_{J_S} (m/s-K)	0.219	0.227
J_S (W/m²)	7.49 E8	2.17 E9
C_P^{Eff} (J/m³-K)	3.416 E7	1.683 E7
P_{T,J_S}	0.166	0.277
R_{J_S} (m)	1.5 E-6	8.7 E-7
$\bar{V}_R$	0.579	0.463
Predicted $\bar{V}_{\gamma\delta}$ (m/s)	1.3	3.8
Measured $\bar{V}_{\gamma\delta}$ (m/s)	1.6 ± 0.39 * [11]	3.9 ± 0.31 [12]
Standard Deviation (m/s)	0.40	0.81
Num. $V_{\gamma\delta}$ Data Points	4	26

* Indicates that the values are based on few data points.

6.3 Conclusions

A new dendrite growth model for evaluating growth of a secondary solid phase through a matrix of pre-existing solid and liquid, where the primary solid has a lower melting temperature than the secondary solid, has been presented. The model was evaluated using mushy-zone growth velocity data from Fe–Co and Fe–Cr–Ni alloys. The Fe–Co alloys that were tested are hyper-peritectic compositions, while the Fe–Cr–Ni alloys were evaluated as pseudobinary hypoeutectic compositions.

The results show that for a given heat flux, there will be a minimum undercooling for which dendritic growth can be supported. By varying the heat flux, it is possible to match that minimum undercooling with the known thermal driving force between the metastable and stable phases of a given alloy system. The predicted growth velocity which corresponds to that minimum undercooling, agrees reasonably well with the measured experimental growth velocity data. This suggests that the growth of the stable phase into the mushy zone occurs under the minimum conditions required to support dendritic growth. Additionally, if expanded, this model can serve as the foundation to approximate grain refinement that results from double recalescence, which Flemings *et al.* [19] previously observed.

Chapter 7

Future Work

Future work should consist of applying the thermodynamic modeling techniques and growth kinetics analyses to intermetallic compounds and solid solutions that exhibit significant partitioning.

A longer-term goal regarding the thermodynamic modeling would be to develop a method to reasonably predict the excess free energy of a solution. In order for thermodynamic modeling to achieve a high level predictive accuracy, there needs to be a way to estimate the excess Gibbs energy of mixtures. The excess Gibbs energy accounts for nonidealities that occur in mixtures, which makes this an extremely difficult problem to solve.

The mushy-zone growth model, presented in Chapter 6, only considers the thermal aspects of stable phase dendrite growth in the presence of a preexisting metastable phase. There are two considerations that should be addressed: 1) the liquid that exists in the mushy-zone can have a different concentration than the bulk liquid did. 2) When the metastable phase is remelted, some trapped solute will be reintroduced back into the system. These considerations did not appear to have a significant impact on the alloys that were studied

in this work, however, they may play a substantial role in alloys that exhibit more partitioning, or in intermetallic systems with ordered phases. Therefore, future work regarding the mushy-zone growth model should involve including solutal considerations within the analysis.

Bibliography

[1] John P. Holdren. Materials genome initiative for global competitiveness. Technical report, National Science and Technology Council OSTP, Washington, USA, 2011.

[2] Committee on Integrated Computational Materials Engineering. *Integrated Computational Materials Engineering: A Transformational Discipline for Improved Competitiveness and National Security*. National Academies Press, Washington, D.C., September 2008.

[3] David A. Porter and Kenneth E. Easterling. *Phase Transformations in Metals and Alloys*. CRC Press, second edition edition, 2004.

[4] Justin E. Rodriguez and Douglas M. Matson. Thermodynamic modeling of the solidification path of levitated Fe–Co alloys. *Calphad*, 49:87–100, June 2015.

[5] R. Hermann and W. Löser. Growth kinetics of undercooled Fe–Co melts. *Journal of Magnetism and Magnetic Materials*, 242–245, Part 1:285–287, April 2002.

[6] R. Hermann, W. Löser, G. Lindenkreuz, A. Diefenbach, W. Zahnow, W. Dreier, Th. Volkmann, and D. Herlach. Metastable phase formation

in undercooled Fe–Co melts. *Materials Science and Engineering: A*, 375–377:507–511, July 2004.

[7] R. Hermann, W. Löser, H. G. Lindenkreuz, W. Yang-Bitterlich, Ch. Mickel, A. Diefenbach, S. Schneider, and W. Dreier. Metastable phase formation in undercooled Fe-Co melts under terrestrial and parabolic flight conditions. *Microgravity - Science and Technology*, 19(1):5–10, December 2007.

[8] Toshihiko Koseki. *Undercooling and rapid solidification of Fe-Cr-Ni ternary alloys*. Thesis, Massachusetts Institute of Technology, 1994.

[9] Toshihiko Koseki and Merton C Flemings. Solidification of undercooled Fe-Cr-Ni alloys: Part I. Thermal behavior. *Metallurgical and Materials Transactions A*, 26(11):2991–2999, 1995.

[10] T Koseki and M C Flemings. Solidification of undercooled Fe-Cr-Ni alloys: Part II. Microstructural evolution. *Metallurgical and Materials Transactions A*, 27(10):3226–3240, 1996.

[11] Douglas M. Matson, A. Shokuhfar, John W. Lum, and Merton C. Flemings. Imaging the double-recalescence behavior of undercooled Fe-Cr-Ni alloys using a Highspeed video technique. *Solidification Science and Processing (eds I. Ohnaka and DM Stefanescu), TMS, Warrendale, PA*, pages 19–26, 1996.

[12] D. M. Matson. Growth Competition During Double Recalescence in Fe-Cr-Ni Alloys. In *Materials in Space-Science, Technology & Exploration*, volume 551 of *MRS Online Proceedings Library Archive*, pages 227–234, 1998.

[13] Mingjun Li, Xin Lin, Guangsheng Song, Gencang Yang, and Yaohe Zhou.

Microstructure evolution and metastable phase formation in undercooled Fe–30 at.% Co melt. *Materials Science and Engineering: A*, 268(1–2):90–96, August 1999.

[14] Toshihiko Koseki and Merton C Flemings. Solidification of undercooled Fe-Cr-Ni alloys: Part III. Phase selection in chill casting. *Metallurgical and Materials Transactions A*, 28(11):2385–2395, 1997.

[15] W. Löser, T. Volkmann, and D. M. Herlach. Nucleation and metastable phase formation in undercooled Fe-Cr-Ni melts. *Materials Science and Engineering: A*, 178(1):163–166, April 1994.

[16] S. A. Moir and D. M. Herlach. Observation of Phase Selection From Dendrite Growth in Undercooled Fe-Ni-Cr Melts. *Acta Materialia*, 45(7):2827–2837, July 1997.

[17] T. Volkmann, D. M. Herlach, and W. Löser. Nucleation and phase selection in undercooled Fe-Cr-Ni melts: Part I. Theoretical analysis of nucleation behavior. *Metallurgical and Materials Transactions A*, 28(2):453–460, February 1997.

[18] T. Volkmann, D. M. Herlach, and W. Löser. Nucleation and phase selection in undercooled Fe-Cr-Ni melts: Part II. Containerless solidification experiments. *Metallurgical and Materials Transactions A*, 28(2):461–469, February 1997.

[19] M. C. Flemings, D. M. Matson, W. Löser, R. Hyers, and J. Rogers. Science Requirements Document (SRD) for Levitation Observation of Dendrite Evolution in Steel Ternary Alloy Rapid Solidification (LODESTARS). *NASA Document LODESTARS-RQMT-0001*, 2003.

[20] M. Asta, C. Beckermann, A. Karma, W. Kurz, R. Napolitano, M. Plapp,

G. Purdy, M. Rappaz, and R. Trivedi. Solidification microstructures and solid-state parallels: Recent developments, future directions. *Acta Materialia*, 57(4):941–971, February 2009.

[21] M. E. Glicksman, R. J. Schaefer, and J. D. Ayers. Dendritic growth-A test of theory. *Metallurgical Transactions A*, 7(11):1747–1759, November 1976.

[22] Martin E. Glicksman, Matthew B. Koss, Laura T. Bushnell, Jeffrey C. Lacombe, and Edward A. Winsa. Dendritic Growth of Succinonitrile in Terrestrial and Microgravity Conditions as a Test of Theory. *ISIJ International*, 35(6):604–610, 1995.

[23] S. Reutzel, H. Hartmann, P. K. Galenko, S. Schneider, and D. M. Herlach. Change of the kinetics of solidification and microstructure formation induced by convection in the Ni–Al system. *Applied Physics Letters*, 91(4):041913, July 2007.

[24] Robert W. Hyers, Douglas M. Matson, Kenneth F. Kelton, and Jan R. Rogers. Convection in Containerless Processing. *Annals of the New York Academy of Sciences*, 1027(1):474–494, November 2004.

[25] Douglas M. Matson, David J. Fair, Robert W. Hyers, and Jan R. Rogers. Contrasting Electrostatic and Electromagnetic Levitation Experimental Results for Transformation Kinetics of Steel Alloys. *Annals of the New York Academy of Sciences*, 1027(1):435–446, November 2004.

[26] Douglas M. Matson, Robert W. Hyers, and Thomas Volkmann. Peritectic alloy rapid solidification with electromagnetic convection. *JASMA: Journal of the Japan Society of Microgravity Application*, 27(4):238–244, 2010.

[27] R. W. Hyers, G. Trapaga, and B. Abedian. Laminar-turbulent transition in an electromagnetically levitated droplet. *Metallurgical and Materials Transactions B*, 34(1):29–36, February 2003.

[28] A. B. Hanlon, Douglas M. Matson, and Robert W. Hyers. Internal Convective Effects on the Lifetime of the Metastable Phase Undercooled Fe–Cr–Ni Alloys. *Philosophical Magazine Letters*, 86(3):165–174, 2006.

[29] D. M. Matson. Unpublished Personal Communication, 2016.

[30] Josiah Willard Gibbs. On the Equilibrium of Heterogeneous Substances. *Transactions of the Connecticut Academy of Arts and Sciences*, 3:300–320, 1879.

[31] P. J. Spencer. A brief history of CALPHAD. *Calphad*, 32(1):1–8, March 2008.

[32] Hans Leo Lukas, Suzana G. Fries, and Bo Sundman. *Computational thermodynamics: the Calphad method*, volume 131. Cambridge university press Cambridge, 2007.

[33] A. Fernández Guillermet and Per Gustafson. An Assessment of the Thermodynamic Properties and the(p, T) Phase Diagram of Iron. *High Temperatures–High Pressures*, 16(6):591–610, 1984.

[34] A. Fernández Guillermet. Critical evaluation of the thermodynamic properties of cobalt. *International Journal of Thermophysics*, 8(4):481–510, July 1987.

[35] A. Fernandez Guillermet. Critical evaluation of the thermodynamic properties of the iron-cobalt system. *High Temperatures-High Pressures*, 19(5):477–499, 1987.

[36] A. T. Dinsdale. SGTE data for pure elements. *Calphad*, 15(4):317–425, October 1991.

[37] A. T. Dinsdale. SGTE data for pure elements. Technical report, NPL Materials Centre, 2001.

[38] T. G. Woodcock, R. Hermann, and W. Löser. Development of a metastable phase diagram to describe solidification in undercooled Fe–Co melts. *Calphad*, 31(2):256–263, June 2007.

[39] W. C. Ellis and E. S. Greiner. Equilibrium relations in the solid state of the iron-cobalt system. *Trans. ASM*, 29(2):415–432, 1941.

[40] H. Masumoto. On a New Transformation of Cobalt and the Equilibrium Diagrams of Nickel-Cobalt and Iron-Cobalt. Part 1. New Transformation of Cobalt. *Sci. Repts. Tohoku Imp. Univ*, 15:463, 1926.

[41] H. Masumoto. On the Equilibrium Diagram of Co-Fe Binary Alloys. *Nippon Kinzoku Gakkaishi*, 42(3):256–260, 1978.

[42] W. A. Fischer, K. Lorenz, H. Fabritius, and D. Schlegel. Examination of alpha/gamma Transformation in Very Pure Binary Alloys of Iron with Molybdenum, Vanadium, Tungsten, Niobium, Tantalum, Zirconium, and Cobalt. *Arch. Eisenhuettenw.*, 41:489–498, May 1970.

[43] A. S. Normanton, P. E. Bloomfield, F. R. Sale, and B. B. Argent. A Calorimetric Study of Iron–Cobalt Alloys. *Metal Science*, 9(1):510–517, January 1975.

[44] G. B. Harris and W. Hume-Rothery. The Liquidus-Solidus Relations in the System Iron-Cobalt in the Range 0-30 Atomic % Cobalt. *Journal of the Iron and Steel Institute*, 174(3):212–218, July 1953.

[45] Bruno Predel and Rudolf Mohs. Thermodynamische Untersuchung der Systeme Eisen-Nickel und Eisen-Kobalt. *Arch. Fur das Eisenhuttenwessen*, 41(2):143–149, 1970.

[46] Franz Müller and F. H. Hayes. The thermodynamic properties of iron + cobalt alloys I. Calorimetric study of the solid alloys. *The Journal of Chemical Thermodynamics*, 3(5):599–607, September 1971.

[47] R. Castanet and A. Ferrier. Experimental Determination of Calorific Capacity and Thermodynamic Functions of the Equimolecular Iron-Cobalt Alloy. *Comptes Rendus Hebdomadaires des Seances de L'Academie des Sciences Serie C*, 272(1):15, 1971.

[48] Tsuneo Satow, Sukeji Kachi, and Keizo Iwase. Thermodynamic Activities in Iron-Cobalt Solid Solutions. *Science reports of the Research Institutes, Tohoku University. Ser. A, Physics, chemistry and metallurgy*, 8:502–510, 1956.

[49] Von Walter Steiner and Otto Krisement. Bildungswärmen von alpha - und gamma - Eisen-Kobalt-Legierungen. *Archiv fur das Eisenhuttenwesen*, 33(12):877–881, December 1962.

[50] J. P. Hajra. *Thermodynamic measurements in the system fe co, cr-co and cr-co-fe, using solid oxide electrolytes.* PhD thesis, Thesis – University of Strathclyde, 1970.

[51] G. I. Batalin, N. N. Minenko, and V. S. Sudavtsova. Enthalpy of mixing and thermodynamic properties of molten alloys of Fe with Mn, Co and Ni. *Izvest. Akad. Nauk SSSR Metally*, 5:99–103, 1974.

[52] Y. Tozaki, Y. Iguchi, S. Banya, and T. Fuwa. Heat of mixing of iron alloys. In *Proc. Int. Symp. Met. Chemistry, Appl. Ferrous Met*, pages

19–21, 1973.

[53] W. Rammensee and Donald G. Fraser. Activities in Solid and Liquid Fe-Ni and Fe-Co Alloys Determined by Knudsen Cell Mass Spectrometry. *Berichte der Bunsengesellschaft für physikalische Chemie*, 85(7):588–592, July 1981.

[54] J. Vrestal, J. Velisek, and A. Rek. Determination of thermodynamic activities of components in the Fe–Co system at 1500 K. *Kovové Mater.*, 14:625–625, 1976.

[55] J. Tomiska. Determination of the Thermodynamic Mixing Properties of Solid Fe–Co Alloys by Knudsen Cell Mass Spectrometry and Calculation of the Phase Diagram. *Z. Metallkd.*, 77(2):97–102, 1986.

[56] J. Tomiska and A. Neckel. Knudsen Cell Mass Spectrometry: the Thermodynamic Mixing Functions of Liquid Fe–Co Alloys. *Z. Metallkd.*, 77(10):649–653, 1986.

[57] Geoffrey R. Belton and Richard J. Fruehan. Determination of activities by mass spectrometry. I. The liquid metallic systems iron-nickel and iron-cobalt. *The Journal of Physical Chemistry*, 71(5):1403–1409, April 1967.

[58] N. Maruyama and Shiro Ban-Ya. Measurement of Activities in Liquid Fe–Ni, Fe–Co and Ni–Co Alloys by a Transportation Method. *Journal of the Japan Institute of Metals*, 42(10):992–999, 1978.

[59] R. Trivedi and W. Kurz. Dendritic growth. *International Materials Reviews*, 39(2):49–74, January 1994.

[60] Francis I. Versnyder and M. E. Shank. The development of columnar grain and single crystal high temperature materials through directional

solidification. *Materials Science and Engineering*, 6(4):213–247, October 1970.

[61] A. Papapetrou. Investigations on the Dendrite Growth of Crystals. *Zeitschrift Fur Kristallographie*, 92(1/2):89–129, 1935.

[62] G. P. Ivantsov. The temperature field around a spherical, cylindrical, or pointed crystal growing in a cooling solution. In *Dokl. Akad. Nauk SSSR*, volume 58, pages 567–569, 1947.

[63] D. E. Temkin. Condition for the Stability of the Solid-Liquid Interface During The Crystallization of a Binary Alloy. *Doklady Akademii Nauk SSSR*, 133(1):174–177, 1960.

[64] G. R. Kotler and L. A. Tarshis. An extension to the analysis of dendritic growth in pure systems. *Journal of Crystal Growth*, 5(2):90–98, April 1969.

[65] R Trivedi. Growth of dendritic needles from a supercooled melt. *Acta Metallurgica*, 18(3):287–296, March 1970.

[66] W. W. Mullins and R. F. Sekerka. Stability of a Planar Interface During Solidification of a Dilute Binary Alloy. *Journal of Applied Physics*, 35(2):444–451, February 1964.

[67] J. S. Langer and H. Müller-Krumbhaar. Stability effects in dendritic crystal growth. *Journal of Crystal Growth*, 42:11–14, December 1977.

[68] J. S. Langer and H. Müller-Krumbhaar. Theory of dendritic growth—I. Elements of a stability analysis. *Acta Metallurgica*, 26(11):1681–1687, 1978.

[69] J. Lipton, M. E. Glicksman, and W. Kurz. Dendritic growth into undercooled alloy metals. *Materials Science and Engineering*, 65(1):57–63, July 1984.

[70] Alain Karma and J. S. Langer. Impurity effects in dendritic solidification. *Physical Review A*, 30(6):3147–3155, December 1984.

[71] R. Trivedi and W. Kurz. Morphological stability of a planar interface under rapid solidification conditions. *Acta Metallurgica*, 34(8):1663–1670, August 1986.

[72] J. Lipton, W. Kurz, and R. Trivedi. Rapid dendrite growth in undercooled alloys. *Acta Metallurgica*, 35(4):957–964, 1987.

[73] David A. Kessler and Herbert Levine. Velocity selection in dendritic growth. *Physical Review B*, 33(11):7867–7870, June 1986.

[74] David Bensimon, Pierre Pelcé, and Boris I. Shraiman. Dynamics of curved fronts and pattern selection. *Journal de Physique*, 48(12):2081–2087, 1987.

[75] P. Pelce and D. Bensimon. Theory of dendrite dynamics. *Nuclear Physics B - Proceedings Supplements*, 2:259–270, November 1987.

[76] Martine Benamar. Dendritic growth rate at arbitrary undercooling. *Physical Review A*, 41(4):2080–2092, February 1990.

[77] Angelo Barbieri. Velocity selection at large undercooling in a two-dimensional nonlocal model of solidification. *Physical Review A*, 36(11):5353–5358, December 1987.

[78] A. Barbieri and J. S. Langer. Predictions of dendritic growth rates in the linearized solvability theory. *Physical Review A*, 39(10):5314–5325,

May 1989.

[79] Ph. Bouissou and P. Pelcé. Effect of a forced flow on dendritic growth. *Physical Review A*, 40(11):6673–6680, December 1989.

[80] D. M. Herlach and P. K. Galenko. Rapid solidification: in situ diagnostics and theoretical modelling. *Materials Science and Engineering: A*, 449–451:34–41, March 2007.

[81] Dieter M. Herlach. Non-Equilibrium Solidification of Undercooled Metallic Melts. *Metals*, 4(2):196–234, June 2014.

[82] D. V. Alexandrov, P. K. Galenko, and D. M. Herlach. Selection criterion for the growing dendritic tip in a non-isothermal binary system under forced convective flow. *Journal of Crystal Growth*, 312(14):2122–2127, July 2010.

[83] Dmitri V. Alexandrov and Peter K. Galenko. Selection criterion of stable dendritic growth at arbitrary P\'eclet numbers with convection. *Physical Review E*, 87(6):062403, June 2013.

[84] D V Alexandrov and P K Galenko. Dendrite growth under forced convection: analysis methods and experimental tests. *Physics-Uspekhi*, 57(8):771–786, August 2014.

[85] Dmitri V. Alexandrov and Peter K. Galenko. Thermo-solutal and kinetic regimes of an anisotropic dendrite growing under forced convective flow. *Phys. Chem. Chem. Phys.*, 17(29):19149–19161, 2015.

[86] Michael J Aziz and Theodore Kaplan. Continuous growth model for interface motion during alloy solidification. *Acta Metallurgica*, 36(8):2335–2347, August 1988.

[87] J. C Baker and J. W Gahn. Solute trapping by rapid solidification. *Acta Metallurgica*, 17(5):575–578, May 1969.

[88] M. J. Aziz, J. Y. Tsao, M. O. Thompson, P. S. Peercy, and C. W. White. Solute Trapping: Comparison of Theory with Experiment. *Physical Review Letters*, 56(23):2489–2492, June 1986.

[89] W. J. Boettinger, S. R. Coriell, and R. Trivedi. Application of dendritic growth theory to the interpretation of rapid solidification microstructures. *Rapid Solidification Processing: Principles and Technologies IV*, page 13, 1988.

[90] D. M. Herlach, R. F. Cochrane, I. Egry, H. J. Fecht, and A. L. Greer. Containerless processing in the study of metallic melts and their solidification. *International Materials Reviews*, 38(6):273–347, January 1993.

[91] Jan Rogers and Michael Sansoucie. Containerless Processing Studies in the MSFC Electrostatic Levitator. In *50th AIAA Aerospace Sciences Meeting including the New Horizons Forum and Aerospace Exposition*. American Institute of Aeronautics and Astronautics, January 2012.

[92] James M Burke, Andrew J Mueller, David J Fair, and Douglas M Matson. Application of EM Levitation Processing: Fundamental Studies of Steel Rapid Solidification. In *Materials Science and Technology - Association for Iron and Steel Technology*, pages 71–78, 2005.

[93] Michael P. SanSoucie, Jan R. Rogers, and Douglas M. Matson. Rapid Quench in an Electrostatic Levitator. In *TMS 2016: 145 Annual Meeting & Exhibition: Supplemental Proceedings*, pages 31–34. John Wiley & Sons, Inc., 2016.

[94] D M Herlach. Containerless Undercooling and Solidification of Pure Metals. *Annual Review of Materials Science*, 21(1):23–44, 1991.

[95] Thomas A. Hughes. *Measurement and Control Basics*. ISA-The Instrumentation, Systems, and Automation Society, 2002.

[96] William Hofmeister, R. J. Bayuzick, and Shankar Krishnan. Optical pyrometry on TEMPUS: a critical assessment of noncontact temperature measurement in low earth orbit. volume 2809, pages 288–302, 1996.

[97] Hiromichi Watanabe, Masahiro Susa, Hiroyuki Fukuyama, and Kazuhiro Nagata. Phase (Liquid/Solid) Dependence of the Normal Spectral Emissivity for Iron, Cobalt, and Nickel at Melting Points. *International Journal of Thermophysics*, 24(2):473–488, 2003.

[98] H. B. Wahlin and Harry W. Knop. The Spectral Emissivity of Iron and Cobalt. *Physical Review*, 74(6):687–689, September 1948.

[99] Harry W. Knop. The Emissivity of Iron-Tungsten and Iron-Cobalt Alloys. *Physical Review*, 74(10):1413–1416, November 1948.

[100] D. M. Matson and R. W. Hyers. Adiabatic remelting of the mushy-zone during rapid solidification. *Philosophical Magazine*, 86(24):3795–3807, August 2006.

[101] D. M. Matson, R. W. Hyers, T. Volkmann, and H.-J. Fecht. Phase selection in the mushy-zone: LODESTARS and ELFSTONE projects. *Journal of Physics: Conference Series*, 327(1):012009, 2011.

[102] H. Hess, E. Kaschnitz, and G. Pottlacher. Thermophysical properties of liquid cobalt. *High Pressure Research*, 12(1):29–42, March 1994.

[103] J. A. Treverton and J. L. Margrave. Levitation calorimetry. IV. Thermodynamic properties of liquid cobalt and palladium. *The Journal of Physical Chemistry*, 75(24):3737–3740, November 1971.

[104] W. Löser. EML delay times of Fe–40 at.% Co, 2013. Published: Private Communication DLR, Köln, Germany.

[105] Carolina Kreischer and Thomas Volkmann. Growth Velocities and Delay Times of Various Fe-Co Alloys Processed in EML, 2015. Published: Private Communication DLR, Köln, Germany.

[106] W. F. Roeser and H. T. Wensel. Freezing Temperatures of High-Purity Iron and of Some Steels. *Journal of Research of the National Bureau of Standards*, 26:273–287, 1941.

[107] H. Preston-Thomas. The International Temperature Scale of 1990(ITS-90). *Metrologia*, 27(1):3–10, 1990.

[108] H. F. Stimson. The international temperature scale of 1948. *J. Res. Natl. Bur. Stand.(US)*, 42:209–217, 1949.

[109] Milton S. VanDusen and Andrew I. Dahl. Freezing Points of Cobalt and Nickel. *Journal of Research of the National Bureau of Standards*, 39:291–295, 1947.

[110] Irving Langmuir. The Vapor Pressure of Metallic Tungsten. *Physical Review*, 2(5):329–342, November 1913.

[111] J. Lee and D. M. Matson. Prediction of Mass Evaporation of Fe50co50 During Measurements of Thermophysical Properties Using an Electrostatic Levitator. *International Journal of Thermophysics*, 35(9-10):1697–1704, July 2014.

[112] Richard E. Honig and Dean A. Kramer. Vapor-pressure data for the solid and liquid elements. Technical report, RCA Laboratories, Princeton, New Jersey, 1970.

[113] Jonghyun Lee, Justin E. Rodriguez, Robert W. Hyers, and Douglas M. Matson. Measurement of Density of Fe-Co Alloys Using Electrostatic Levitation. *Metallurgical and Materials Transactions B*, 46(6):2470–2475, August 2015.

[114] Kenneth C. Mills. *Recommended values of thermophysical properties for selected commercial alloys*. Woodhead Publishing, 2002.

[115] Takamichi Iida and Roderick IL Guthrie. *The physical properties of liquid metals*. Oxford University Press Inc., 1993.

[116] Wilfried Kurz and David J. Fisher. *Fundamentals of solidification*. Trans Tech Publication Ltd, Switzerland, fourth edition, 1998.

[117] D. M. Matson. The mesurement of dendrite tip propagation velocity during growth into undercooled metallic melts. *Solidification 1998, Indianapolis, IN*, pages 233–244, 1998.

[118] Tsuyoshi Nishi, Hiroyuki Shibata, Yoshio Waseda, and Hiromichi Ohta. Thermal conductivities of molten iron, cobalt, and nickel by laser flash method. *Metallurgical and Materials Transactions A*, 34(12):2801–2807, December 2003.

[119] D. W. Morgan and J. A. Kitchener. Solutions in liquid iron. Part 3:—Diffusion of cobalt and carbon. *Transactions of the Faraday Society*, 50:51–60, 1954.

[120] D. Y. Sun, M. Asta, J. J. Hoyt, M. I. Mendelev, and D. J. Srolovitz. Crystal-melt interfacial free energies in metals: fcc versus bcc. *Physical*

Review B, 69(2):020102, January 2004.

[121] Gernot Pottlacher. *High temperature thermophysical properties of 22 pure metals.* Keiper, 2010.

[122] J-O Andersson, Thomas Helander, Lars Höglund, Pingfang Shi, and Bo Sundman. Thermo-Calc & DICTRA, computational tools for materials science. *Calphad*, 26(2):273–312, June 2002.

[123] Jackson R. Dolan. *Application of the adiabatic remelt model to the solidification of undercooled iron-cobalt alloys.* M.S., Tufts University, United States – Massachusetts, 2012.

[124] K. Eckler, R. F. Cochrane, D. M. Herlach, B. Feuerbacher, and M. Jurisch. Evidence for a transition from diffusion-controlled to thermally controlled solidification in metallic alloys. *Physical Review B*, 45(9):5019–5022, March 1992.

[125] P. K. Galenko, S. Reutzel, D. M. Herlach, D. Danilov, and B. Nestler. Modelling of dendritic solidification in undercooled dilute Ni–Zr melts. *Acta Materialia*, 55(20):6834–6842, December 2007.

[126] H. Hartmann, P. K. Galenko, D. Holland–Moritz, M. Kolbe, D. M. Herlach, and O. Shuleshova. Nonequilibrium solidification in undercooled Ti45al55 melts. *Journal of Applied Physics*, 103(7):073509, April 2008.

Appendix A

Camera and Pyrometer

Specifications

MI-S 140 · MI-GA 140

Highly accurate, fully digital, fast

Pyrometer with focusable optics for non-contact temperature measurements on metals, ceramics, graphite etc. between 572 and 5972°F

- ◆ Temperature ranges between 572 and 5972°F

- ◆ Fast response times < 1 ms
  optional 500 µs

- ◆ Extremly small spot sizes, min 0.014 in

- ◆ Built in digital display with temperature indication

- ◆ Precision thru-lens sighting
  or laser targeting

- ◆ Test current output

- ◆ Housing with precision mounting rail for
  safe mounting and accurate alignment

- ◆ Interface RS232 / RS485 switchable

- ◆ Focusable optics

The **MI-S140** and **MI-GA 140** are highly accurate, digitial pyometers for non-contact temperature measurement on metals, ceramics, graphite etc.
For optimal match of the intrument to the application 3 different focusable optics with extremly small spot sizes are available.
The pyrometer parameters can be selected via the integrated key pad, the settings are indicated on the built-in LCD-Display. In measuring mode the actual temperature is indicated.

The pyrometers are equipped with RS232 and RS485 serial interfaces (switchable inside the pyrometer). This enables the reading of temperature and pyrometer parameters via the provided InfraWin PC-software. If necessary the parameters also can be changed via PC.
A laser targeting or thru-lens viewfinder for exact alignment of the pyrometer is available.

Typical applications:

- preheating
- annealing
- tempering
- welding
- forging
- hardening
- sintering
- melting
- soldering
- rolling
- brazing
- normalizing

THE INFRARED PROS

Technical Data:

Temperature ranges:	see reference numbers, other temperature ranges on request
Subrange:	any range adjustable within the temperature range, minimum span 51°C
Spectral ranges:	MI-S 140: 0.7 ... 1.1 µm MI-GA 140 1.45 ... 1.8 µm
Signal processing:	photoelectric current, digitized immediately
Accuracy:	below 2732°F: 0.3% of measured value in °F +1.8°F
(ε = 1, t_{90} = 1 s, T_U = 23°C)	above 2732°F: 0.5% of measured value in °F
Repeatability:	0.1 % of measured value in °F +1.8°F , @ e=1; t90 = 1 s; Tamb = 23°C
Resolution:	interface: 0.1°F, analog output: < 0.1 % of temperature range
Response time t_{90}:	< 1 ms, adjustable up to 10 s ("L" temperature ranges: with dynamical adaption at low signal levels)
Emissivity ε:	0.200 ... 1.000 adjustable in steps of 0.001
Analog output:	linear 4 ... 20 mA or 0 ... 20 mA, DC, switchable; load max. 500 Ohm
Power supply:	24 V AC/DC (12 ... 30 V AC/DC) (AC: 48 ... 62 Hz)
Power consumption:	max. 2 VA
Sighting:	laser targeting or thru-lens view finder, Laser (650 nm), Laser power level <1 mW, CDRH Class II
Serial interface:	switchable inside the pyrometer: RS232 or RS485 addressable, half duplex; baud rate up to 115 kBd
Parameters:	adjustable at the instrument or via serial interface:
	emissivity; response time; analog output; address; baud rate; waiting period $t_{W;}$ °C or °F;
	setting of the maximum value storage; temperature sub range
Maximum value storage:	single or double storage; cleared by:
	- preselected time interval
	- external deletion contact or via digital interface
	- automatically with the next measuring object
Test current output:	fixed 12 mA (for 4 ... 20 mA analog output) or fixed 10 mA (for 0 ... 20 mA analog output)
Isolation:	power supply, digital interface, analog output are galvanically isolated against each other and housing
Enclosure rating:	IP65 (acc. to DIN 40 050)
Ambient temperature:	0 ... 70°C at housing
Storage temperature:	-4 ... 140°F
Weight:	approx. 19.4 oz.
Dimensions [in]:	7.7 x 2.2 x 2.5 (L x B x H)
CE-label:	according to EU directives about electromagnetic immunity

CAUTION
LASER RADIATION
DO NOT STARE INTO BEAM
WAVELENGTH: 630-680nm
<1mW MAXIMUM
CLASS II LASER PRODUCT

Advantages of the digital signal processing

The signal processing of series 140 pyrometers is fully digital, i.e. the detector signal are digitized immediately and digitally processed. With this technique an extremly high accuracy and repeatability as well as very long measuring ranges are achieved.

Accuracy:	The high accuracy will be achieved by the digital linearization of the sensor output as well as the digital compensation of the ambient temperature.
Temperature range:	Due to the digital technique the user can set any temperature sub range within the full temperature range. The minimum span of the sub range is 92°F. The analog measuring output corresponds automatically to the selected sub range. This setting of a sub range can be done without recalibration of the pyrometer and does not effect the high accuracy and repeatability. As almost any sub range is adjustable, the storage of spare instruments or the replacement of other pyrometers is simplified.
Output:	The analog measuring outputs 4 ... 20 mA or 0 ... 20 mA are selectable as well as the serial digital interfaces RS232 or RS485. Additionally the interface allows the controlling of the pyrometer via PC.
Bus control:	The RS485 serial interface facillitates the integration of the pyrometer into existing field bus systems.
Calibration:	If a suitable calibration source is available, a calibration of the pyrometers can be done via serial interface without opening the housing.

**Built-in
LCD-Display**

Optics

The series 140 pyrometers are available with 3 different focusable optics. They offer the smallest possible spot size at any distance. The adjustment can be done easily without additional tools with help of the "turn and clamp" mechanism (one hand). The spot sizes are shown in the following table. The different optics are interchangeable without recalibration of the pyrometer.
For measuring distances "a" within the values in the table also the spot sizes "M" are within the values in the table.

	Distance a	Spot size M
Optics 1:	5.1 in	0.014 in
(distance	6.3 in	0.020 in
5.1 ... 7.9 in)	7.9 in	0.028 in
Optics 2:	7.5 in	0.020 in
(distance	11.8 in	0.031 in
7.5 ... 16.5 in)	16.5 in	0.051 in
Optics 3:	13.4 in	0.035 in
(distance	78.8 in	0.256 in
13.4 ... 157.5 in)	157.5 in	0.591 in

Aperture D (depends on the objective distance):
Basic temperature range up to 2732°F: 0.551 ... 0.630 in
Basic temperature range above 2732°F: 0.315 ... 0.354 in

Reference numbers

Pyrometers (basic instruments are equipped with laser targeting):

5 875 100	MI-S 140	MB 14:	1022 ... 2552°F	5 875 300	MI-GA 140	MB 13:	572 ... 2372°F
5 875 120	MI-S 140	MB 16:	1112 ... 2912°F	5 875 320	MI-GA 140	MB 18:	662 ... 3272°F
5 875 140	MI-S 140	MB 18:	1202 ... 3272°F	5 875 340	MI-GA 140	MB 25:	842 ... 4532°F
5 875 160	MI-S 140	MB 25:	1382 ... 4532°F	5 875 360	MI-GA 140	MB 13.5 L:	482 ... 2462°F
5 875 180	MI-S 140	MB 33:	1652 ... 5972°F	5 875 380	MI-GA 140	MB 20 L:	572 ... 3632°F
5 875 200	MI-S 140	MB 18 L:	1022 ... 3272°F	5 875 400	MI-GA 140	MB 25 L:	662 ... 4532°F

Optional:
Thru-lens view finder instead of laser targeting (*add* **010** to the basic instruments ref. number, e.g. 5 875 110 instead of 5 875 100)

Ordering note:
When ordering please select one focusable optics.
A connection cable is not included in scope of delivery and and must be ordered separately.

Ordering example:
5 875 150   MI-S 140 with thru-lens view finder, focusable optics 2, temperature range 1202 ... 3272°F
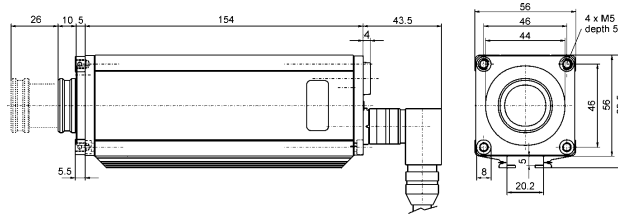5 820 530   connection cable, length 32 ft, with 90° connector

Scope of delivery: Pyrometer with focusable optics, *InfraWin* operating and analysis software
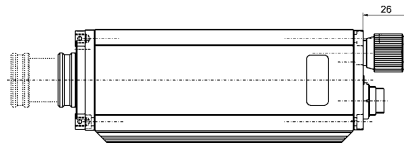
Accessories:

3 820 340	connection cable, length 16 ft, 90° connector	3 837 240	cooling plate
3 820 530	connection cable, length 32 ft, 90° connector	3 835 280	90° mirror
3 820 540	connection cable, length 49 ft, 90° connector	3 843 520	rugged scanner MI-SCA 140, (scanning angle ad-
3 820 830	connection cable, length 65 ft, 90° connector		justable 0 ... 12°, scanning frequency adjustable
3 820 840	connection cable, length 82 ft, 90° connector		1 ... 5 Hz), with quarz glass window
3 820 550	connection cable, length 98 ft, 90° connector	3 835 290	air purge for scanner SCA 140
3 820 330	connection cable, length 16 ft, straight connector	18712-2	power supply for DIN rail mounting;
3 820 500	connection cable, length 32 ft, straight connector		90 ... 250 V AC ⇒ 24 V DC, 420 mA
3 820 510	connection cable, length 49 ft, straight connector	18712-1	power supply:
3 820 810	connection cable, length 65 ft, straight connector		90 ... 250 V AC . 24 V DC, 420 mA
3 820 820	connection cable, length 82 ft, straight connector	17219-1	LED digital display M60TDS
3 820 520	connection cable, length 98 ft, straight connector	17219-1	LED digital display M60TDS: with 2 limit switches
3 820 740	connection cable, length 16 ft, straight connector,	5 890 560	LED digital display MI-DA 6000-N: with possibility for
	temperature resistant up to 392°F		pyrometer paramter settings for digital
3 820 750	connection cable, length 16 ft, 90° connector,		*INFRATHERM* pyrometers; RS232 interface
	temperature resistant up to 392°F	5 890 520	LED digital display MI-DA 6000; MI-DA 6000-N addi-
3 834 280	adjustable mounting angle		tional with 2 limit switches and analog input and
3 834 270	ball and socket mounting		output
3 835 230	air purge	3 890 660	IP 65 front cover for LED digital displays
3 837 290	cooling jacket, stainless steel	5 826 500	MI-HT 6000, portable battery driven indicator and
3 835 060	air purge for cooling jacket		instrument for pyrometer parameter setting

Dimensions

Pyrometer with laser targeting

26 10 5 154 43.5
4
56
46
44
4 x M5 depth 5
46 56 62.5
5.5
8 5
20.2

Pyrometer with thru-lens view finder

26

All dimensions in mm

Overview accessories

Ball and socket mounting

60
25
20
5
101
50
4.2
ø72

mounting angle

40
7 20
100°
50
5.2
5.2

36.8 6.4
6
8
34
40
60
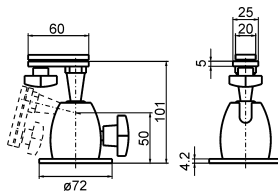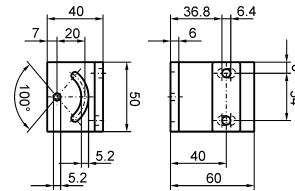
Cooling plate

90° mirror

air purge

Stainless steel cooling jacket

Scanner for small angles up to 12°

17219-1

LED digital display

MIKRON®
I N F R A R E D

Specifications are subject to change without notice

IT 4C3 MIS_MIGA140_e Rev 1.7 e F 072106

p h a n t o m v7.1

You asked for it: Faster, with longer recording times and more sensitivity . . . the new v7.1 is here!

With a new high resolution sensor featuring incredible speed and the sensitivity to take advantage of 1 μsec exposure times, the new Phantom v7.1 raises the bar in digital high-speed camera performance. This is a true replacement for many HS film applications, including most 16mm rotating prism requirements. Long record times for missile launch and flight missions are now supported with an option for real time streaming output!

☑ *Optional 12 bit SR-CMOS 800x600 pixel sensor, color or monochrome*

☑ *4800 ISO/ASA monochrome, 1200 ISO/ASA color sensitivity*

☑ *4,800pps full frame, 10,000pps at 512x384, 160,000 maximum*

☑ *"CAR" (Continuously Adjustable Resolution) in 16x8 pixel increments*

☑ *Global (snap-shot) on-chip shutter to 2 microseconds (1μsec optional)*

☑ *Auto Exposure control*

☑ *"EDR" Extreme Dynamic Range exposure control*

☑ *IRIG-B timing, modulated or unmodulated, IRIG lock w/phase shift*

☑ *Optional continuous data streaming up to 2,000pps (8 bit)*

☑ *Range data input*

☑ *Continuous color video output*

☑ *Automated multiple session recording for remote unmanned operation*

☑ *Rugged high-G configuration*

☑ *Gigabit Ethernet, or RS232 control*

☑ *100% compatibility with Phantom v4, v5, v6 and v9 cameras!*

v7.1 Maximum Recording Speed vs. Image Size

The Phantom v7.1 camera systems can record up to 4,800 pictures per second using the full 800x600 pixel SR-CMOS imaging sensor array. The operator may also specify other aspect ratios to increase recording speeds or extend recording times.

The chart below details the Phantom v7.1 aspect ratio choices available in the setup screen pull down menu. Using the CAR (Continuously Adjustable Resolution) feature, speeds between these values are continuously adjustable in 16x8 pixel increments.

Resolution	Rate
800x600	4,800
640x480	7,300
320x240	24,400
160x120	64,500
512x512	8,300
512x384	10,900
512x256	16,000
512x128	29,600
512x64	51,500
384x512	10,600
256x512	14,500
256x256	27,000
256x128	47,600
256x64	76,900
128x512	23,000
128x256	41,300
128x128	68,500
128x64	102,000
64x64	121,000
32x32	160,000

PRINT PDF

Y4-S1 SPECIFICATION SHEET

The Y4 is the most versatile camera system, useful in production and research and development environments. This camera system can be operated in an extended dynamic range (EDR) mode to produce either 11-bit or 12-bit images.

KEY FEATURES

Maximum Resolution	1024 x 1024
Maximum FPS @ Maximum Resolution	3,000 fps
Maximum FPS @ Maximum Resolution (Plus Mode)	6,000 fps
Image Storage @ Max Frame Rate (DDR 8)	6,142
Image Storage @ Max Frame Rate (DDR 16)	12,497

FEATURES

Approx. Size	103 x 96 x 228 mm (W x H x L)
Approx. Weight	3.4 kg or 7.5 lbs
Shock/Vibration Rating	Shock: 200G / Vibration: 40G - All axes
Battery Powered Operation Time	Operation and battery back-up up to 1 hours
Mount	C-Mount standard , F&PL Adaptor optional

Image Storage @ Max Frame Rate (DDR 32)	25,207
Image Storage @ Max Frame Rate (DDR 64)	50,627
Maximum FPS	130,000 @ 1024 x 8
Minimum Exposure Time	1µs
Sensitivity ASA/ISO	6000 ISO Mono 2000 ISO Color
Power Requirements	minimum 12V , 2 A
Operating Temperature	-40+50 °C / -40+122 °F

SENSOR

Sensor Type	CMOS - Proprietary
Sensor Size	13.9 x 13.9 mm
Sensor Format	1 inch
Pixel Size (micron)	13.68x13.68 um
Pixel Depth	10 bit mono 30 bit color

INPUTS

Trigger	TTL & Switch/Circular buffer with on-camera or software trigger
Sync	Phase-lock TTL
IRIG	Optional

SOFTWARE

Motion Studio	Windows 32/64
Motion Inspector	Windows 32/64 - MAC OS X - Apple iOS
Plug-ins/SDK	SDK, LabVIEW™ or MatLab®
File Formats	Proprietary RAW
On-the-fly Conversion	TIF, BMP, JPG, PNG, AVI, MPG, TP2, MOV, MRF, MCF

COMMUNICATION

Ethernet	100/1000BaseT
USB2	Standard
WiFi	Optional

GPS Time Code	Standard

OUTPUTS

Sync	Frame sync / Strobe
HDMI	30 fps

Specifications are subject to change without notification. | Data accurate as of 10 May. 2016 | Please reference our website for updates: http://www.idtvision.com

Y7-S3 SPECIFICATION SHEET

New to the Y Series, the Y7 PIV model introduces a universal integrated timing interface. This allows for synchronization of any illumination sources such as lasers or LEDs. Together with our standard 200-nanosecond inter-frame time, the camera is perfectly suited for PIV researchers as it decreases PIV system size and cost.

KEY FEATURES

Maximum Resolution	1920 x 1080
Maximum FPS @ Maximum Resolution	12,300 fps
Image Storage @ Max Frame Rate (DDR 8)	10,908
Image Storage @ Max Frame Rate (DDR 16)	22,183
Image Storage @ Max Frame Rate (DDR 32)	44,733

FEATURES

Approx. Size	103 x 96 x 228 mm (W x H x L)
Approx. Weight	3.4 kg or 7.5 lbs
Shock/Vibration Rating	Shock: 200G / Vibration: 40G - All axes
Battery Powered Operation Time	Operation and battery back-up up to 1 hours
Mount	C-Mount standard , F&PL Adaptor optional

Image Storage @ Max Frame Rate (DDR 64)	89,833
Maximum FPS	300,000 @ 1920 x 8
Minimum Exposure Time	1µs
Sensitivity ASA/ISO	6000 ISO Mono 2000 ISO Color
Power Requirements	minimum 12V , 2 A
Operating Temperature	-40+50 °C / -40+122 °F

SENSOR

Sensor Type	CMOS - Proprietary
Sensor Size	13.9 x 7.8 mm
Sensor Format	1 inch
Pixel Size (micron)	7.24x7.24 um
Pixel Depth	10 bit mono 30 bit color

INPUTS

Trigger	TTL & Switch/Circular buffer with on-camera or software trigger
Sync	Phase-lock TTL
IRIG	Optional
GPS Time Code	Standard

SOFTWARE

Motion Studio	Windows 32/64
Motion Inspector	Windows 32/64 - MAC OS X - Apple iOS
Plug-ins/SDK	SDK, LabVIEW™ or MatLab®
File Formats	Proprietary RAW
On-the-fly Conversion	TIF, BMP, JPG, PNG, AVI, MPG, TP2, MOV, MRF, MCF

COMMUNICATION

Ethernet	100/1000BaseT
USB2	Standard
WiFi	Optional

126

OUTPUTS

Sync	Frame sync / Strobe
HDMI	30 fps

Specifications are subject to change without notification. | Data accurate as of 10 May. 2016 | Please reference our website for updates: http://www.idtvision.com

FASTCAM SA5
ULTRA HIGH-SPEED VIDEO SYSTEM

High-Speed Video System
Next generation CMOS sensor technology providing 7,500 fps, 1K x 1K pixels

The Photron FASTCAM SA5 will meet the requirements of the most demanding applications in research and development due to its unrivaled sensitivity, frame rate and resolution.

This high performance will permit the SA5 to be applied to areas of research once dismissed as unsuitable for digital high-speed imaging.

Building on the success of Photron's Emmy award winning high speed cameras our sensor design improves sensitivity, image quality and color reproduction.

The FASTCAM SA5 delivers mega-pixel resolution at 7,500 fps, an impressive maximum frame rate of 775,000 fps and a 1 microsecond exposure time. Optional one million fps and 369 ns shutter capabilities are available subject to export restrictions.

Target applications include:

- Materials research
- Combustion
- Ballistics
- Cavitation
- Aerospace
- Fluid dynamics
- PIV

Benefits

■ Performance examples:

- 1,024 x 1,000 pixels @ 7,500 fps
- 512 x 512 pixels @ 25,000 fps
- 256 x 256 pixels @ 87,500 fps
- 128 x 128 pixels @ 262,500 fps
- 128 x 24 pixels @ 775,000 fps

■ Variable Region of Interest (ROI)

■ Capture 12-bit uncompressed data

■ $20\mu m$ pixels ensure best light sensitivity for demanding high-speed or low light applications

■ Equivalent ISO light sensitivity 10,000 (monochrome), 4,000 (color) measured to ISO12232 S sat

■ Phase lock to IRIG/GPS

■ Composite and SDI video output for real time monitoring during set up, recording and playback

■ Optional remote keypad control with integrated viewfinder

■ 8GB, 16GB, 32GB or 64GB memory options

■ Gigabit Ethernet interface

Photron
www.photron.com

128

FASTCAM SA5
ULTRA HIGH-SPEED VIDEO SYSTEM
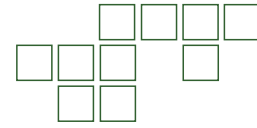
Specifications: Partial Frame Rate / Recording Duration Table

FRAME RATE (fps)	MAXIMUM RESOLUTION Horizontal	Vertical	MAXIMUM SHUTTER SPEED	RECORD DURATION (12-BIT) TIME (Sec.) 8GB	16GB	32GB	64GB	FRAMES 8GB	16GB	32GB	64GB
1,000	1,024	1,024		5.46	10.92	21.84	43.68	5,457	10,918	21,841	43,686
2,000	1,024	1,024		2.73	5.46	10.92	21.84	5,457	10,918	21,841	43,686
4,000	1,024	1,024		1.36	2.73	5.46	10.92	5,457	10,918	21,841	43,686
5,000	1,024	1,024		1.09	2.18	4.37	8.73	5,457	10,918	21,841	43,686
7,000	1,024	1,024		0.78	1.56	3.12	6.24	5,457	10,918	21,841	43,686
7,500	1,024	1,000		0.75	1.49	2.98	5.96	5,588	11,180	22,365	44,735
9,300	1,024	800		0.75	1.50	3.01	6.01	6,985	13,975	27,956	55,918
10,000	1,024	744	1 μs	0.75	1.50	3.01	6.01	7,511	15,027	30,061	60,127
15,000	960	528	1/1,000,000 sec	0.75	1.51	3.01	6.02	11,289	22,587	45,182	90,374
20,000	832	448		0.77	1.54	3.07	6.14	15,352	30,716	61,443	122,898
30,000	768	320		0.78	1.55	3.11	6.21	23,284	46,586	93,189	186,396
50,000	512	272		0.82	1.64	3.29	6.57	41,090	82,211	164,452	328,934
75,000	320	264		0.90	1.81	3.61	7.22	67,737	135,523	271,097	542,244
100,000	320	192		0.93	1.86	3.73	7.45	93,138	186,345	372,758	745,585
150,000	256	144		1.03	2.07	4.14	8.28	155,230	310,575	621,264	1,242,642
300,000	256	64		1.16	2.33	4.66	9.31	349,269	698,794	1,397,845	2,795,946
420,000	128	64		1.66	3.33	6.66	13.31	698,538	1,397,589	2,795,690	5,591,893
525,000	128	48		1.77	3.55	7.10	14.20	931,384	1,863,452	3,727,587	7,455,857
775,000	128	24		2.40	4.81	9.62	19.24	1,862,769	3,726,904	7,455,175	14,911,715
930,000	128	16	369 ns 1/2,712,000 sec	3.00	6.01	12.02	24.05	2,794,154	5,590,357	11,182,762	22,367,573
1,000,000	64	16		5.59	11.18	22.37	44.73	5,588,309	11,180,714	22,365,525	44,735,146

OPTION SUBJECT TO EXPORT LICENSE CONTROL RESTRICTIONS WHERE APPLICABLE

Sensor	12-bit ADC (Bayer system color, single sensor) with 20 μm pixel
Shutter	Global electronic shutter from 16.7ms to 1 μs independent of frame rate
Lens Mount	Interchangeable F-mount and C-mount using supplied adapters
Extended Dynamic Range	Selectable in twenty steps (0 to 95% in 5% increments) to prevent pixel over-exposure
Memory	8GB (standard: 5,457 frames @ maximum resolution) 16GB (option: 10,913 frames @ maximum resolution) 32GB (option: 21,841 frames @ maximum resolution) 64GB (option: 43,686 frames @ maximum resolution)
Video Output 1	NTSC/PAL composite VBS (BNC). Ability to zoom, pan and tilt within image via keypad. Live video during recording
Video Output 2	HD-SDI: HD-SDI 2 channel (BNC) digital output
Camera Control	Through optional keypad with integrated viewfinder and Gigabit Ethernet or RS-422
User Preset Switches	Four user selectable camera function controls mounted on the camera's rear panel
Low Light Mode	Low light mode drops the frame rate and shutter time to their maximum values, while maintaining other set parameters, to enable users to position and focus the camera
Triggering	Selectable positive or negative TTL 5Vp-p or switch closure
Trigger Delay	Programmable delay on selected input and output triggers, 100ns resolution
Timing	Internal clock or external source
Phase Lock	Enables cameras to be synchronized precisely together to a master camera or external source, such as IRIG/GPS time codes

Event Markers	Ten user entered event markers mark specific events within the image sequence in real time. Immediately accessible through software
Dual Speed Recording	Enables the recording speed to be changed up or down by a factor of 2, 4 or 8 during a recording
Trigger Modes	Start, End, Center, Manual, Random, Random Reset, Random Center, Random Manual and Duals Speed Recording
Saved Image Formats	JPEG, AVI, TIFF, BMP, RAW, PNG, MOV and FTIF. Images can be saved with or without image or comment data
Data Display	Frame Rate, Shutter Speed, Trigger Mode, Date or Time, Status (Playback/Record), Real Time, Frame Count and Resolution
Partitioning	Up to 64 memory segments for multiple recording in memory
Data Acquisition	Supports Photron MCDL and DAQ
Cooling	Actively cooled
Operating Temperature	0 - 40 degrees C (32 - 104 degree F)
Mounting	1 x 1/4 - 20 UNC, 1 x 3/8 - 16 UNC, 6 x M6
Dimensions	165mm (6.50")H×153mm (6.02")W×242.5mm (9.55")D *excluding protrusions
Weight	6.2 kg (13.67 lbs)
Power Requirements	100V - 240V AC ～ 1.5A, 50-60Hz DC operation 18 - 36 V DC, 100VA

Specifications subject to change without notice

Appendix B

Fe–Cr–Ni Phase Diagrams
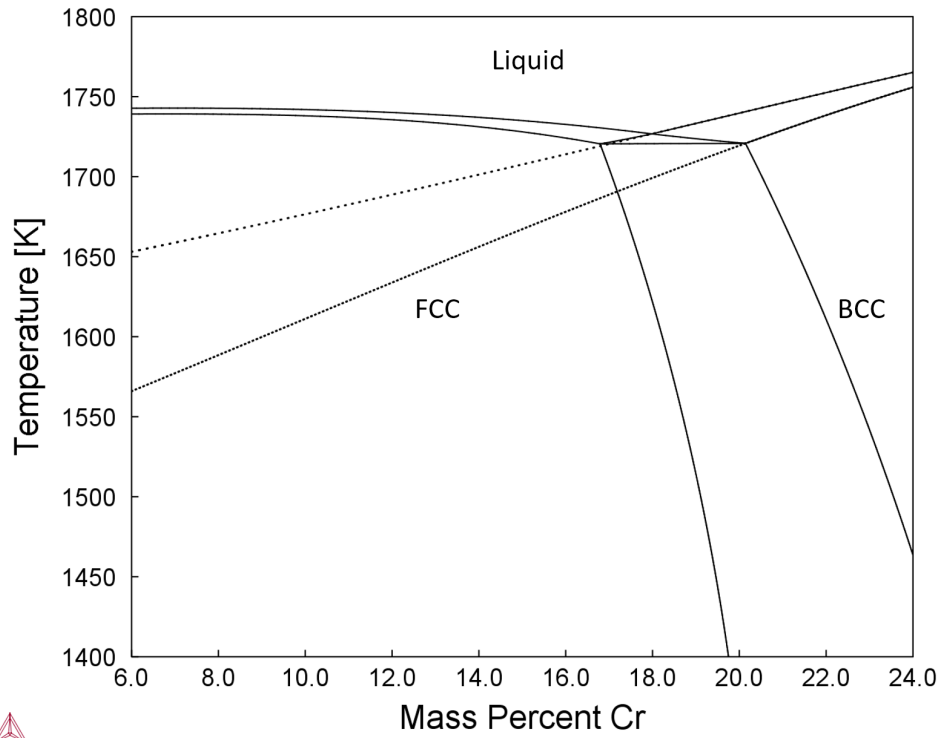
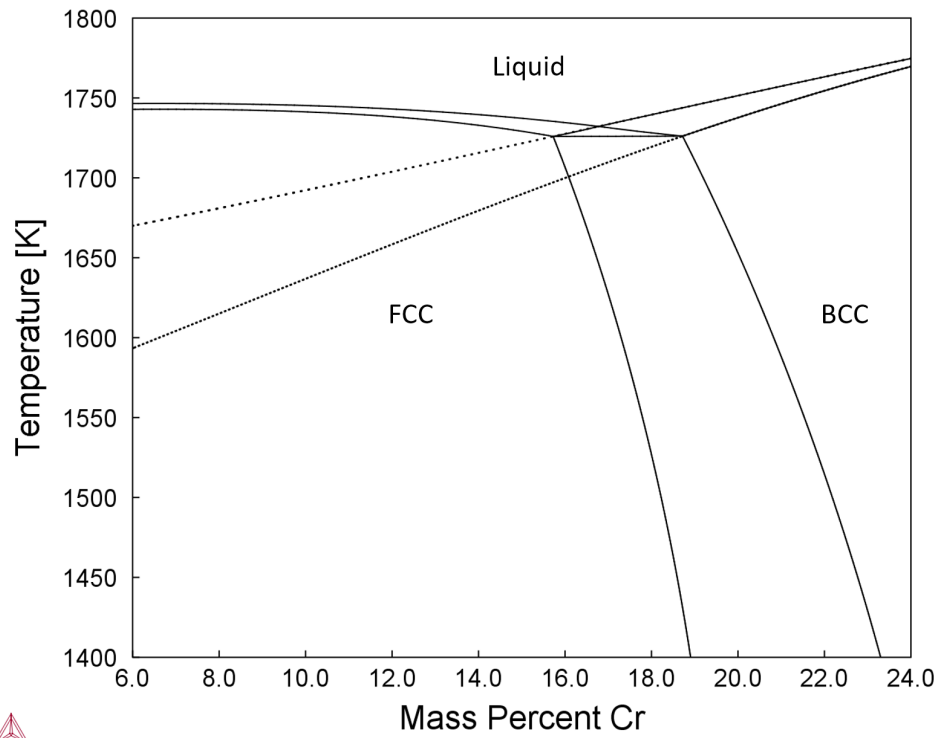**Figure B.1:** $Fe_{70}Cr_xNi_{30-x}$ wt.% pseudobinary phase diagram.

Figure B.2: $Fe_{72}Cr_xNi_{28-x}$ wt.% pseudobinary phase diagram.